INFORMATION TO USERS

This manuscript has been reproduced from the microfilm master. UMI films the text directly from the original or copy submitted. Thus, some thesis and dissertation copies are in typewriter face, while others may be from any type of computer printer.

The quality of this reproduction is dependent upon the quality of the copy submitted. Broken or indistinct print, colored or poor quality illustrations and photographs, print bleedthrough, substandard margins, and improper alignment can adversely affect reproduction.

In the unlikely event that the author did not send UMI a complete manuscript and there are missing pages, these will be noted. Also, if unauthorized copyright material had to be removed, a note will indicate the deletion.

Oversize materials (e.g., maps, drawings, charts) are reproduced by sectioning the original, beginning at the upper left-hand corner and continuing from left to right in equal sections with small overlaps. Each original is also photographed in one exposure and is included in reduced form at the back of the book.

Photographs included in the original manuscript have been reproduced xerographically in this copy. Higher quality 6" x 9" black and white photographic prints are available for any photographs or illustrations appearing in this copy for an additional charge. Contact UMI directly to order.

UMI

A Bell & Howell Information Company
300 North Zeeb Road, Ann Arbor MI 48106-1346 USA
313/761-4700 800/521-0600

A MECHANISTIC APPROACH TO DETERMINE THE IMPACTS OF SMALL UTILITY CUTS IN URBAN STREET PAVEMENTS

by

MEWBURN HILARY HUMPHREY

A dissertation submitted to the Graduate Faculty in Engineering in partial fulfillment of the requirements for the degree of Doctor of Philosophy, The City University of New York

1997

This manuscript has been read and accepted for the Graduate faculty in Engineering in satisfaction of the dissertation requirement for the degree of Doctor of Philosophy.

4/29/97
Date

Dr. Neville A. Parker
Professor of Civil Engineering
Chair of Examining Committee

4/30/97
Date

Dr. Gerald G. Lowen
Executive Officer

Dr. Edward S. Reitz
Associate Professor of Civil Engineering
City College of New York

Dr. Carl J. Costantino
Professor of Civil Engineering
City College of New York

Dr. Lynne H. Irwin
Professor of Agricultural & Biological
Engineering/Civil Engineering
SUNY at Cornell University

Dr. Mohammed H. Maher
Associate Professor of Civil Engineering
Rutgers University

Dr. Nenad Gucunski
Assistant Professor of Civil Engineering
Rutgers University

Supervisory Committee

The City University of New York

ABSTRACT

A MECHANISTIC APPROACH TO DETERMINE THE IMPACTS OF SMALL UTILITY CUTS IN URBAN STREET PAVEMENTS

by

Mewburn Hilary Humphrey

Advisor: Professor Neville A. Parker

Utility cuts in urban street pavements have been observed to be a major cause of premature pavement deterioration, with related high maintenance and road user costs.

This research determined that when a small utility cut (3' - 0" x 3' - 0") is opened in a city street pavement, the surrounding soil stretches towards the cut, until a state of plastic equilibrium is achieved. The localized stretching was found to extend a distance of 3.25 to 3.5 feet from the face of the cut, for utility cuts varying from 3 to 5 feet deep.

The research used elasto-plastic theory and three dimensional finite element methods to analyze the pavement materials around the open utility cut, for unsupported depths of up to 5 feet. The ANSYS - Engineering Analysis System, Revision 5.2, 1995 was used in this analysis. The research used three density combinations, ranging from 110 to 130 lb/ft^2 in the fill/subgrade material, and 125 to 140 lb/ft^2 in the base material. Three ϕ scenarios were used per combination, ranging from 30° to 38° in the fill/subgrade, and 32° to 40° in the base. For similar ϕ values, soil stretching around the cut was not found to be a function of soil density. Hence a detailed study was done on the mid-range properties of the materials selected for the analysis, to obtain a representative set of results on predictable pavement distresses in the vicinity of open utility cuts. The research produced tables and charts to enable agencies to predict the distress impacts to the

pavement in the area surrounding the utility cut. The results are expected to enable agencies to predict the appropriate PCI deduct values for small utility cuts in city street pavements, when routine pavement evaluations are done. Further, it is expected that from the results of this research, that an appropriate fee structure could be developed for pricing utility companies, when applications are made for small utility cuts.

This research is expected to explain and theoretically extend/complement work done by others which reported physical observations of surface distresses and abnormal pavement deflections in the vicinity of utility cuts.

This Dissertation is dedicated to my wife, Agnes and children; Mewburn Jr., Marcia, Michelle and Marissa, for their love and devotion and for the strength they gave me during this long journey.

Acknowledgments

My heartfelt thanks to the members of the Supervisory Committee who provided me with the necessary guidance to enable the production of this quality document. To the Chairman of the Committee, Professor Neville Parker of The City College of New York, I extend my gratitude for his consent to be my mentor, and for his guidance, from the gathering of the topic some years ago to his provision of the literature on the pipeline theory, vital to the research, through the analyses and production of the Dissertation. To Professor Costantino of The City College of New York, my thanks for shining some light on the issue of cohesion when the pure granular soils created a series of problems in the analysis. To Professor Edward Reitz of The City College of New York, "The Phantom of the Field House", my sincere thanks for his instructions on Finite Element Analysis and the use of ANSYS for the conduct of the analysis. He allowed me the use his office and computer and made his library available to me for the furtherance of my knowledge in finite element methods and plasticity theory. To Professor Lynne Irwin of Cornell University, who consistently and meticulously read all of my Proposal and Dissertation drafts, my sincere thanks for his detailed comments and advice, which inputs have been a major influence in the shaping of the research. To Professor Nenad Gucunski of Rutgers University, my thanks for his guidance during the conduct of the stress relief analysis and for his comments on the compilation of the document. To Professor Mohammed Maher of Rutgers University, my thanks for his comments on the draft submissions.

To Professor Claire McKnight, my Masters Degree advisor, my thanks for her early guidance when I was contemplating embarking on this venture and the continuous

guidance and listening ear she provided over the years. To Dr. Shaoquan Lin, the Administrator of the computer system, my thanks for his assistance in finding me disk space when it was scarce. For his pleasant disposition even when my large models crashed the system yet another time. To Professor Jacques Benveniste, my thanks for his guidance on the execution of special applications of ANSYS.

My thanks to John Kwan, Computer Technician, for his support. To Ms. Linda Smith the Department Secretary my thanks for her assistance in enabling me to have the conveniences to bring this task to an end. To Ms. Desiree Richards of the Institute for Transportation Systems, my thanks for her assistance in coordinating my respective administrative matters during my stay with the Institute. My thanks to Dr. Beatrice Issacs for her guidance and advice along the way. To my friends and colleagues, past and present, at the Port Authority of NY & NJ and at Lockwood Kessler and Bartlett, my sincere thanks for their support and encouragement, when they were most needed. To my many other friends and well wishers, my sincere thanks for their encouraging support.

To my mother Agatha, sister Bridget, brothers Burchell and Clairmonte and cousin James, my thanks for their encouragement throughout the years. To my mother-in-law Cicely and my many in-laws, I express my gratitude for their encouraging support.

Finally, to my dear wife Agnes, who read everything and made very important editorial contributions, I express sincere thanks for her love, patience and support over these long years. To my Children Mewburn Jr., Marcia, Michelle and Marissa, I also express my sincere thanks for their love, support and understanding, during the long years they endured without vacations, while I toiled on research and analyses.

Table of Contents

Table of Contents (Cont'd)

Table of Contents (Cont'd)

Table of Contents - List of Tables

Table of Contents - List of Tables (Cont'd)

Table of Contents - List of Figures

Table of Contents - List of Figures (Cont'd)

Table of Contents - List of Figures (Cont'd)

Table of Contents - List of Figures (Cont'd)

Table of Contents - List of Figures (Cont'd)

Table of Contents - List of Figures (Cont'd)

CHAPTER I

DEFINITIONS

The definitions of some important terms used in the text are given at this time to clarify their usage in the dissertation.

DILATANCY: "The tendency of a volume to increase under increasing stress difference is known as *dilatancy*." (Terzaghi and Peck 1967, 94).

ELASTIC EQUILIBRIUM: "The active and passive Rankine states constitute the two limiting states for the equilibrium of the sand. Every intermediate state, including the state of rest, is referred to as a *state of elastic equilibrium*." (Terzaghi and Peck 1967, 189). "The term *elastic equilibrium* does not imply any definite relationship between stress and strain. It merely implies that an infinitely small increase of the stress difference produces no more than an infinitely small increase of the strain." (Karl Terzaghi 1943, 26). In the plot of the Mohr circle, if the circle of stress does not touch the lines of rupture (the Mohr envelope) the soil is said to be in a state of rest or elastic equilibrium. (Karl Terzaghi 1943, 26). See Chapter V.

PLASTIC EQUILIBRIUM: "A body of soil is in a state of *plastic equilibrium* if every part of it is on the verge of failure. " (Terzaghi and Peck 1967, 187). The

limiting states forming the threshold to plastic failure are the active and passive states:

For active earth pressure the coefficient of active earth pressure is represented by;

$$K_A = p_h/p_v = 1/N_\phi = \tan^2 (45° - \phi/2) \quad (1.1)$$

where: $N_\phi = (1 + \sin \phi)/(1 - \sin \phi) = \tan^2 (45° + \phi/2)$

is defined as the flow factor

and in the active state the intensity of horizontal pressure at any depth z is equal to:

$$p_h = K_A p_v = K_A \gamma z \quad (1.2)$$

For passive earth pressure, the coefficient of passive earth pressure is represented by;

$$K_p = p_h/p_v = \sigma_1/\sigma_3 = N_\phi \quad (1.3)$$

where: σ_1 = Major principal stress

σ_3 = Minor principal stress

And in the passive state the intensity of horizontal pressure at any depth z is equal to:

$$p_h = K_p p_v = K_p \gamma z \quad (1.4)$$

(Terzaghi and Peck 1967, 186-189).

An element of soil can be changed from a state of *elastic equilibrium* to that of *plastic equilibrium* by stretching the entire mass uniformly in a horizontal direction, or by uniformly compressing the mass in the

same direction, with the pressure on the base remaining the same. (Karl Terzaghi 1943, 28). In the plot of the Mohr Circle ..."if the circles of stress touch the lines of rupture, an infinitely small increase in stress differences produces a steady increase of the corresponding strain. (Karl Terzaghi 1943, 26). See Chapter V.

FAILURE: In the context of this research, failure of a utility cut represents "the transition from the state of *plastic equilibrium* to that of plastic flow." "...The stresses which start the plastic flow are assumed to be identical with those required to maintain the state of flow", therefore, any further stretching or compression will not alter the state of stress in the material. (Karl Terzaghi 1943 ,28).

In the context of this research, failure of a utility cut patch or any other part of the pavement surface is considered to be any permanent settlement of the area of > 0.5"

HOMOGENEOUS: In relation to a soil, the term *homogeneous* refers to "its properties being constant from point to point. (Lambe and Whitman, 1969, 100).

ISOTROPIC: In relation to a soil, the term *isotropic* refers to its properties being "the same in each direction through a point." (Lambe and Whitman, 1969, 100).

MECHANISTIC: Adj. **1:** mechanically determined **2 a:** of, relating to, or consistent with the theory of philosophical mechanism **b:** of, relating to or

marked by a psychological mechanism tending to interpret conduct in terms of theoretical mechanisms. (Webster's English Dictionary)

UTILITY CUT: In the context of this research, a utility cut is an excavation made in a street to allow utility companies to access buried utility lines. Utility cuts can be of any size and shape. A small utility cut is considered in this research to be an excavation of size 3' - 0" x 3' - 0" for unsupported depths of up to 5 feet.

INTRODUCTION

Reports in the literature on utility cuts have indicated, that the presence of utility cuts in the street pavement, have contributed, in some considerable measure, to the deterioration of pavement life. Previous studies by Shahin and Crovetti 1985 have shown that pavement life can be shortened by a factor in excess of 1.7, wherever utility cut patching is located. The failure of small utility cuts (approximately 3'-0" x 3'-0"), have recorded high occurrences in several North American cities, requiring American Public Works Association (APWA) intervention.

AIM

The aim of this dissertation is to determine what failure mechanisms exist in the vicinity of small, open utility cuts, in urban street pavements.

HYPOTHESIS

The following hypotheses emerged from both the review of the literature on utility cuts, and the physical evidence of pavement distresses in the vicinity of utility cuts, in urban street pavements. The research will test the following hypotheses:

* That when utility cuts are opened in city street pavements, the soil goes from a state of elastic equilibrium to a state of plastic equilibrium in the areas surrounding the opening in the pavement. This transformation in the states extends from the face of the utility cut to a limited distance into the pavement structure, characterized by shear deformation and stretching of the soil mass in X-, Y- and Z- directions, throughout the depth of the cut.
* That some local form of displacement profile is created, at some distance from the face of the cut, which encloses a localized stretching zone in the elasto-plastic soil, surrounding the utility cut. Within this displacement envelope, the confining stresses are released, material bulking occurs through dilatancy, and the soil stretches and heaves, due to decompression and rebounding of the soil. Beyond this localized displacement envelope, the remaining pavement structure is unaffected, and remains in a state of elastic equilibrium. This is believed to be due to inter-granular frictional resistance in the material, and better material confinement with increasing distance from the face of the utility cut.
* That the existing restoration methods address only the patch area and do not address the resident distresses characteristics, created when the cut was opened. This is

believed to contribute to residual distresses in the pavement area, around the restored utility cut.

RESEARCH FOCUS

The research will utilize elasto-plastic theory, through finite element methods, to examine which mechanisms possibly contribute to pavement distress in the vicinity of utility cuts, in urban street pavements. The research will use compacted density values for the respective layers, to determine the vertical stress (σ_1) at any depth in the pavement. Horizontal stress ($\sigma_2 = \sigma_3$) values will be determined by depth and which will be used to compute material modulus values for use in the analyses. Other input values will be the Poisson's ratio, the material angle of internal friction, material dilatancy angle and a minimum cohesion value, to represent the assumed intrinsic cohesion value present in granular roadbed materials. Note that in the text it is stated that "...very few natural soils are perfectly cohesionless." (Terzaghi & Peck 1967, 232).

In determining the horizontal stresses for the material at rest, the following approach was taken in this research. "The corresponding ratio σ_{h0}/σ_{v0} between the vertical and the horizontal principal stresses for a mass of soil in a state of rest depends on the type of soil, on the geological origin of the soil, and on the temporary loads which have acted on the surface of the soil. If the nature of a mass of soil and its geological history justify the assumption that the ratio σ_{h0}/σ_{v0} is approximately the same for every point of the mass, it will be called the coefficient of earth pressure at rest and designated by the symbol K_0." (Karl Terzaghi 1943, 27-28).

The *coefficient of lateral stress or lateral stress ratio* is expressed as the ratio of horizontal stress to vertical stress (σ_3/σ_1) and denoted by *K*. "The definition of K is used, whether or not the stresses are geostatic. Even when the stresses are geostatic, the value of K can vary over a wide range, depending on whether the ground has been stretched, or compressed in the horizontal direction, by either the forces of nature or the works of man." (Lambe and Whitman, 1969,100). After a soil has been deposited (naturally or artificially), K has a value K_0 intermediate between K_A and K_P such that:

$$p_h = K_0 p_v \tag{1.5}$$

Supporting the theory, is the following passage from the text, that the value of K_0, "...depends on the relative density of the sand and the process by which the deposit is formed. If this process did not involve artificial compaction by tamping, the value of K_0 ranges from 0.5 for dense sand to 0.4 for loose sand. Tamping in layers may increase the value to about 0.8. " (Terzaghi & Peck 1967, 188).

Using the foregoing assumptions and limiting conditions, the research will use the range $\mathbf{0.4} \leq \sigma_3/\sigma_1 \leq \mathbf{0.8}$ for the granular materials used in this analysis, ranging from the coefficient of earth pressure at rest, to an almost rigid confinement, when compacted in the pavement structure.

Using the above assumptions, (which will be elaborated on, in much more detail, later in the dissertation), the research will determine/establish what happens in the soil mass, when the cut is made in the pavement. The analysis will include:

- Structuring the model for analysis, that would closely mirror field conditions for a flexible pavement, subjected to a utility cut.

- Determining what are the horizontal and vertical soil pressures in each layer, from the relationships discussed above.
- Determining the material modulus values by layer, using the soil pressure values.
- Applying the appropriate Poisson's Ratio.
- Determining the nodal forces by layer, for the respective Density Combinations used in the research.
- Determining the minimum cohesion value for the granular materials that will provide a stable solution for the model, representing stable cut conditions, observed in granular materials in the field.
- The research effort will use three-dimensional finite element theory, through the ANSYS Solid 45 model, to apply three-dimensional plasticity theory, to determine the nature of the pavement distresses, when the utility cut is opened.
- Process the analyses and report on results obtained.

The research will assume the following in each model analyzed, which will be elaborated on in much more detail, in later chapters of this dissertation:

- The road structure is founded on firm subgrade.
- The materials in each layer are homogeneous and isotropic, which may not necessarily be so, due to unpredictable nature of soils, but is so assumed in the ideal models for this utility cut analysis.
- The road structure is unaffected by ground water.
- The road structure is made up of granular fill and a granular base, each having some intrinsic cohesion value (to be determined), and an asphaltic concrete surface.

- The excavation is not affected by traffic vibration.
- The excavated material is not heaped on the edges of the cut, causing the inducement of additional surcharge on the walls of the cut.
- The analysis assumes symmetrical loading around the utility cut in the development of the model.
- The model assumes a rapidly excavated utility cut and measurement of the surrounding distresses as soon as the excavation is completed.

Because of the predominance of flexible pavements in North American city streets, this research will address utility cut problems in flexible pavements. However, the Researcher assumes that displacements and localized stretching patterns in the fill material, are expected to be similar in character in the composite pavement, due to the influence of geostatic forces The reports in this research are expected to make this assumption more evident as the dissertation is developed.

The research is expected to theoretically complement the field determinations made by others, from observed and measured surface distresses in the vicinity of utility cuts. The research is expected to extend a theoretical explanation of these surface distresses, through a mechanistic examination of the pavement, in depth, to determine what failure characteristics exist in the fill, base and surface materials, in the vicinity of the open utility cut.

CHAPTER II

DEFINITION OF THE PROBLEM

Evidence from the literature on utility cuts has indicated that non-destructive field testing in the vicinity of restored small utility cuts has determined that pavement distresses exist in these areas. This phenomenon has led the Researcher to believe that the damage done to the pavement is not only confined to the cut area but also to an area located some distance from the face of the utility cut and which may not be totally recoverable by normal compaction methods when the cut is restored. It is the Researcher's opinion that limitations in the Poisson's Ratio of the backfill material does not provide for sufficient lateral expansion of the material from vertical tamping, during the restoration process. Because of these limitations, it is believed that the material does not exert the necessary horizontal pressures to restore the plastic deformation in the distress zone that is created in the surrounding soil when the cut is made.

To deal with the problem of restoring the integrity of the utility cut and its surroundings, other methods were explored to deal with the restoration process. In Canada and the United States, some schools of thought suggest that a cement slurry backfill will remedy the problem. For further information on this material, refer to: (Arizona Roads Newsletter Vol. 4 No. 4. "Non-shrink Backfill Saves Time, Money In Restoring Utility Cuts." October 1988: Department of Water and Power, City of Los Angeles. Slurry backfill Program, 1973: Emery, John J., and Tom H Johnston. "SP 93-10 - Unshrinkable Fill for Utility Cut Restorations," 1986, 187-211: Emery, John J., and

Tom H Johnston. "Influence of Utility Cuts on Urban Pavement Performance." 1985: Metropolitan Toronto Roads and Traffic Department. "Utility Cut Restoration, Problems and a New Policy." Toronto: April 1985). The Researcher is of the opinion that a slurry backfill will restore the utility cut with a hard plug, but the areas surrounding the utility cut will have the resident plastic equilibrium characteristics (a stretching zone) that is believed to be the contributor to pavement distresses at utility cut sites, and which will be addressed in later chapters of this dissertation.

Normal infrastructure development practices locate utility lines in the fill material of city street pavements, and from time to time, utility companies need to cut the city streets to access these utilities, for new connections, or to address emergencies, or other repairs.

In order to maintain smooth streets, utility cuts in the urban street setting require increased maintenance activities, over and above that required for life cycle maintenance of the remaining pavement. If serious deterioration in the serviceability and ride-ability of the pavement surface occurs, due of the number of failed or failing utility cuts, overlays become necessary, to restore pavement integrity and design life. In the extreme case of pavement deterioration and negligent maintenance practices, reconstruction may even become necessary.

Maintenance and repair costs, though created by utility companies, are borne by the consumer. These surface and/or structural defects generate high road user costs, and to maintain smooth streets in the city environment, result in high street maintenance costs, funded through taxation.

Work Done By The American Public Works Association

In an attempt to quantify the destructive effects of utility cuts in urban city street pavements, the American Public Works Association (APWA) convened a committee in 1989, comprising representatives of City Agencies, to develop the research project, *"Recovering Costs of Pavement Cuts."* The aim of that project was identified as the development of *"a method for calculating the real costs of pavement cuts and establishing an equitable fee structure to recover those costs."*

The primary areas studied by the committee included:

1. Pavement Performance
2. A Fee Structure, and
3. Controlling Cuts

Absent from the above study, was the determination of the causes of failure in and around utility cuts, their effects, and the corrective measures that need to be taken to remedy structural deficiencies in and around the vicinity of utility cuts. It is the Researcher's opinion that these findings were necessary in order to develop a realistic setting for determining a fee structure, to cover full pavement restoration costs.

The APWA activity sought, in a general sense, to establish a standard method for calculating the real costs of utility cuts in pavement structures, which could be charged to applicant utility companies. The determination of their proposed costs would include costs for maintenance and protection of traffic, anticipated rehabilitation and pavement maintenance, for a minimum period of two years. The University of Cincinnati in cooperation with the City of Cincinnati was contracted to assist the APWA study, by

monitoring the impact of utility cuts on the performance and life span of city street pavements. The primary objective of their study was to obtain reliable and consistent information on the impact of utility cuts on the performance and life-cycle of street pavements, and to establish a Utility Cut Management System (UCMS). The study set out to investigate the impact of cuts on the fatigue life and riding quality of pavements, as well as set up a comprehensive data base of existing and new cuts. The effort was expected to generate a statistically calibrated model for predicting future pavement performance in the vicinity of utility cuts, and for estimating the monetary impacts of utility cuts in the pavement.

Work Done by Shahin and Crovetti

In the Shahin and Crovetti 1985 study entitled, *"Effects of Utility Cut Patching on Pavement Performance and Rehabilitation Costs,"* the Pavement Condition Index (PCI) procedure laid out in The US Army Corps of *Engineers "Construction Engineering Research Laboratory Technical Report M-294"*, was used to test and analyze pavements containing utility cuts in a Northeast United States city setting. The PCI is a numerical indicator of the pavement condition, which has a numerical scale ranging from 0 to 100, with excellent representing 100. The new pavement's attainment of any specific PCI in time, results from subtracting deduct values from 100, attributable to various surface distresses. In the case of utility cuts, the exact size of the utility cut is measured, and a deduct value applied for subtraction from the existing PCI, depending on the severity of distress in the utility cut patch area.

The objective of the Shahin and Crovetti 1985 study was to determine the average life of pavements, with and without utility cut patching. Their study sought to describe some procedures for testing and analyzing pavements containing utility cut patching, in order to determine the effects of such patching on the pavement performance and structural adequacy. This, they achieved through consideration of both pavement performance and load carrying capacity. From data collected, they determined that pavement life was shortened by a factor of over 1.7 as a result of utility cut patching. Pavement life was defined in their study to be the age in years that the street can be economically maintained without the need for major a rehabilitation, such as an overlay, and not at the point when the street can no longer safely carry traffic. The study defined the minimum economical PCI for a pavement to be 70.

The Shahin and Crovetti 1985 study did some extensive deflection testing of streets in their study area. They determined that areas, in and around the patches, were considerably weaker than the original pavement. They further determined that patches were a major source of discontinuity and non-uniformity in a pavement, with detrimental effects to future pavement performance

The Shahin and Crovetti 1985 study showed, that the maximum deflection of a pavement under a given load, was taken as an indicator of its load carrying capacity. The study noted that the higher the surface deflection, the fewer the number of wheel applications before structural failure occurs. A second indicator of structural adequacy in a pavement was used in the Shahin and Crovetti 1985 study, taken from work developed by Jim Hall, Waterways Experiment Station, US Army Corps of Engineers, but which has

not received general acceptance as a measure of structural adequacy in a pavement. It is, however, mentioned here, not for numerical reasons but to convey the fact that tests were done in the vicinity of utility cuts, and which determined that weaknesses of the road structure do exist, in and around these cuts. This indicator was the *Dynamic Stiffness Modulus (DSM)* which was computed, using the maximum deflection (in mils) under three load levels (7,000, 9,000, and 17,000 pounds). The *DSM* was defined as:

$$\text{DSM} = \frac{\text{Load X - Load Y}}{\text{Deflection at Load X - Deflection at load Y}} \qquad (2.1)$$

where Load X is greater than Load Y.

The DSM test was conducted in four areas (see Figure 2.1) viz.,

1. The center of the patch
2. The edge of the restoration within the patch
3. The edge of the restoration outside of the patch
4. A distance less than three feet away from the edge of the patch, in the adjacent pavement.

Average edge patch DSM values at the edge of the patch adjacent to the pavement (PAT-E), and at the edge of the pavement adjacent to the cut (PVT-E), were found to be lower than those at the center of the patch (PAT), and those at some distance in sound pavement, away from the patch (PVT).

LEGEND:

PAT	Test points inside patch
PAT-E	Test areas within patch boundaries adjacent to pavement
PVT-E	Test areas adjacent to patch (less than 3 feet away)
PVT	Test areas away from patch

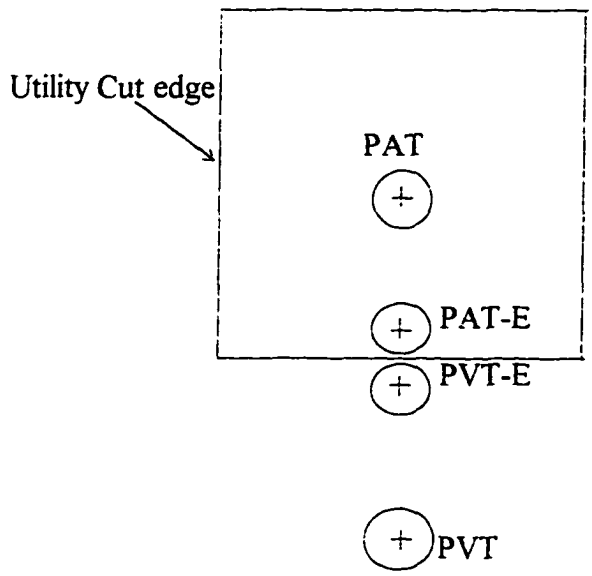

Figure 2.1

Utility cut test location designations. (Shahin and Crovetti 1985).

In pavements with utility cuts, Shahin and Crovetti 1985 determined that overlays increased pavement thickness and stiffness Modulus, reduced pavement deflections, and increased service life, but did not seem to correct the underlying distresses in the region of the utility cut.

Shahin and Crovetti 1985 determined in their study that there was some difficulty in obtaining desired densities in the backfill material of small utility cuts. They further

determined in flexible pavements, that in the utility cut patch and for some distance away from the cut, there were observable pavement weaknesses. Their study did not consider the failure mechanisms that contributed to these weaknesses in the vicinity of the utility cuts, nor indicated whether they related these distresses to pavement depth, material density or material angle of internal friction. Shahin and Crovetti 1985 determined the existence of pavement weaknesses for distances of up to 3 feet from the edge of utility cuts.

Work to be Done in this Research

In addition to the activities referred to in Chapter I, this research intends to develop a nest of curves, representing the extent of the distress characteristics that exist in the soil mass surrounding the open utility cut. This is with an aim to providing a guide to city agencies, when determining their restoration specifications, and fee structure to cover costs for utility cut restorations.

In the PCI method, the deduct value for a utility cut is determined from the area of the physical patch. This present research effort intends to determine that the deduct value should consider not only the area of the patch but the affected area which could be as much as 10'-0" x 10'-0" for a 3'-0" x 3'-0" utility cut (depending on the depth of the cut and the respective material properties). This assumption would therefore indicate that a higher deduct value should be used in determining the PCI value for a pavement possessing a utility cut, and that the deterioration rate of the pavement may be much higher than hitherto believed. These issues, which were not considered in the literature on utility cuts, will be reviewed later in the dissertation.

CHAPTER III

OTHER RELATED WORK THAT ADDRESSES THE UTILITY CUT PROBLEM

Of noteworthy importance and somewhat related to this utility cut research, is the work being done on soil behavior, adjacent to trench excavation in the pipeline industry. "Most of the literature dealing with ground movements caused by excavations pertain to deep braced cuts (e.g. Peck, 1969; Terzaghi and Peck, 1967; Clough, Hansen and Mana, 1980; and O'Rourke, 1981)." (Harris and O'Rourke 1983, 4).

There are varying definitions for deep and shallow excavations in the literature, e.g. in Terzaghi and Peck 1967, shallow cuts have depths less that 20 feet and deep cuts have depths greater than 20 feet. O'Rourke and Kumbhojkar 1984 view shallow trench excavation as having a maximum depth of 5 to 6 feet; while Harris and O'Rourke view shallow unsupported trench excavation as having a maximum depth of 4 to 6 feet, and deep temporary trenches as having depths ranging from 6 to 20 feet. Deep braced cuts are considered to exceed depths of 20 feet. The text went on to say that "braced cuts are typically wider and deeper than trenches and are subject to ground movements, such as base heave, that may not occur in trenches" (Harris and O'Rourke 1983, 4) and which should make it even less likely in the small (3'-0" x 3'-0") utility cut. Based on this assumption, base heave was not considered to be a factor in this research.

Harris and O'Rourke 1983 conducted studies of ground movements adjacent to deep trench construction and researched adjacent buried pipeline response to parallel trench construction. They found that ground settlements in loose to dense sand and gravel

were measurable for distances up to 1.5 trench depths from the edge of the trench, with maximum settlements of 0.5% of maximum trench depth. Settlements due to construction traffic and loading along trench edges were found to be as large as 2.5% of trench depth and located within a distance of 0.5 trench depths from the edge of the trench. Horizontal movements indicated maximum displacements of 0.8% of maximum trench depth, with no observable movement beyond a distance of 1.5 trench depths from the edge of the trench. Horizontal movement due to construction traffic and loading were found to be as large as 2.0% of trench depth and located within a distance of 0.5 trench depths from the edge of the trench.

Harris and O'Rourke 1983 determined that ground movements adjacent to trench construction is systematic and continuous, and is generally generated by the release of horizontal stresses and construction loading. It was found that as the face of the trench advances, a vertical and horizontal deformation profile will occur in the adjacent soil. "The horizontal displacement of a line parallel to the trench develops over a distance, L, from an undeformed position in front of the trench face to a maximum displacement behind the trench face." (Harris and O'Rourke 1983, 61-62). They determined that a buried pipeline lying adjacent to an advancing trench will adopt the deformation profile shown in Figure 3.1 for vertical and horizontal movement.

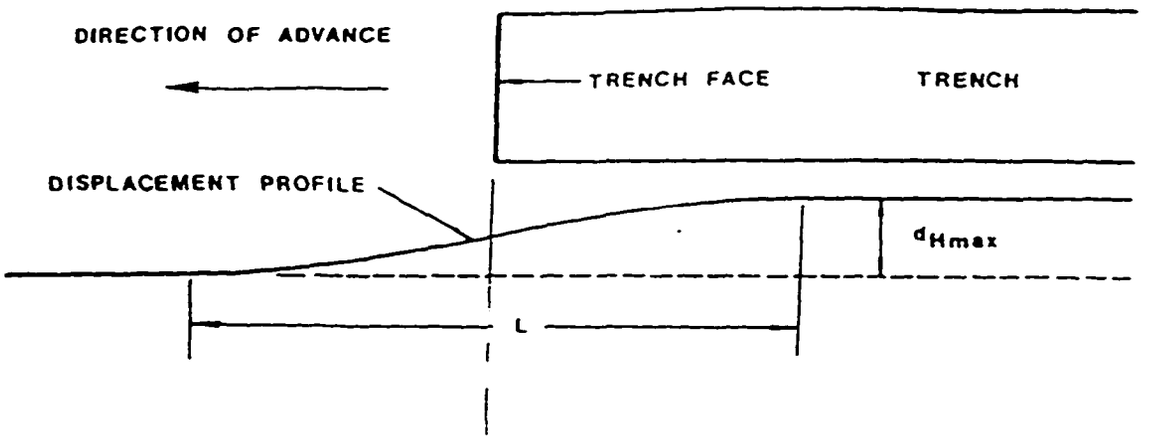

a) Plan View Showing Horizontal Displacement

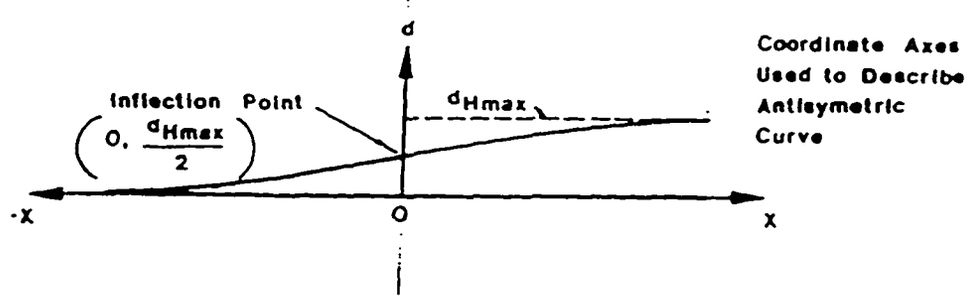

b) Displacement Profile on Reference Axes

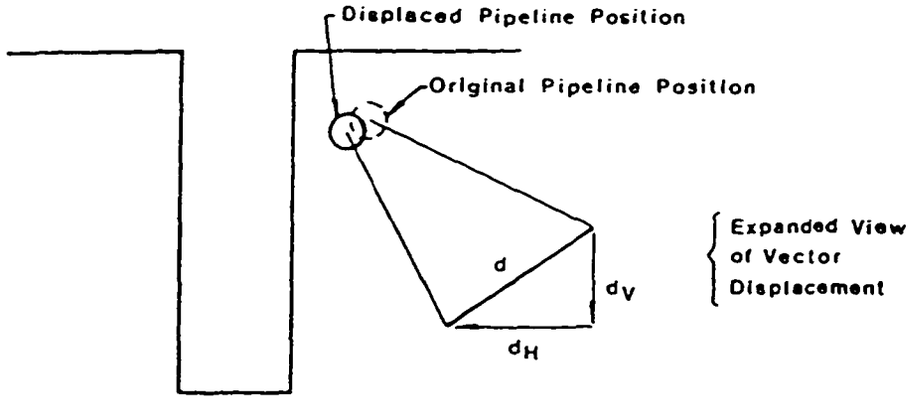

c) Cross-Section Showing Pipeline Movement

Figure 3.1

Ground Movements Parallel to Trench Construction. (Harris and O'Rourke 1983).

The literature states that "if it is assumed that ground displacements near the face of the trench are distributed in an anti-symmetric pattern, the displacement profile could be represented as a continuous curve according to the coordinate axes shown..." in Figure 3.1. (Harris and O'Rourke 1983, 63). The text went on to say that "The inflection point of the curve would occur at the zero coordinate of the horizontal distance axis, and the points of maximum curvature would be at equal distances, less than or equal to ***L/2***, on either side of the zero horizontal coordinate." (Harris and O'Rourke 1983, 63). In Figure 3.1 the data is shifted parallel to the horizontal distance axis, to the point where, at $x = 0$ at the face of the advancing trench, the ground displacement distance is $\mathbf{d_{Hmax}/2}$. From this position, regarded as the inflection point of the curve "...the points of maximum curvature would be at equal distances, less than or equal to L/2, on either side of the zero horizontal coordinate. For a given shape of the curve and a constant maximum displacement, the maximum curvature would depend on the magnitude of L." (Harris & O'Rourke 1883, 63).

The Harris and O'Rourke 1983 study determined that the soil displacement could be represented by the sine function:

$$\frac{d}{d_{max}} = \frac{1}{2}\{\sin(cx/H) + 1\} \qquad (3.1)$$

Where:

c = Constant expressed in radians.

d = The movement at any point along the displacement profile.

x = Horizontal distance from face of trench.

H = Maximum trench depth.

d_{max} = maximum displacement.

Harris and O'Rourke inversed the sine function to convert the curvilinear distribution to that of a linear function of x/H, to enable regression analysis of the function. The regression model then became:

$$\sin^{-1}\left(2\frac{d}{d_{max}} - 1\right) = \frac{cx}{H} \qquad (3.2)$$

Linear regression analysis by Harris and O'Rourke on the horizontal and vertical displacements produced best fit curves with slope c equal to 1.47 and 1.41 for vertical and horizontal displacements, respectively. These were done between limits $\pm \pi/2$ radians and within which boundary conditions the predictive limits were most sensitive. Accordingly, the standard t test was adapted to define the 95% confidence limit on the predicted value of x/H at $\pm \pi/2$ radians. This produced the equation shown in Equation (3.3) below:

$$c_{max} = \frac{\pi}{2(x/H)_{min}}. \qquad (3.3)$$

where:

c_{max} = Maximum slope c for a 95% confidence.

$(x/H)_{min}$ = Minimum horizontal distance ratio across which distributed displacements occur for depth H.

The c_{max} values for vertical and horizontal displacements are 2.53 and 2.57, respectively and are used in Equation (3.3) or (3.2) to obtain the minimum distance (x_{min}), over which (d_{max}) can occur at $\pi/2$ radians. The c_{min} values for vertical and horizontal displacements are 1.47 and 1.41 and are used in Equation (3.2) to obtain the maximum distance (x_{max}), over which maximum displacement (d_{max}) can occur at $\pi/2$ radians. (Harris and O'Rourke 1983, 63-72).

CHAPTER IV

APPLICATIONS OF OTHER RELATED WORK TO THE UTILITY CUT RESEARCH

The Researcher applied the inverse sine function (Harris and O'Rourke 1983) described in Chapter III, to the utility cut analysis, bearing in mind that the small utility cut is square, with sides 3 feet long and limited in extent and depth, compared to the long pipeline trench that can vary in depth along its length. In addition, the Researcher is aware that in the case of a utility cut, each of the four sides of the square cut could be considered as an advancing face as in the pipeline trench application. Based on this concept it can, therefore, be expected that the deformation profiles will surround the utility cut and overlap among themselves. Figure 4.1 shows a sketch of the Researcher's comprehension of the deformation characteristics around the utility cut, which will be tested in this research. The figure also gives some idea of the expected shape of the distress zone surrounding the cut. This will be discussed further in Chapter VII.

In the application of the Harris and O'Rourke 1983 theory in Chapter III to the utility cut analysis, the Researcher identified the limitations in the application. The research looked at the utility cut as a short square trench (3' 0" x 3' 0") which allows the development of the maximum displacement (d_{max}) in Figure 3.1 to develop only over a distance of x = 1.5 feet from the respective faces of the utility cut. The maximum displacement (d_{max}) is assumed to occur at the respective center lines, as the pairs of anti-

symmetric curves which form on each side of the utility cut intersect at the midpoint at a maximum displacement point. (See Figure 4.1).

The Harris and O'Rourke theory stated that the length of the anti-symmetrical curve $L = 2x$. This results in an anti-symmetric curve of length $L = 2x = 3$ *feet*.

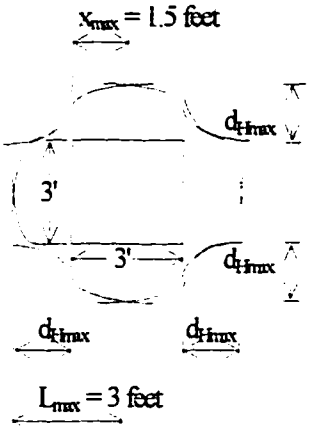

Figure 4.1

Sketch of the assumed network of displacement profiles that surround a small utility cut 3 feet x 3 feet, showing the maximum L value.

The research examined small utility cuts of depths varying from three feet to five feet. From Equations (3.2) and (3.3), Table 4.1 shows the range of **x**-values (the approximate distance from the face of a pipeline trench to the point forward of the face, where the displacements were no longer detected in the pipeline study) for horizontal displacement, if the cut were an extended trench. Note that $x = {}^1/_2 L$ (Harris and O'Rourke 1983).

Table 4.1

Maximum and minimum x values where observable horizontal soil displacements were detected adjacent to pipeline trenches of varying depths.

CUT DEPTH (ft)	MINIMUM X (ft)	MAXIMUM X (ft)
3	1.83	3.34
3.5	2.14	3.90
4	2.44	4.46
4.5	2.75	5.01
5	3.06	5.57

Table 4.2 shows the range of values of **x** (the distance from the edge of the cut to the point where the displacements no longer detected) for vertical displacement, if the cut were an extended trench. Note, also that as in the case of horizontal displacements, $x = {}^1/_2L$ (Harris and O'Rourke 1983).

Table 4.2

Maximum and minimum x values where observable vertical soil displacements were detected adjacent to pipeline trenches of varying depths.

CUT DEPTH (ft)	MINIMUM X (ft)	MAXIMUM X (ft)
3	1.86	3.21
3.5	2.17	3.74
4	2.48	4.27
4.5	2.79	4.81
5	3.10	5.34

The tables show close similarities in the maximum and minimum values for both horizontal and vertical displacements.

As an aside to this study, for each of the 3'-0" x 3'-0", utility cuts analyzed in this research, (where x = 1.5 feet is a constant for all depths), the constant c in Equations (3.1), (3.2), and (3.3), will vary for each H (depth of utility cut). Based on the constant

size small utility cut, the following relationships in Table 4.3 apply for c_{max} from Equation (3.3), for a constant x = 1.5 feet:

Table 4.3

Variation in c_{max} values for a 3' - 0" x 3' - 0" utility cut for changes in depth of cut

H (feet)	c_{max}
3	3.142
3.5	3.67
4	4.19
4.5	4.71
5	5.24

The researcher used Table 4.1 above to set up the dimensional criteria for the analyses in this research after carrying out several tests to determine the width of the model that should be used to analyze the respective finite element models. Although it is assumed that x = 1.5 feet for the small utility cut analyzed in this research, and which should establish the width of the model in this exercise. When the values in the range of x = 1.5 feet and x_{min} in table 4.1 were used in the analysis of the models, solutions were not obtained, because of the close proximity of the geostatic thrust plane to the face of the utility cut in the granular material.

In determining the appropriate width to be used in the utility cut analysis, the research acknowledged that two plastic states exist in a soil mass, the *active Rankine state* and the *passive Rankine state*. These states are produced by stretching and compression, respectively in a semi infinite mass of soil parallel to its surface. "For the active Rankine state the surfaces of sliding descend from the surface at an angle $45° + \phi/2$ to the horizontal. For the passive Rankine state the surfaces of sliding descend at an angle $45° - \phi/2$ to the horizontal." (Karl Terzaghi 1943, 26-32, 35-37). In the active Rankine

state, the minor principal stresses are horizontal. In the passive Rankine state the minor principal stresses are vertical.

Before excavation takes place, the soil mass acting on any element in the soil is in a passive state, with its potential surfaces of sliding making an angle of $45° - \phi/2$ with the horizontal.. When the cut is made and the element is removed, the soil that was adjacent to the element experiences a transition from a passive state to that of an active state, with its potential surfaces of sliding making an angle of $45° + \phi/2$ with the horizontal.. During this process, however, the Researcher is of the opinion that the geostatic forces act on the soil mass even before the active state is fully achieved. The research assumes that thrusting occurs at some point between intersection of the active and passive failure planes with the surface of the granular material. See Figure 4.2.

In determining the width of the model to establish the thrust plane for the application of the geostatic forces to the models in this analysis, the Researcher observed the following:

- The x_{max} distance from the Harris and O'Rourke 1983 inverse sine function coincidentally showed close approximation to the average horizontal distance from the face of the utility cuts to a point midway between the intersection of the active failure plane and the passive failure plane, respectively with the surface. (See Figure 4.2 below). This occurrence gives some attention to the research assumption, that in the transition from the passive to the active state, the geostatic forces act on the soil mass at a distance located between the active and passive failure planes, before the state of stress becomes fully active. The Harris and O'Rourke 1983 study may have identified

the region where the geostatic forces act, in the equation for the x_{max} distance, (the region beyond which no observable distresses were observed in the soil adjacent to the pipeline trench).

- The x_{min} distances determined in Table 4.1 were in the region of the distances set out by the intersection of the active surface of sliding and the surface of the material, from the face of the cut for ϕ Scenario #1, and which decreased with increasing ϕ.

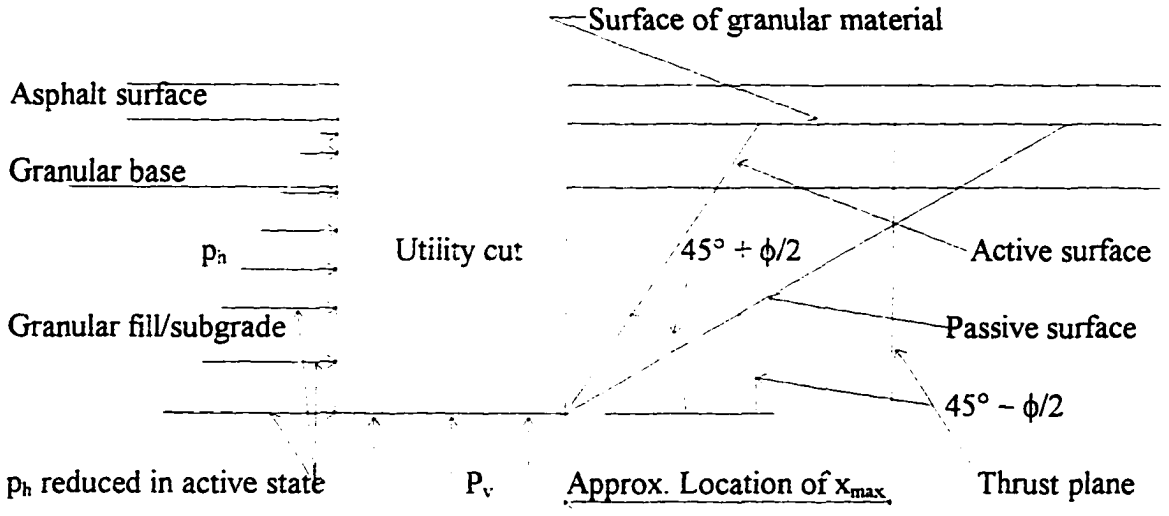

Figure 4.2
Failure planes for the active and passive Rankine states (Terzaghi 1943).

The average distances between the two failure planes and the face of the utility cut for the respective ϕ Scenarios approximated the Harris and O'Rourke 1983 x_{max} distances to the nearest 0.5 foot. (See Tables 4.4 to 4.6).

To establish the model widths, the Researcher used the x_{max} distances (Harris and O'Rourke 1983) which were more closely approximated by the average distances for ϕ Scenario #2, (the average of the three ϕ Scenarios used in the research) rounded to the nearest 0.5 foot. (See Tables 4.5 and 4.7).

For a comparison between the x_{max} distance from the Harris and O'Rourke 1983 theory and the sum of distances to the respective failure planes, see Tables 4.4 to 4.7 These tables were prepared in terms of the respective depths analyzed in this research and for the three ϕ Scenarios used.

The sum of distances to the passive failure plane in Tables 4.6 to 4.7 possibly explain the indications of distress observations by Harris and O'Rourke 1983, for distances of up to 1.5 trench depths, from the face of the trench.

The Researcher, in an attempt to standardize the analyses and establish a point of reference in the conduct of the analyses, decided after several tests, and with the application of the above material, to use the x_{max} distances to define the width of the models for the respective cut depth analyses. The widths of the respective models exceed the Researcher's plot of the anti-symmetric curve in Figure 4.1 for the 3' - 0" x 3' - 0" cut, but based on the theory (Karl Terzaghi 1943) and field observations (Harris and O'Rourke 1983) feels that the dimensions are justifiable for use in this analysis. In addition, using these distances allowed for a mechanistic determination of the extent of the surface distresses as observed by Shahin and Crovetti 1985.

Table 4.4

Distances from the base of the utility cut, to the intersection of the active and passive failure planes with the surface, and computed average distances by depth of utility cut. Phi Scenario #1: $Phi_{Base} = 32°$; $Phi_{Fill} = 30°$

			ACTIVE FAILURE PLANE			PASSIVE FAILURE PLANE			
Trench Depth (ft)	Base Thickness (ft)	Fill Thickness (ft)	Hor. Dist. to Active Plane Base Th./Tan 61 (ft)	Hor. Dist. to Active Plane Fill Th./Tan 60 (ft)	Sum Distance to Active Plane (ft)	Hor. Dist. to Active Plane Base Th./Tan 29 (ft)	Hor. Dist. to Active Plane Fill Th./Tan 30 (ft)	Sum Distance to Active Plane (ft)	Average Distance (ft)
3	0.6667	2	0.3695	1.1547	1.5242	1.2027	3.4641	4.6668	3.0955
3.5	0.6667	2.5	0.3695	1.4434	1.8129	1.2027	4.3301	5.5328	3.6729
4	0.6667	3	0.3695	1.7321	2.1016	1.2027	5.1962	6.3989	4.2502
4.5	0.6667	3.5	0.3695	2.0207	2.3903	1.2027	6.0622	7.2649	4.8276
5	0.6667	4	0.3695	2.3094	2.6789	1.2027	6.9282	8.1309	5.4049

Table 4.5

Distances from the base of the utility cut, to the intersection of the active and passive failure planes with the surface, and computed average distances by depth of utility cut. Phi Scenario #2: $Phi_{Base} = 36°$; $Phi_{Fill} = 34°$

			ACTIVE FAILURE PLANE			PASSIVE FAILURE PLANE			
Trench Depth (ft)	Base Thickness (ft)	Fill Thickness (ft)	Hor. Dist. to Active Plane Base Th./Tan 63 (ft)	Hor. Dist. to Active Plane Fill Th./Tan 62 (ft)	Sum Distance to Active Plane (ft)	Hor. Dist. to Active Plane Base Th./Tan 27 (ft)	Hor. Dist. to Active Plane Fill Th./Tan 28 (ft)	Sum Distance to Active Plane (ft)	Average Distance (ft)
3	0.6667	2	0.3397	1.0634	1.4031	1.3084	3.7615	5.0699	3.2365
3.5	0.6667	2.5	0.3397	1.3293	1.6690	1.3084	4.7018	6.0102	3.8396
4	0.6667	3	0.3397	1.5951	1.9348	1.3084	5.6422	6.9506	4.4427
4.5	0.6667	3.5	0.3397	1.8610	2.2007	1.3084	6.5825	7.8909	5.0458
5	0.6667	4	0.3397	2.1268	2.4665	1.3084	7.5229	8.8313	5.6489

Table 4.6

Distances from the base of the utility cut, to the intersection of the active and passive failure planes with the surface, and computed average distances by depth of utility cut. Phi Scenario #3: $Phi_{Base} = 40°$; $Phi_{Fill} = 38°$

			ACTIVE FAILURE PLANE			PASSIVE FAILURE PLANE			
Trench Depth (ft)	Base Thickness (ft)	Fill Thickness (ft)	Hor. Dist. to Active Plane Base Th./Tan 65 (ft)	Hor. Dist. to Active Plane Fill Th./Tan 64 (ft)	Sum Distance to Active Plane (ft)	Hor. Dist. to Active Plane Base Th./Tan 25 (ft)	Hor. Dist. to Active Plane Fill Th./Tan 26 (ft)	Sum Distance to Active Plane (ft)	Average Distance (ft)
3	0.6667	2	0.3109	0.9755	1.2863	1.4297	4.1006	5.5303	3.4083
3.5	0.6667	2.5	0.3109	1.2193	1.5302	1.4297	5.1258	6.5554	4.0428
4	0.6667	3	0.3109	1.4632	1.7741	1.4297	6.1509	7.5806	4.6773
4.5	0.6667	3.5	0.3109	1.7071	2.0179	1.4297	7.1761	8.6057	5.3118
5	0.6667	4	0.3109	1.9509	2.2618	1.4297	8.2012	9.6309	5.9463

Table 4.7

X_{max} distance used for model width in utility cut analysis

Trench Depth (ft)	Computed x_{max} Distance	Rounded x_{max} Distance
3	3.21	3.5
3.5	3.74	4
4	4.27	4.5
4.5	4.81	5
5	5.34	5.5

CHAPTER V

STRESSES AND STRAINS IN GRANULAR ROADBED MATERIALS

Roadbed Stresses

The application of stress to a particulate system such as soil is no more different than the application of stress to metals, which are made up of a particulate structure of crystals. Because of the particulate structure of all matter, we can safely apply macroscopic stresses to soils as we do with metals, instead of microscopic applications, which would require contact stress analysis, between individual particles of the particulate system. In the application of macroscopic stress to an infinitesimal element of matter, it is assumed that the distance between the particles of the particulate system does not exceed the size of the largest particle within the system. (Lambe and Whitman 1969, 98).

For the purposes of this research it is assumed that the respective materials making up the layers are homogeneous (their respective properties are constant from point to point), and isotropic (their properties are the same in each direction through a point). This assumes ideal conditions in the granular material making up the road bed which, however, is often violated by unpredictable inconsistencies in the particulate system making up the soil. For geostatic stress conditions, where the ground surface is horizontal and there is no variation in the soil in the horizontal direction, soil stress in depth is a function of the soil's unit weight, which increases linearly with depth. Hence, vertical soil stress at any depth in the road bed can be represented as:

$$\sigma_v = \gamma z \qquad (5.1)$$

where:

σ_v = Vertical stress in lb/ft^2

γ = Unit Weight in lb/ft^3

z = Depth in feet

Related to the vertical stress in the soil mass is the horizontal stress, which is developed due to confinement of the soil element by the surrounding soil elements, preventing its lateral displacement. This is explained by the coefficient of lateral stress ratio:

$$K = \sigma_3/\sigma_1 \qquad (5.2)$$

where:

K = Coefficient of lateral stress ratio

σ_3 = Horizontal stress in lb/ft^2

σ_1 = Vertical stress in lb/ft^2

The magnitude of K is a function of the frictional resistance between the particles of the particulate system forming the soil element. The value of K can vary over a wide range of values in the roadbed. These values will depend on whether the soil is in a compressed or stretched state, caused by either the vertical stresses set up by the compactive effort during construction, or due to the removal of these stress effects during maintenance activities in the roadbed, such as utility cuts. The value of K can generally vary between 0.4 and 0.8. (See Chapter III, p7)..

Generally, during confined compression, as in pavement layer compaction, particle movement is in the vertical direction. When the many tangential contact forces are

summed over any plane, there is a net tangential force; i.e. a net shear stress acting on that surface, which generally differs from the vertical stress during confined compression. (Lambe and Whitman 1969, 126-127).

From the text, if the soil can be displaced easily, the ratio σ_3/σ_1 is defined as the coefficient of earth pressure at rest, K_0. "When the granular soil is loaded vertically for the first time, the frictional forces at the contacts act in such a direction that σ_h is less than σ_v; i.e., $K_0 < 1$." (Lambe and Whitman 1969, 127). Jaky 1944 determined that:

$$K_0 = 1 - \sin \phi \qquad (5.3)$$

where:

ϕ = Soil angle of internal friction (values used in this research will be defined later).

In the text it is shown that during the unloading process, the direction of the frictional forces at contact points reverse. "For a given vertical stress, the horizontal stress will be larger during unloading than during the original loading. During the latter stages of unloading, the horizontal stress can even exceed the vertical stress." (Lambe and Whitman 1969, 127). Because of this phenomenon, when the soil is reloaded, during confined recompression, the horizontal stress will almost invariably start out greater than the vertical stress, and the K_0 value will exceed the value in Equation (5.3), until such time, with increase in stress, it returns to this value as the vertical stress increases. See Equations (1.1) and (1.3) and Figure 4.2. This is basically, the underlying phenomenon that prevents normal compaction methods (vertical tamping) in utility cut restoration, from

developing enough horizontal pressure, to horizontally compact the adjacent soil and restore initial stresses.

From the text, we see that during the compactive effort, when shear failure occurs between particles, two activities occur:

1) There is mineral-to-mineral frictional resistance between particles, due to grain interlock among the particles.
2) After exceeding the frictional resistance between particles and the reduction of grain interlock forces, the particles roll over each other into new and tighter positions. Normally some crushing of particles in the soil mass may precede this activity depending on particle hardness.

Strains in Granular Materials

"The strains experienced by an element of soil are the result of strains within and relative motions among the many particles composing the element." (Lambe and Whitman 1969, 122). In granular soils, such as base, subbase, fill and subgrade materials, there are two mechanisms which contribute to soil strain. These are:

1. Distortion and crushing of soil particles at contact points.
2. Soil deformation due to the action of individual particles rolling or sliding over each other.

The uncemented particulate structure of the soil element will contribute to deformation of the soil element whenever high stresses are applied. This is demonstrated by movement of the loose arrangement of the particles in the element when stresses are applied to the element. As these stresses increase, this relative movement between the

individual soil particles causes large strains to occur in the particulate system, as the high contact stresses cause some individual particles to crush, enabling sliding and rolling activity among the soil particles into tighter packed arrays.

If not affected by the environment nor subjected to disturbances by road cuts, the roadbed materials are expected to maintain their compacted state as established during construction.

Removal of Horizontal Equilibrium Force from the Road Structure

In the removal of the horizontal equilibrium stress in the pavement structure, say in the form of a utility cut, the unsupported wall of the utility cut is subjected to released confinement, as well as geostatic forces, which eventually induce shear deformation and a state of plastic equilibrium, which can eventually lead to plastic flow or cut failure. This effect, though, is not extensive and is more or less a local phenomenon. This removal of the horizontal stress can be related to the yielding of a retaining wall and can be typified as follows. "Local events, such as the yielding of a retaining wall, cannot produce a radical change in the state of stress in the sand except in the immediate vicinity of the source of the disturbance. The rest of the sand remains in a state of elastic equilibrium." (Terzaghi & Peck 1967, 189-190).

Within the elastic range, the stress/strain behavior of granular soils is characterized by small movements, caused by elastic deformation of the individual particles. When the critical yield stress occurs (the point at which the Mohr circle touches the failure envelope (see Figure 5.1), in compression, sliding among the particles commences, which reorients the particles in the element and in so doing, reduce the voids ratio of the soil by tighter

particle packing. In tension, the opposite occurs in terms of particle orientation. Rebounding, sliding, and relocation of the particles take place, but with an increased voids ratio in this case, due to material bulking and the particles going into a loose array in the localized yield zone.

Dilatancy

Osbourne Reynolds 1885 determined that a dense sand when compacted in one direction will increase in volume as sliding and rolling occurs. He called this phenomenon *dilatancy*, the measure of volume increase in a soil as it yields, which the Researcher referred to as *bulking* in the previous section. This soil behavior is characterized by the particles riding over each other as the soil commences to yield, thereby increasing soil volume. In Lambe and Whitman 1969 the concept of dilatancy and grain interlock is treated and can be explained as follows:

1) The denser the sand, the greater will be the interlock among the soil particles. This allows for a greater deviator stress ($\sigma_1 - \sigma_3$) and a greater friction angle (ϕ).
2) Strain resistance decreases as the sand expands and stretches.
3) The densest soils will show a more marked decrease in strain resistance as the largest movement among the particles will occur at yield.
4) The denser the sand the greater will be the increase in soil volume, as the tightly packed particles roll over each other as the soil yields.

The Ultimate Condition

In the ultimate condition or plastic flow condition, the grain interlock and friction resistance between particles decreases. This occurs to the point where there is unimpeded

shear displacement among the grains in the soil mass, without any further volume change in the element. At this stage the void ratio "...is independent of the initial void ratio before shearing was commenced." (Lambe and Whitman 1969, 132).

The Effect of Confining Stress

Under higher stress conditions in frictional granular soils, than occurs in road construction, "the resistance to sliding at each contact point is proportional to the normal force at that contact, and hence the overall resistance increases as the confining stress increases." (Lambe and Whitman 1969, 137). Under these conditions interlocking contributes to overall resistance and "decreases as the confining stress increases, because the particles become flattened at contact points, sharp corners are crushed, and particles break." (Lambe and Whitman 1969, 137). These actions cause densification, but provide for shear displacement/deformation to occur. These patterns are not common in road layer materials because of the lower stress applications, even under heavy rolling, as material heave before and after the wheel gives some release to the lateral confinement conditions. The softer granular particles in the material, however, may crush under these compaction stresses.

Mohr-Coulomb Failure Law

"Shear failure starts at a point in a mass of soil when, on some surface passing through the point, a critical combination of shearing and normal stress is reached." (Terzaghi & Peck 1967, 101).

For most engineering problems, the Mohr envelope is used to determine the strength of soils. This envelope is plotted as the tangent to a number of Mohr Circles,

whose diametrical values signify the confining stresses (σ_3) (the lower value) and vertical stresses (σ_1) (the higher value). These stresses are generally determined in the triaxial test. The point at which the tangent touches the circle indicates the failure stresses in shear and compression. Figure 5.1 demonstrates the location of the failure stress in the Mohr diagram and the line from σ_{3f} to the tangent point (σ_{ff}, τ_{ff}) is identical to the slope of the failure plane in the specimen, to the plane of principal stress. The subscripts *f* indicate the failure condition.

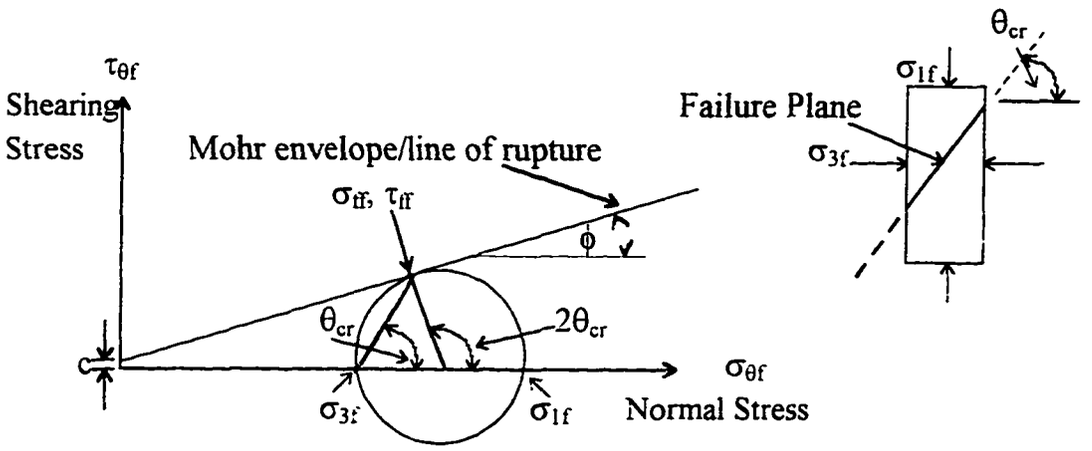

Figure 5.1
Diagram showing the Mohr envelope and stress circle for sand. (Lambe and Whitman 1969)

The shear strength of the soil is determined from testing and reported per the Mohr-Coulomb failure law as:

$$\tau_{ff} = c + \sigma_{ff} \tan\phi \qquad (5.4)$$

where:

τ_{ff} is the shear stress on the failure plane at failure

σ_{ff} is the normal stress on the failure plane at failure

c is the cohesion in the soil

ϕ is the angle of internal friction of the soil.

Use of Equation (5.4) requires a cohesion intercept. Tests have shown that the Mohr envelope is not a straight line, but is in fact curved. The curvature of the Mohr envelope has been determined to be sharper for dense soils and less sharp for loose soils. However, most engineering analysis are conducted assuming a straight line relationship. A straight line Mohr envelope will be assumed for the granular soils in the road structures, that will be considered in this research.

The Researcher attempted in earlier analyses to model pure granular fill and base materials, with a negligible cohesion value of 0.001 lb/in^2. For the ϕ scenario #3 models (highest values used in this dissertation, but the lowest used in the previous analyses), the earlier models failed to generate solutions at the 3 feet to 4 feet and 5 feet depths, which conflicted with stable excavations observed in the field at these depths. These models required unrealistic field values (at least $\phi_{Base} = 42°$ and $\phi_{Fill} = 40°$) to obtain stable solutions. Taking into account that observed field excavations exhibit stable conditions, the Researcher assumed that the materials in the road structure possess some intrinsic cohesion value, hence their stability during unsupported excavations for depths of up to 5 feet. In addition the text indicates that "...very few soils are perfectly cohesionless." (Terzaghi & Peck 1967, 232). In the course of the analyses that followed, the Researcher set out to determine the minimum cohesion values required for cut stability, for depths 3 to 5 feet.

The Meaning of the Mohr-Coulomb Failure Law

Figure 5.2 demonstrates the relationship between ϕ and the principal stresses at failure.

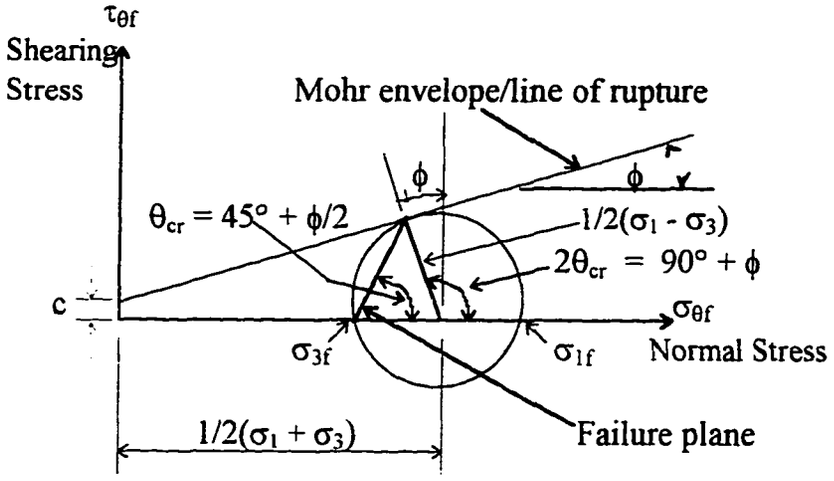

Figure 5.2
Relations between ϕ and principal stresses at failure. (From Lambe and Whitman 1969)

From Figure 5.2 the following relationships can be observed

$$\text{Sin}\,\phi = \frac{(\sigma_1 - \sigma_3)/2}{(\sigma_1 + \sigma_3)/2} = \frac{\sigma_1 - \sigma_3}{\sigma_1 + \sigma_3} \qquad (5.6)$$

$$\text{and;} \quad \sigma_1 \sin\phi + \sigma_3 \sin\phi = \sigma_1 - \sigma_3 \qquad (5.7)$$

Dividing Equation (5.9) by $-\sigma_3$ reduces it to the form of the flow factor (N_ϕ) in Chapter I, where;

$$N_\phi = \frac{\sigma_1}{\sigma_3} = \frac{1 + \sin\phi}{1 - \sin\phi} \qquad (5.8)$$

$$= \tan^2(45°+\phi/2) = \tan^2\theta_{cr} \qquad (5.9)$$

The meaning of the Mohr-Coulomb failure law is demonstrated in Figure 5.2, where it can be seen that the theoretical failure plane lies at an angle of $(45°+\phi/2)$ to the plane on which the major principal stress acts.

The effect of Initial Void Ratio

The "friction angle ϕ is not a material property but depends strongly on the void ratio that existed prior to the application of the deviator stress." (Lambe and Whitman 1969, 144). The denser the sand the higher will be the value of the angle of internal friction (ϕ). The effect of void ratio on ϕ is explained by the phenomenon of interlocking. In addition, the higher the degree of compaction, the larger will be the expansion of the soil as it yields (dilatancy). These high compaction soils require the exertion of greater force on a steeper friction angle to effect shear in the soil.

If there were to be no volumetric change (dilatancy) in the dense granular soil element during the application of vertical stress, it will be necessary to have a considerable amount of confining stresses to prevent this volumetric change. If the particles in the soil mass are restricted from movement then the yield process is prevented from taking place and the soil element will have the capability of withstanding much higher stresses, which is not the case in normal road construction, where these confining conditions do not exist.

"The behavior at constant volume and the behavior with constant confining pressure can be tied together as follows. If a dense sand is to fail in shear, the high degree of interlocking must somehow be overcome. This can happen either (a) by shearing and fracturing of the particles, or (b) by increasing the volume. It will take more energy to cause either of these happenings than will be necessary simply to slide soil particles over a flat surface. If the soil is free to expand, the path of least resistance is to expand and so to overcome the interlocking in this way. If, however, the soil is impeded from expansion, the path of least resistance may lie in fracturing the soil particles," (Lambe and Whitman

1969, 143-144), which will occur only with the application of high stresses, not present in the pavement structures.

Application of the Stress/Strain Theory to the Research

In Chapter VI of this dissertation, we will move from the two-dimensional Mohr-Coulomb stress/strain theory, reviewed in this chapter, to the three-dimensional theory, employed in the Drucker-Prager failure criterion for granular soil analysis, used in this research. In Chapter VI the reader will also be introduced to the finite element methods that will be employed in the conduct of this three-dimensional analysis and by which mechanism the software used in this research will manage the voluminous equations that are involved in a three-dimensional analysis of this type.

CHAPTER VI

FINITE ELEMENT AND PLASTICITY THEORY SUPPORTING THE ANALYSIS

The referenced texts at the end of this chapter were used in the compilation of the material in this chapter. As a brief background to the plastic analysis done in this research, we will first start with the 2-dimensional state of stress and strain in a plane element and work towards the three-dimensional state. Much of the work covered in the plasticity theory in this chapter will be focused on the three-dimensional element.

Stress-Strain Relationships

Plane stress is defined as *"a state of stress in which the normal stress and shear stresses directed perpendicular to the plane are assumed to be zero."* (Logan 1986, 229).

Plane strain is defined as *"a state of strain in which the strain normal to the X-Y plane* ε_Z *and the shear strains* γ_{XZ} *and* γ_{YZ} *are assumed to be zero."* (Logan 1986, 230).

Figure 6.1 illustrates the 2-dimensional state of stress. The infinitesimal element which has sides of dimensions *dX* and *dY* has normal stresses σ_X and σ_Y acting perpendicular to the vertical and horizontal faces of the element in the X and Y directions, respectively. The shear stress τ_{XY} acts perpendicular to the normal stress σ_X along the *dY* face in an anti-clockwise manner, in the Y direction. The shear stress τ_{YX} acts perpendicular to the normal stress σ_Y along the *dX* face in a clockwise manner, in the X direction. (See Figure 6.1).

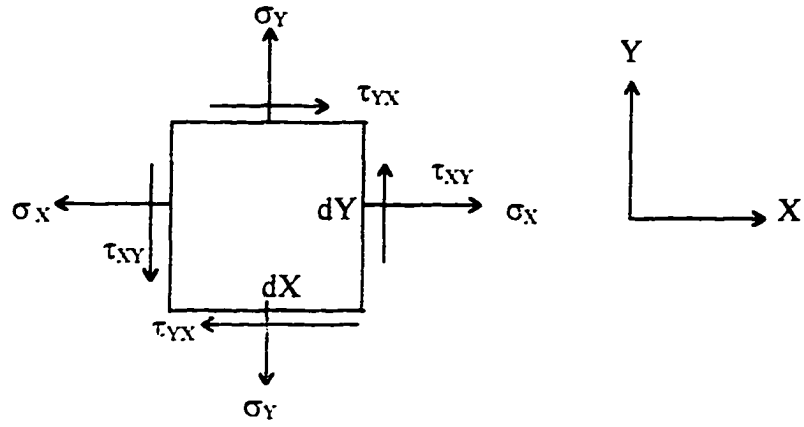

Figure 6.1

Two-dimensional state of stress[1]

Taking moments about the center of the element determines that moment equilibrium is achieved in this element and that $\tau_{XY} = \tau_{YX}$. We see in this element that three levels exist of stress, and which can be represented by the stress vector:

$$\{\sigma\} = \begin{Bmatrix} \sigma_X \\ \sigma_Y \\ \tau_{XY} \end{Bmatrix} \tag{6.1}$$

In plane stress/strain analysis, each node has two degrees of freedom and the stress determined from Equation (6.1) will be expressed in terms of these degrees of freedom.

We learn from Mechanics of Materials theory that the principal stresses which are inclined at the angle θ_p to the X-Y plane have principal normal stresses expressed as follows[1]:

$$\sigma_1 = \frac{\sigma_X + \sigma_Y}{2} + \sqrt{\left(\frac{\sigma_X + \sigma_Y}{2}\right)^2 + \tau_{XY}^2} = \sigma_{max} \tag{6.2}$$

$$\sigma_2 = \frac{\sigma_X + \sigma_Y}{2} - \sqrt{\left(\frac{\sigma_X + \sigma_Y}{2}\right)^2 + \tau_{XY}^2} = \sigma_{min} \qquad (6.3)$$

Also, θ_p defines the direction of the principal stress that is perpendicular to the plane on which either the maximum or minimum principal stress acts. Figure 6.2 shows the direction of the maximum and minimum principal stresses and the inclination of the planes on which these stresses act with respect to the X and Y coordinate axes. It should be noted that no shear stresses exist on the planes of principal stresses.

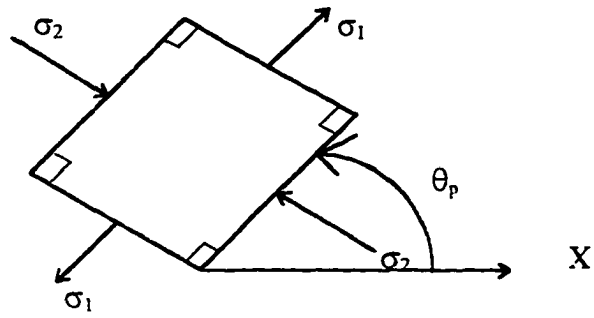

Figure 6.2

The principal stresses and their directions[1]

In developing the partial differential equations for the two-dimensional plane state of strain in a structure, let us look at the infinitesimal element that is subjected to plain strain in Figure 6.3. In the figure, the dotted lines represent the undeformed shape and the solid lines the deformed shape of the element (after straining has occurred). In this examination of plane strain, we will only consider small displacements in the continuum, with displacements u and v in the X and Y coordinate directions, respectively. We will assume that the displacements occur at point A of the element and that side AB extends in the X direction, an additional (incremental) amount of $(\partial u/\partial x)dX$ and similarly, side AC extends in the Y direction an additional (incremental) of amount $(\partial v/\partial y)dY$. Note that in

Figure 6.3, point B is displaced in the vertical Y direction a distance of $\partial v/\partial x)dX$ and that point C is displaced horizontally to the right, a distance of $(\partial u/\partial y)dY$. Both these movements are measured with respect to point A.

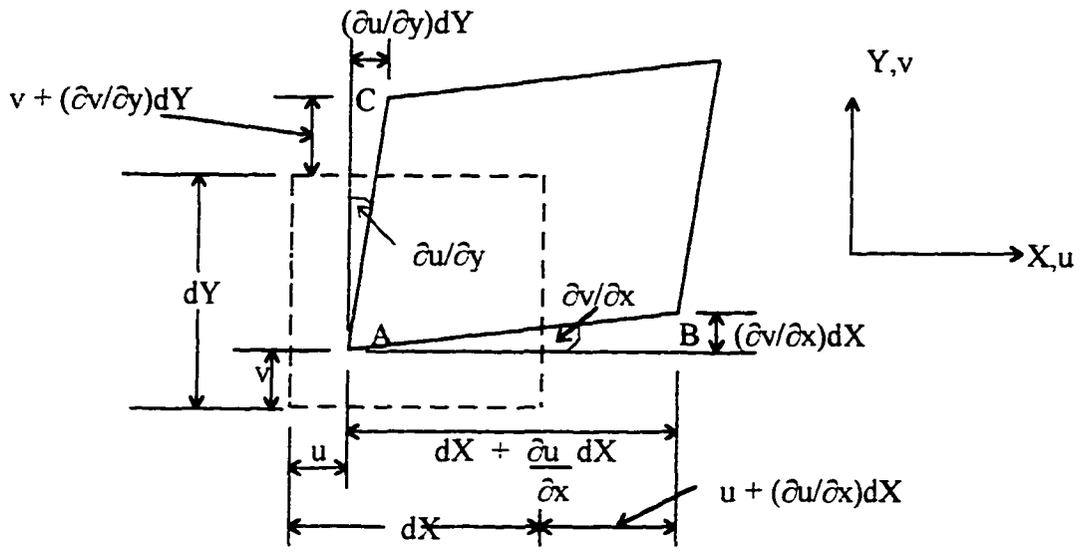

Figure 6.3

Displacements and measurements of an element in the X-Y plane[1].

For small deformations in the continuum, the longitudinal strain components in the X and Y directions are[1]:

$$\varepsilon_X = \partial u/\partial x \tag{6.4}$$

$$\varepsilon_Y = \partial v/\partial y \tag{6.5}$$

The shearing strain is[1]:

$$\gamma_{XY} = (\partial u/\partial y) + (\partial v/\partial x) \tag{6.6}$$

Writing these equations in matrix form we get[4]:

$$\begin{Bmatrix} \varepsilon_X \\ \varepsilon_X \\ \gamma_{XY} \end{Bmatrix} = \begin{bmatrix} \partial/\partial x & 0 & 0 \\ 0 & \partial/\partial y & 0 \\ \partial/\partial y & \partial/\partial x & 0 \end{bmatrix} \begin{Bmatrix} u \\ v \end{Bmatrix} \tag{6.7}$$

where:

$$\{\varepsilon\} = \begin{Bmatrix} \varepsilon_X \\ \varepsilon_Y \\ \gamma_{XY} \end{Bmatrix} \tag{6.8}$$

is the strain vector[1].

Uniaxial Stress

We know from the literature[2] that for a linearly elastic, homogeneous, isotropic material, uniaxial stress is represented by:

$$\sigma_X = E\,\varepsilon_X \tag{6.9}$$

where E is the modulus of elasticity.

For uniaxial stress, σ_X in a three-dimensional element, the strain in the Y and Z directions are not zero and can be represented by[2]:

$$\varepsilon_Y = \varepsilon_Z = -\nu\varepsilon_X \tag{6.10}$$

where ν is Poisson's ratio

Therefore;

$$\varepsilon_X = \frac{-\varepsilon_Y}{\nu} = \frac{-\varepsilon_Z}{\nu} \tag{6.11}$$

Plane Stress

For plane stress, in the three-dimensional element, the normal and shear stress components act in two directions only, as shown in Figure 6.1. We should note that in general, the longitudinal strain is non-zero in all coordinate directions, but that[2]:

$$\sigma_Z = \tau_{ZX} = \tau_{ZY} = 0 \tag{6.12}$$

and the shear strain[1];

$$\gamma_{XZ} = \gamma_{YZ} = 0 \tag{6.13}$$

but $\varepsilon_Z \neq 0$, because of the effect of Poisson's ratio.

For plane stress conditions we have[2]:

$$\{\sigma\} = [C]_\sigma\{\varepsilon\} \tag{6.14}$$

where:

$$\{\sigma\} = \begin{matrix}\sigma_x \\ \sigma_y \\ \tau_{xy}\end{matrix} \tag{6.15}$$

is the stress vector

and $[C]_\sigma$ = Constitutive matrix for plane stress.

In defining the components of the stress vector we have from the text[2];

$$\sigma_X = \frac{E}{1-\nu^2}(\varepsilon_X + \nu\varepsilon_Y) \tag{6.16}$$

$$\sigma_Y = \frac{E}{1-\nu^2}(\varepsilon_Y + \nu\varepsilon_X) \tag{6.17}$$

$$\tau_{XY} = G\gamma_{XY} \tag{6.18}$$

and $G = \dfrac{E}{2(1+\nu)}$ is known as the shear modulus

Using the above equations we can now write the constitutive equations in matrix form[2].

$$\begin{Bmatrix}\sigma_X \\ \sigma_Y \\ \tau_{XY}\end{Bmatrix} = \frac{E}{1-\nu^2}\begin{bmatrix}1 & \nu & 0 \\ \nu & 1 & 0 \\ 0 & 0 & \dfrac{1-\nu}{2}\end{bmatrix}\begin{Bmatrix}\varepsilon_X \\ \varepsilon_Y \\ \gamma_{XY}\end{Bmatrix} \tag{6.19}$$

where the constitutive matrix for plane stress is[2]:

$$[C]_\sigma = \frac{E}{1-\nu^2}\begin{bmatrix} 1 & \nu & 0 \\ \nu & 1 & 0 \\ 0 & 0 & \frac{1-\nu}{2} \end{bmatrix} \tag{6.20}$$

Now for plane strain, we assume the following to be zero[1]:

$$\varepsilon_Z = \gamma_{XZ} = \gamma_{YZ} = 0 \tag{6.21}$$

Applying Equation (6.21) to case for plane strain in the three dimensional element, where;

$$\tau_{XZ} = \tau_{YZ} = 0 \tag{6.22}$$

but $\sigma_Z \neq 0$, (the value necessary to keep the linear strain in the Z direction at the value zero[2]).

From the text we find that the stress-strain Equations for the plane state are[2];

$$\sigma_X = \frac{E}{(1+\nu)(1-2\nu)}[(1-\nu)\varepsilon_X + \nu\varepsilon_Y] \tag{6.23}$$

$$\sigma_Y = \frac{E}{(1+\nu)(1-2\nu)}[\nu\varepsilon_X + (1-\nu)\varepsilon_Y] \tag{6.24}$$

$$\sigma_Z = \frac{E}{(1+\nu)(1-2\nu)}[\nu\varepsilon_X + \nu\varepsilon_Y] = \nu(\sigma_X + \sigma_Y) \tag{6.25}$$

$$\tau_{XY} = G\gamma_{XY} \tag{6.26}$$

Note that for plane strain, σ_Z is defined solely in terms of σ_X, σ_Y and ν.

Equation (6.21) shows that $\varepsilon_Z = 0$

If we were to write these X–Y Plane relationships in matrix form for plane strain in the three-dimensional element, we get[2]:

$$\begin{Bmatrix} \sigma_X \\ \sigma_Y \\ \tau_{XY} \end{Bmatrix} = \frac{E}{(1+\nu)(1-2\nu)} \begin{bmatrix} 1-\nu & \nu & 0 \\ \nu & 1-\nu & 0 \\ 0 & 0 & \frac{1-2\nu}{2} \end{bmatrix} \begin{Bmatrix} \varepsilon_X \\ \varepsilon_Y \\ \gamma_{XY} \end{Bmatrix} \quad (6.27)$$

or

$$\{\sigma\} = [C]_\varepsilon\{\varepsilon) \quad (6.28)$$

where the constitutive matrix for plane strain is[2]:

$$[C]_\varepsilon = \frac{E}{(1+\nu)(1-2\nu)} \begin{bmatrix} 1-\nu & \nu & 0 \\ \nu & 1-\nu & 0 \\ 0 & 0 & \frac{1-2\nu}{2} \end{bmatrix} \quad (6.29)$$

Three-Dimensional Stress

Let us extend the two-dimensional strain theory to the three-dimensional case, and consider small strains in the three-dimensional continuum. If *u*, *v* and *w* represent the displacement components of a point along the X, Y and Z coordinate axes in the continuum, the respective longitudinal strains will be[2]:

$$\varepsilon_X = \frac{\partial u}{\partial x}$$

$$\varepsilon_Y = \frac{\partial v}{\partial y} \quad (6.30)$$

$$\varepsilon_Z = \frac{\partial w}{\partial z}$$

and the shearing strains are:

$$\gamma_{XY} = \frac{\partial u}{\partial y} + \frac{\partial v}{\partial x}$$

$$\gamma_{YZ} = \frac{\partial v}{\partial z} + \frac{\partial w}{\partial y} \qquad (6.31)$$

$$\gamma_{ZX} = \frac{\partial w}{\partial x} + \frac{\partial u}{\partial z}$$

Putting the previous six equations into matrix form, we get[2]:

$$\begin{Bmatrix} \varepsilon_X \\ \varepsilon_Y \\ \varepsilon_Z \\ \gamma_{XY} \\ \gamma_{YZ} \\ \gamma_{ZX} \end{Bmatrix} = \begin{bmatrix} \frac{\partial}{\partial x} & 0 & 0 \\ 0 & \frac{\partial}{\partial y} & 0 \\ 0 & 0 & \frac{\partial}{\partial z} \\ \frac{\partial}{\partial y} & \frac{\partial}{\partial x} & 0 \\ 0 & \frac{\partial}{\partial z} & \frac{\partial}{\partial y} \\ \frac{\partial}{\partial z} & 0 & \frac{\partial}{\partial x} \end{bmatrix} \begin{Bmatrix} u \\ v \\ w \end{Bmatrix} \qquad (6.32)$$

Now applying a modified Equation 6.22 in the three dimensional case where now, $\tau_{XZ} = \tau_{YZ} \neq 0$, and $\sigma_Z \neq 0$, we obtain a similar stress-strain relationship, as in Equation (6.14) for an isotropic material[1]:

$$\{\sigma\} = [C]\{\varepsilon) \qquad (6.33)$$

where [C] is the elastic constitutive matrix for an isotropic material. [Isotropic in the sense that $E_X = E_Y = E_Z = E$ and $\nu_X = \nu_Y = \nu_Z = \nu$]:

$$[C] = \frac{E}{(1+\nu)(1-2\nu)}\begin{bmatrix} 1-\nu & \nu & \nu & 0 & 0 & 0 \\ & 1-\nu & \nu & 0 & 0 & 0 \\ & & 1-\nu & 0 & 0 & 0 \\ & & & \frac{1-2\nu}{2} & 0 & 0 \\ & & \text{Symmetry} & & \frac{1-2\nu}{2} & 0 \\ & & & & & \frac{1-2\nu}{2} \end{bmatrix} \tag{6.34}$$

We can now compile the constitutive equations for the three-dimensional element[1]:

$$\begin{Bmatrix} \sigma_X \\ \sigma_Y \\ \sigma_Z \\ \tau_{XY} \\ \tau_{YZ} \\ \tau_{ZX} \end{Bmatrix} = \frac{E}{(1+\nu)(1-2\nu)}\begin{bmatrix} 1-\nu & \nu & \nu & 0 & 0 & 0 \\ & 1-\nu & \nu & 0 & 0 & 0 \\ & & 1-\nu & 0 & 0 & 0 \\ & & & \frac{1-2\nu}{2} & 0 & 0 \\ & & \text{Symmetry} & & \frac{1-2\nu}{2} & 0 \\ & & & & & \frac{1-2\nu}{2} \end{bmatrix} \begin{Bmatrix} \varepsilon_X \\ \varepsilon_Y \\ \varepsilon_Z \\ \gamma_{XY} \\ \gamma_{YZ} \\ \gamma_{ZX} \end{Bmatrix} \tag{6.35}$$

Figure 6.4 below, taken from Reference 3, Chapter 1, shows the components of the three-dimensional stress tensor, and depicts the state of stress at a point P in a continuous medium. The normal stress on the surface of the differential element at point *P* in Figure 6.4, parallel to the *X* axis is depicted by σ_X. The components of the shearing stress on the surface element normal to the X axis in the *Y* and *Z* directions are depicted by τ_{XY} and τ_{XZ}, respectively. In similar manner, the normal and shearing stresses acting on

surface elements normal to the *Y* and *Z* axes will be denoted by σ_Y, τ_{YX}, τ_{YZ}, *and* σ_Z, τ_{ZX}, τ_{ZY}, respectively. These nine quantities are called the components of the stress tensor[3]. (See Figure 6.4).

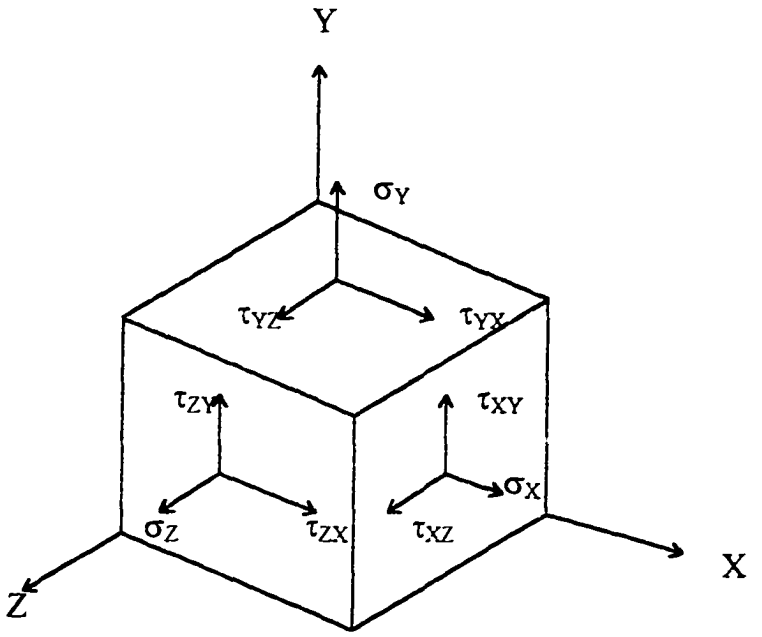

Figure 6.4

Components of the Stress Tensor[3].

In Reference 1, Appendix C, we examine the equilibrium state of a plane element of unit thickness, subjected to normal stresses σ_X and σ_y and in-plane shear stress τ_{XY} (in units of force/unit area) with applied body forces F_{Xb} and F_{Yb} (in units of force per unit volume). With constant stress across the vertical face dY in Figure 6.5 and with a variation of stress as it travels from the subject face to the opposite face, we have in Figure 6.5 the stresses σ_X on the left vertical face of the infinitesimal element and stress $\sigma_X + (\partial\sigma_X/\partial x)dX$ on the opposite face.

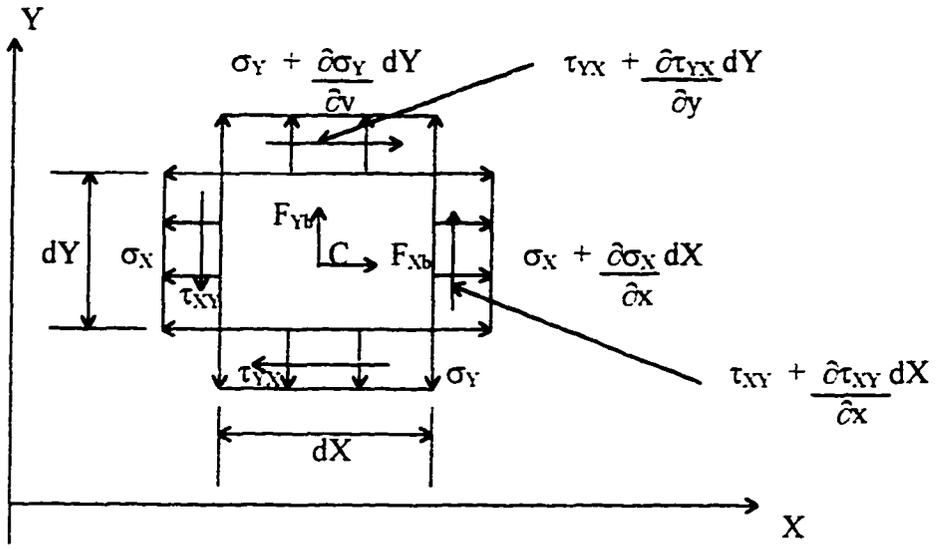

Figure 6.5

Plane differential element subjected to plane stresses[1]

Referring to Figure 6.5, if we sum forces in the X direction, we get:

$$\Sigma F_X = 0 = \left(\sigma_X + \frac{\partial \sigma_X}{\partial x} dX\right) dY\,(1) - \sigma_X\, dY\,(1) + F_{Xb}\, dX\, dY\,(1) + \left(\tau_{YX} + \frac{\partial \tau_{YX}}{\partial y} dY\right) dX\,(1) - \tau_{YX}\, dX\,(1) = 0 \qquad (6.36)$$

Simplifying Equation (6.37) we get:

$$\Sigma F_X = \frac{\partial \sigma_X}{\partial x} + \frac{\partial \tau_{YX}}{\partial y} + F_{Xb} = 0 \qquad (6.37)$$

Similarly summing forces for the Y direction and simplifying, we get:

$$\Sigma F_Y = \frac{\partial \sigma_Y}{\partial y} + \frac{\partial \tau_{XY}}{\partial x} + F_{Yb} = 0 \qquad (6.38)$$

The text went on to show that by taking moments about C of this planar element and neglecting higher order terms, the third equilibrium equation is satisfied, and:

$$\tau_{XY} = \tau_{YX} \qquad (6.39)$$

Similarly: $\tau_{XZ} = \tau_{ZX}$ $\tau_{YZ} = \tau_{ZY}$ (6.40)

The Three-Dimensional Stress Tensor

If we were to consider the three-dimensional state of stress in the stress tensor in Figure 6.4 and add coordinate forces F_{Xb}, F_{Yb} and F_{Zb} acting at the center of the element, we get in Figure 6.6 the components of the stress tensor with three-dimensional body forces.

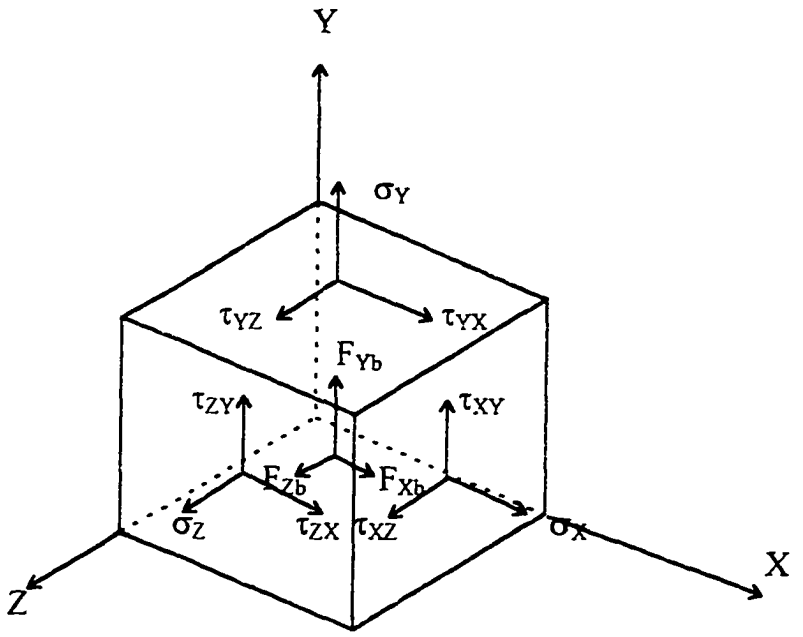

Figure 6.6
Components of the stress tensor with 3-D body forces[1], [3].

We find in the text, that we can extend the two-dimensional equilibrium Equations (6.37) and (6.38) to satisfy the three-dimensional case and obtain:

$$\frac{\partial \sigma_X}{\partial x} + \frac{\partial \tau_{YX}}{\partial y} + \frac{\partial \tau_{ZX}}{\partial z} + F_{Xb} = 0 \qquad (6.41)$$

$$\frac{\partial \tau_{XY}}{\partial x} + \frac{\partial \sigma_Y}{\partial y} + \frac{\partial \tau_{ZY}}{\partial z} + F_{Yb} = 0 \qquad (6.42)$$

$$\frac{\partial \tau_{XZ}}{\partial x} + \frac{\partial \tau_{YZ}}{\partial y} + \frac{\partial \sigma_Z}{\partial z} + F_{Zb} = 0 \qquad (6.43)$$

and; $\tau_{XY} = \tau_{YX}$ $\tau_{XY} = \tau_{YX}$ $\tau_{XY} = \tau_{YX}$ (6.44)

PLASTICITY THEORY APPLICABLE TO THE GRANULAR SOILS ANALYSIS USED IN THE RESEARCH

The Yield Criterion

This section of the chapter is dedicated to gathering work already done in plasticity theory that is applicable to the theoretical analysis of the granular soil types used in this research. Plasticity theory provides a mathematical relationship, that characterizes the elasto-plastic response of materials[6]. The computer application used in this research, (ANSYS) in employing the use of plasticity theory with respect to failure in granular soils, uses the Drucker-Prager yield criterion. The Researcher felt it appropriate to gather the theory from the various texts under one cover for a structured development of the theory used in the ANSYS program. It was felt that in so doing, it would enable the reader to have a better understanding of the computer application and its usefulness in this research. From the text[6], the Drucker-Prager option uses the outer cone approximation to the Mohr-Coulomb Law. The following is a development of the theory that supported the analysis in this dissertation and which contains the theory included in the Haigh-Westergaard, Mohr-Coulomb and Drucker-Prager yield criteria.

In Reference 6 it is stated that "plasticity theory provides a mathematical relationship that characterizes the elasto-plastic response of materials." (p4-4). "In the plastic range, the total strain may be considered as the sum of the *elastic strain* and the

plastic or permanent strain, the latter being the strain observed after complete unloading of the volume element under consideration." (Prager and Hodge, p27).

"The Yield Criterion establishes the stress level at which yielding is initiated. For multi-component stresses, this is represented as a function of the individual components, $f(\{\sigma\})$, which can be interpreted as an equivalent stress σ_e:" (ANSYS User's Manual, Vol. IV, Theory, p4-4).

$$\sigma_e = f(\{\sigma\}) \tag{6.45}$$

where: $\{\sigma\}$ = stress vector in Equation (6.33)

$$= \begin{Bmatrix} \sigma_X \\ \sigma_Y \\ \sigma_Z \\ \tau_{XY} \\ \tau_{YZ} \\ \tau_{ZX} \end{Bmatrix}$$

In Reference 4 it is stated that the material yield parameter (σ_p) is equal to the material equivalent stress (σ_e), that is:

$$f(\{\sigma\}) = \sigma_e = \sigma_p \tag{6.46}$$

and the material develops plastic strains. If σ_e is less than σ_p the range is elastic and stress/strain relationships will follow the rules of the elastic relationship. The literature[6] went on to say that the material equivalent stress cannot exceed the material yield stress as plastic strains will develop immediately and reduce material stresses to yield stresses only[6].

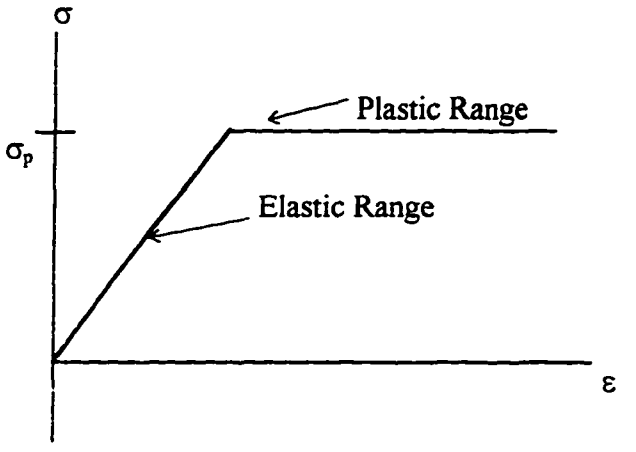

Figure 6.7

Stress-strain behavior of the Drucker-Prager option[6]

In Figure 6.7, depicts the stress-strain behavior of the Drucker-Prager option used by the ANSYS program for granular soil analysis in which the following relationships pertain[6]:

$$\sigma_p = f(\sigma_m) \tag{6.47}$$

where: σ_m = mean stress

$$= 1/3(\sigma_X + \sigma_Y + \sigma_Z) \tag{6.48}$$

The analysis pursued in this research considered the soil mass undergoing rate independent plasticity when the utility cut is made. "Rate independent plasticity is characterized by the irreversible straining that occurs in a material once a certain level of stress is reached. The plastic strains are assumed to develop instantaneously, that is, independent of time." (ANSYS User's Manual, Vol. IV, Theory, p4-4).

For plastic failure in granular materials, the yielding of the material is not as straight-forward as it is for metals and requires modifications as included in the Mohr-Coulomb failure criteria and the Drucker-Prager failure criteria theory and applications. The following is a review of the failure criteria employed in this research.

Mohr-Coulomb Failure Criterion

The Mohr-Coulomb failure criteria is "...based on the assumption that the maximum shear stress is the only decisive measure of impending failure." (Chen and Han 1988, 88). Mohr in his theory considered "the limiting shear stress (τ) in a plane to be a function of the normal stress (σ) in the same plane at a point, i.e."

$$|\tau| = f(\sigma) \tag{6.49}$$

Using straight line relationship referred to in Chapter V, we have the straight line envelope, known as the Coulomb's equation, since 1877 (Chen and Han 1988, 90):

$$|\tau| = c - \sigma \tan \phi \tag{6.50}$$

in which c is the cohesion and ϕ the internal angle of friction, both material constants determined by experiment. (See Figure 6.8).

Using Equation (6.50) and for $\sigma_1 \geq \sigma_2 \geq \sigma_3$ the Mohr-Coulomb criterion is represented in the text as follows[4]:

$$1/2\ (\sigma_1 - \sigma_3) \cos \phi = c - [1/2\ (\sigma_1 + \sigma_3) + \{1/2\ (\sigma_1 - \sigma_3) \sin \phi\}] \tan \phi \tag{6.51}$$

If we were to re-arrange Equation (6.51), we will get[4]

$$\sigma_1 \frac{1 + \sin \phi}{2c \cos \phi} - \sigma_3 \frac{1 - \sin \phi}{2c \cos \phi} = 1 \tag{6.52}$$

where we can define the strength in simple compression ($\sigma_1 = 0$) as:

$$f'_c = \frac{2c \cos \phi}{1 - \sin \phi} \tag{6.53}$$

and the strength in simple tension ($\sigma_3 = 0$) as

$$f'_t = \frac{2c \cos \phi}{1 + \sin \phi} \tag{6.54}$$

Equation (6.52) can now be reduced to

$$\frac{\sigma_1}{f_t} - \frac{\sigma_3}{f_c} = 1 \qquad \text{for } \sigma_1 \geq \sigma_2 \geq \sigma_3 \qquad (6.55)$$

we can obtain a straight line relationship from Equation (6.55) and write it in the slope-intercept form by multiplying both sides by f'_c and obtain the slope

$$m = \frac{f'_c}{f_t} = \frac{1 + \sin\phi}{1 - \sin\phi} \qquad (6.56)$$

Substituting Equation (6.56) into Equation (6.55) and putting it into slope-intercept form, we get:

$$m\sigma_1 - \sigma_3 = f'_c \qquad \text{for } \sigma_1 \geq \sigma_2 \geq \sigma_3 \qquad (6.57)$$

Figure 6.8 shows the Mohr-Coulomb criterion with the straight line failure envelope[4].

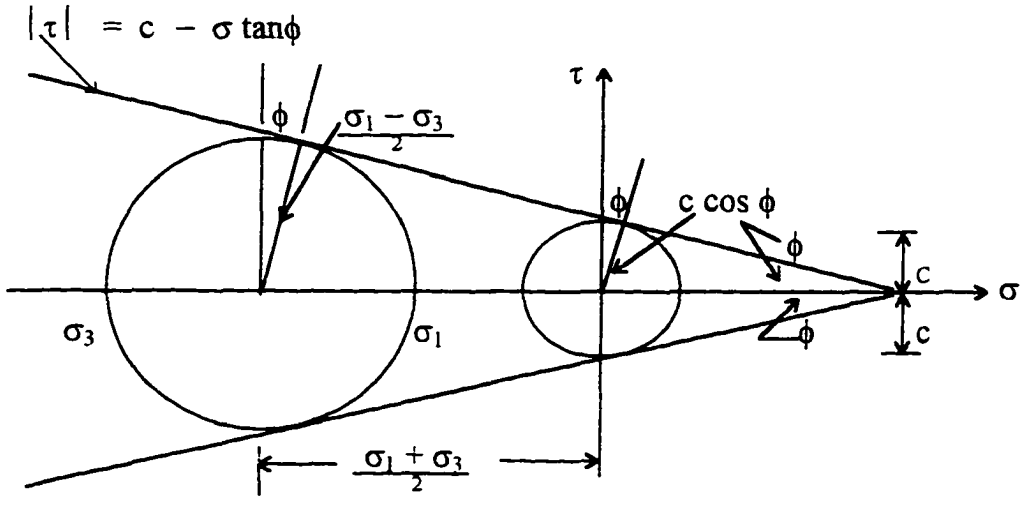

Figure 6.8

The Mohr-Coulomb criterion, with a straight line as the failure envelope[4]

In order to plot the three-dimensional failure surface of the Mohr-Coulomb failure criterion, let us first develop the relationships pertinent to this criterion.

From the text (Chen and Han 1988, 63), we know that if the stress tensor is referenced to the principal axes the mean stress is defined as:

$$\sigma_m = 1/3(\sigma_X + \sigma_Y + \sigma_Z) = 1/3I_1 \quad (6.58)$$

$$\text{For } I_1 = \sigma_X + \sigma_Y + \sigma_Z \quad (6.59)$$

(the sum of the diagonal terms of σ_{ij})

$$= \sigma_{11} + \sigma_{22} + \sigma_{33} \quad (6.60)$$

It is stated in the text that "... the mean stress is an invariant of the stress tensor," (Prager and Hodge p15) and "...it is apparent that σ_m is the same for all possible orientations of the axes; hence, it is called the *spherical or hydrostatic stress.*" (Chen and Han 1988, 57). The text went on to say that the stress deviator tensor s_{ij} is the result of the subtraction of the spherical state of stress from the actual state of stress. We thus have;

$$s_{ij} = \sigma_{ij} - \sigma_m\delta_{ij} \quad (6.61)$$

where $\sigma_m\delta_{ij}$ is referred to as the spherical state of stress

It should be noted that for $i \neq j$ in Equation (6.61), $\delta_{ij} = 0$ and $s_{ij} = \sigma_{ij}$.

The components of the stress deviator tensor is

$$s_{ij} = \begin{bmatrix} s_{11} & s_{12} & s_{13} \\ s_{21} & s_{22} & s_{23} \\ s_{31} & s_{32} & s_{33} \end{bmatrix} = \begin{bmatrix} (\sigma_{11} - \sigma_m) & \sigma_{12} & \sigma_{13} \\ \sigma_{21} & (\sigma_{22} - \sigma_m) & \sigma_{23} \\ \sigma_{31} & \sigma_{31} & (\sigma_{33} - \sigma_m) \end{bmatrix} \quad (6.62)$$

which in Von Karman's notation is[4]

$$s_{ij} = \begin{bmatrix} s_X & s_{XY} & s_{XZ} \\ s_{YX} & s_Y & s_{YZ} \\ s_{ZX} & s_{ZY} & s_Z \end{bmatrix} = \begin{bmatrix} (\sigma_X - \sigma_m) & \tau_{XY} & \tau_{XZ} \\ \tau_{YX} & (\sigma_Y - \sigma_m) & \tau_{YZ} \\ \tau_{ZX} & \tau_{ZY} & (\sigma_Z - \sigma_m) \end{bmatrix} \quad (6.63)$$

If we were to subtract a constant normal stress in all directions it will not change the principal directions, hence the principal stresses will be the same for the stress deviator tensor as for the original tensor. In terms of the principal stresses, the stress deviator tensor is represented in Equation (6.64) as follows[4]:

$$s_{ij} = \begin{bmatrix} (\sigma_X - \sigma_m) & 0 & 0 \\ 0 & (\sigma_Y - \sigma_m) & 0 \\ 0 & 0 & (\sigma_Z - \sigma_m) \end{bmatrix} \quad (6.64)$$

or

$$s_{ij} = \begin{bmatrix} \frac{(2\sigma_1 - \sigma_2 - \sigma_3)}{3} & 0 & 0 \\ 0 & \frac{(2\sigma_2 - \sigma_3 - \sigma_1)}{3} & 0 \\ 0 & 0 & \frac{(2\sigma_3 - \sigma_1 - \sigma_2}{3} \end{bmatrix} \quad (6.65)$$

The text indicated the method to be employed in order to obtain the invariants of the stress tensor (Chen and Han 1988, 52-54). The text developed relationships among the 3 stress invariants in terms of the principal stresses, and which are expressed as follows:

$$I_1 = \sigma_1 + \sigma_2 + \sigma_3 \quad (6.66)$$

$$I_2 = \sigma_1\sigma_2 + \sigma_2\sigma_3 + \sigma_3\sigma_1 \quad (6.67)$$

$$I_3 = \sigma_1\sigma_2\sigma_3 \quad (6.68)$$

The value of these invariants are not impacted by any rotation of the axes.

The text further indicated the method to be employed in order to obtain the three invariants (J_1, J_2 and J_3) of the stress deviator tensor, (Chen and Han 1988, 58). The text showed that these invariants are related to the invariants of the stress tensor as follows:

$$J_1 = 0 \quad \text{(always)} \tag{6.69}$$

$$J_2 = 1/3(I_1^2 - 3I_2) \tag{6.70}$$

$$J_3 = 1/27(2I_1^3 - 9I_1I_2 + 27I_3) \tag{6.71}$$

For the development of the three-dimensional failure surface, we are interested in J_2 (known as the octahedral shear stress). From the text[4], we find the relationship between J_2 and the principal stresses as follows

$$J_2 = 1/6[(\sigma_1 - \sigma_2)^2 + (\sigma_2 - \sigma_3)^2 + (\sigma_3 - \sigma_1)^2] \tag{6.72}$$

or in terms of the principal stresses of the stress deviator tensor[4]

$$J_2 = 1/2(s_1^2 + s_2^2 + s_3^2) \tag{6.73}$$

(Chen and Han 1988, 58-63).

The Haigh-Westergaard Failure Criterion

In developing the Mohr-Coulomb failure criterion the text showed its relationship to the Haigh-Westergaard criteria (Chen and Han 1988, 66-70). Haigh-Westergaard took the three principal stresses σ_1, σ_2, σ_3 and represented them as coordinates originating from a point in stress space. This stress space representation was basically concerned with the geometry of the stress state and not on the orientation of the coordinate stress axes with respect to the body. The Haigh-Westergaard stress space is reproduced in Figure (6.9) (Chen and Han 1988, 67).

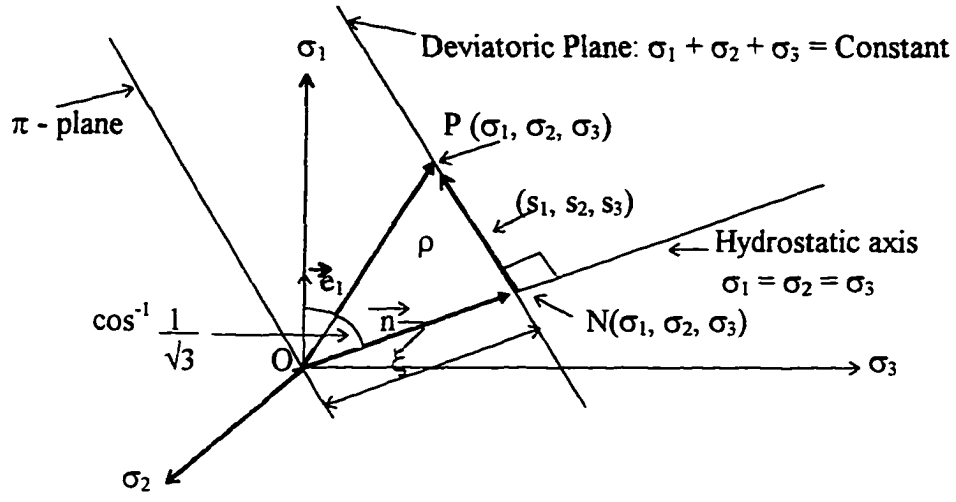

Figure 6.9

Plot of the Haigh-Westergaard stress space[4]

In Figure 6.9 the line ON passes through the origin and makes the same angle with each of the coordinate axes. Therefore, for every point on this line $\sigma_1 = \sigma_2 = \sigma_3$ and corresponds to an hydrostatic or spherical state of stress. The deviatoric stresses for this state in Equation (6.65), (e.g. $s_1 = 2\sigma_1 - \sigma_2 - \sigma_3$) are all equal to zero. ON can be referred to here as the hydrostatic axis and any plane perpendicular to it is referred to as a deviatoric plane. From Chen, such a deviatoric plane has the form

$$\sigma_1 + \sigma_2 + \sigma_3 = \sqrt{3}\,\xi \qquad (6.74)$$

where ξ is the distance from the origin to the plane measured along the normal **ON**.

The text went on to show that the particular deviatoric plane passing through the origin *o* has a stress state such that

$$\sigma_1 + \sigma_2 + \sigma_3 = 0 \qquad (6.75)$$

and is referred to as the *π-plane*.

Before we continue with the development of the Mohr-Coulomb failure criterion which is based on the Haigh-Westergaard criterion let us discuss the relationships in Figure 6.9. (Chen and Han 1988, 66-68).

Consider an arbitrary state of stress at point P in stress space with stress components σ_1, σ_2, σ_3, such that the state of stress is represented by point P(σ_1, σ_2, σ_3). (See Figure 6.9). If we decompose the stress OP into two components we get;

ON in the direction of the unit vector $\vec{n} = (1/\sqrt{3}, 1/\sqrt{3}, 1/\sqrt{3})$

and

The component **NP** which is perpendicular to **ON** and parallel to the π-plane.

Now

$$|\mathbf{ON}| = \mathbf{OP} \bullet \mathbf{n} = (\sigma_1, \sigma_2, \sigma_3) \bullet (1/\sqrt{3}, 1/\sqrt{3}, 1/\sqrt{3}) \quad (6.76)$$

$$= 1/\sqrt{3}(\sigma_1 + \sigma_2 + \sigma_3) = I/\sqrt{3} = \sqrt{3}\,\sigma_m \quad (6.77)$$

Putting NP in its component form, we get:

$$\mathbf{NP} = \mathbf{OP} - \mathbf{ON} \quad (6.78)$$

But $$\mathbf{ON} = |\mathbf{ON}|\,\mathbf{n} = (\sigma_m, \sigma_m, \sigma_m) \quad (6.79)$$

Substituting Equation (6.79) into Equation (6.78) we get

$$\mathbf{NP} = (\sigma_1, \sigma_2, \sigma_3) - (\sigma_m, \sigma_m, \sigma_m) = (\sigma_1 - \sigma_m), (\sigma_2 - \sigma_m), (\sigma_3 - \sigma_m) \quad (6.80)$$

and from Equation (6.62) reduces to

$$\mathbf{NP} = (s_1, s_2, s_3) \quad (6.81)$$

See Equation (6.73).

Hence for a length of vector NP = ρ we get:

$$\rho = |\mathbf{NP}| = (s_1^2 + s_2^2 + s_3^2)^{1/2} = \sqrt{2J_2} \quad (6.82)$$

"The vectors **ON** and **NP** represent the hydrostatic components ($p\delta_{ij}$) and the deviatoric stress components (s_{ij}), respectively, of the state of stress (σ_{ij}) represented by point P," (Chen and Han 1988, 68).

Chen demonstrated in the text that if we were to consider the projection of vector NP and the coordinate axes σ_i on a deviatoric plane to form new deviatoric axes σ'_1, σ'_2, σ'_3, the projection of NP on the deviatoric plane is as shown in Figure 6.10. "In this figure the axes σ'_1, σ'_2, σ'_3 are deviatoric projections of the axes σ_1, σ_2, σ_3 on the deviatoric plane, and NP is the projection of vector **NP** on the same plane." (Chen, p68).

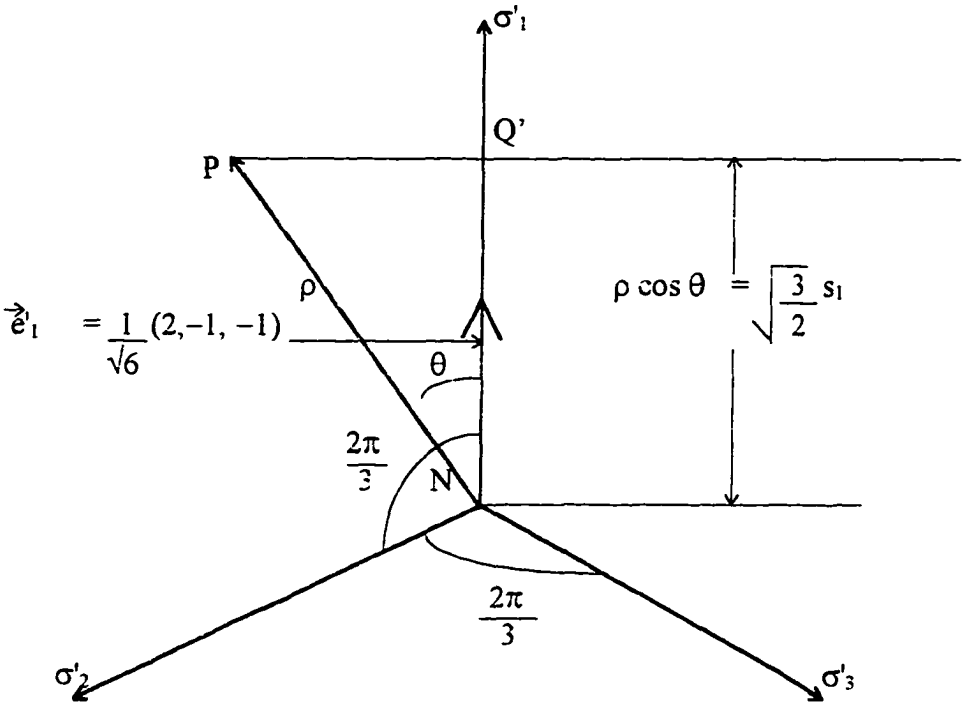

Figure 6.10

The Haigh-Westergaard stress state at a point projected on a deviatoric plane[4]

Unit vector e'_i is in the direction of the σ'_1 axis and has components

$1/\sqrt{6}\ (2, -1, -1)$ with respect to axes σ_1, σ_2, and σ_3. Therefore, the projection of vector NP on the σ'_1 axis is represented as:

$$NQ = NP\cos\theta = \rho\cos\theta = NP \bullet e'_i$$

$$= (s_1, s_2, s_3) \bullet 1/\sqrt{6}\ (2, -1, -1) \tag{6.83}$$

or:

$$\rho\cos\theta = 1/\sqrt{6}\ (2s_1, -s_2, -s_3) \tag{6.84}$$

and substituting $s_2 + s_3 = -s_1$ we get

$$\rho\cos\theta = \sqrt{\frac{3}{2}}\ s_1 \tag{6.85}$$

Substituting Equation (6.80) into Equation (6.83) we get:

$$\cos\theta = \frac{\sqrt{3}}{2}\ \frac{s_1}{\sqrt{J_2}} \tag{6.86}$$

we then have

$$s_1 = \frac{2}{\sqrt{3}}\sqrt{J_2}\cos\theta \tag{6.87}$$

$$s_2 = \frac{2}{\sqrt{3}}\sqrt{J_2}\cos(2\pi/3 - \theta) \tag{6.88}$$

$$s_3 = \frac{2}{\sqrt{3}}\sqrt{J_2}\cos(2\pi/3 + \theta) \tag{6.89}$$

Equations (6.87), (6.88), and (6.89) are only satisfied if $\sigma_1 \geq \sigma_2 \geq \sigma_3$ and the angle (θ) lies in the range

$$0 \leq \theta \leq \pi/3 \tag{6.90}$$

Chen went on from these trigonometrical relationships for the state of stress on a deviatoric plane depicted in Figure 6.10 and expressed the three principal stresses of σ_{ij} as

$$\begin{Bmatrix} \sigma_1 \\ \sigma_2 \\ \sigma_3 \end{Bmatrix} = \begin{Bmatrix} \sigma_m \\ \sigma_m \\ \sigma_m \end{Bmatrix} + \frac{2}{\sqrt{3}} \sqrt{J_2} \begin{Bmatrix} \cos\theta \\ \cos(2\pi/3 - \theta) \\ \cos(2\pi/3 + \theta) \end{Bmatrix} \tag{6.91}$$

and in terms of the Haigh-Westergaard stress space where (σ_1, σ_2, σ_3) are expressed in terms their coordinates (ξ, ρ, θ), the text (Chen and Han 1988, 70) shows that Equation 6.85 can be expressed in terms of the Haigh-Westergaard parameters as

$$\begin{Bmatrix} \sigma_1 \\ \sigma_2 \\ \sigma_3 \end{Bmatrix} = \frac{1}{\sqrt{3}} \begin{Bmatrix} \xi \\ \xi \\ \xi \end{Bmatrix} + \sqrt{\frac{2}{3}}\, \rho \begin{Bmatrix} \cos\theta \\ \cos(\theta - 2\pi/3) \\ \cos(\theta + 2\pi/3) \end{Bmatrix} \tag{6.92}$$

The Mohr-Coulomb Failure Criterion (Cont'd)

In resuming our discussions on the Mohr-Coulomb failure criterion, if we take Equation (6.91) and rewrite Equation (6.52), we can demonstrate the shape of the 3-D failure surface of the Mohr-Coulomb failure criterion as follows:

$$f(I_1, J_2, \theta) = \frac{1}{3} I_1 \sin\phi + \sqrt{J_2} \sin\left(\theta + \frac{\pi}{3}\right) + \frac{\sqrt{J_2}}{\sqrt{3}} \cos\left(\theta + \frac{\pi}{3}\right) \sin\phi - c\cos\phi = 0 \tag{6.93}$$

or, using Equation (6.92) and rewriting Equation (6.52) we get

$$f(\xi, \rho, \theta) = \sqrt{2}\,\xi \sin\phi + \sqrt{3}\,\rho \sin\left(\theta + \frac{\pi}{3}\right) + \rho\cos\left(\theta + \frac{\pi}{3}\right) \sin\phi - \sqrt{6}c\cos\phi = 0 \tag{6.94}$$

for $0 \le \theta \le \pi/3$.

Chen showed that in stress space Equation (6.94) gives an irregular hexagonal pyramid with straight line meridians. (See Figure 6.11a). Its cross section in the π plane is an irregular hexagon. (See Figure 6.11b). The two requirements to plot the hexagon are ρ_{to} and ρ_{co} which can be obtained from Equation (6.94). For $\xi = 0$ and $\theta = 0$, $\rho = \rho_{to}$ and for $\xi = 0$ and $\theta = 60°$, $\rho = \rho_{co}$.

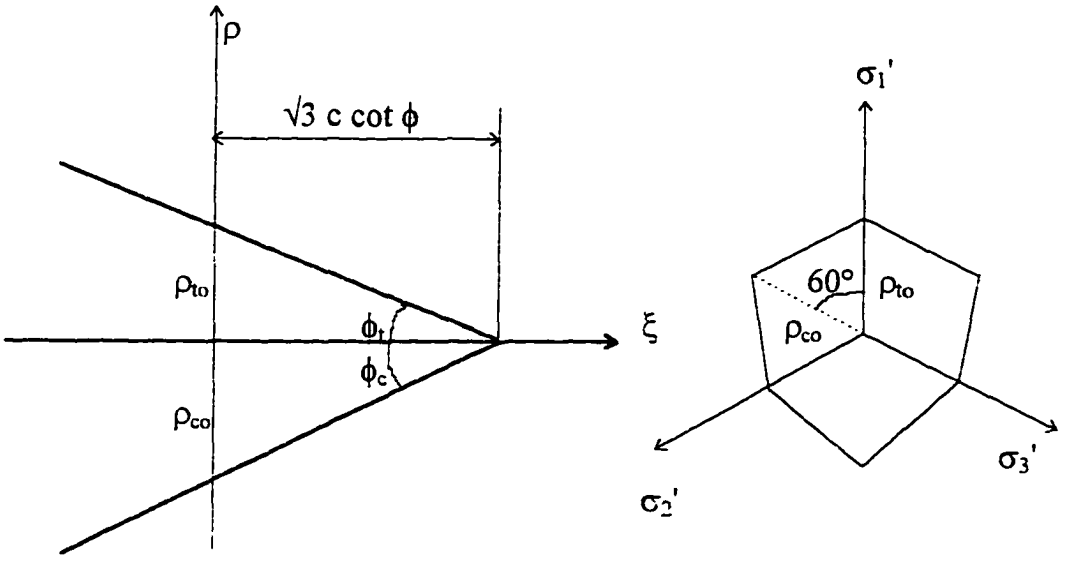

(a) Meridian Plane $\theta = 0$ (b) π–Plane

Figure 6.11

Graphical representation of Mohr-Coulomb criterion in principal stress space[4].

If we were to use Equations (6.94), (6.53) and (6.54), we will get the following alternative forms for ρ_{to} and ρ_{co} on the π–plane:

$$\rho_{to} = \frac{2\sqrt{6}c\cos\phi}{3+\sin\phi} = \frac{\sqrt{6}f'c(1-\sin\phi)}{3+\sin\phi} \qquad (6.95)$$

$$\rho_{co} = \frac{2\sqrt{6}c\cos\phi}{3-\sin\phi} = \frac{\sqrt{6}f'c(1-\sin\phi)}{3-\sin\phi} \qquad (6.96)$$

The ratio of these lengths is

$$\frac{\rho_{to}}{\rho_{co}} = \frac{3 - \sin\phi}{3 + \sin\phi} \tag{6.97}$$

Chen went on to show in his text that for a variety of ϕ angles a family of Mohr-Coulomb cross sections can be plotted on the π-Plane. He further stated that the Mohr-Coulomb criterion is a three-parameter criterion requiring c, ϕ and a stress state to determine the maximum tensile stress.

The Drucker-Prager Failure Criterion

"The Drucker-Prager criterion, formulated in 1952, is a simple modification of the Von Mises criterion." In this criterion, "...the influence of a hydrostatic stress component on failure is introduced by inclusion of an additional term in the Von Mises expression." (Chen and Han 1988, 94).

In Reference 5 it is stated that the Drucker-Prager option "is applicable to granular (frictional) material such as soils, rock, and concrete and uses the outer cone approximation of the Mohr-Coulomb law." The text, in outlining how the Drucker-Prager option is input to obtain a yield solution, went on to say that "the input consists of only three constants: The cohesion value (which must be > 0), the angle of internal friction, and the dilatancy angle. The amount of dilatancy (the increase in material volume due to yielding) can be controlled with the dilatancy angle. If the dilatancy angle is equal to the friction angle, the flow rule is associative. If the dilatancy angle is zero (or less than the frictional angle), there is no (or less of an) increase in material volume when yielding and the flow is non-associative" (Reference 5, 2-16).

The Drucker-Prager criterion is defined as[4]

$$f(I_1, J_2) = \alpha I_1 + \sqrt{J_2} - k = 0 \tag{6.98}$$

and using variables ξ and ρ leads to

$$f(\xi, \rho) = \sqrt{6}\alpha\xi + \rho - \sqrt{2}k = 0 \qquad (6.99)$$

where α is a material constant and k is the material yield parameter. When $\alpha = 0$, Equation (6.99) becomes the Von Mises criterion[4].

As shown in Chen, the surface of failure in Equation (6.99) when plotted in principal stress space is a right circular cone. Figure 6.12 plots the Drucker-Prager criterion in principal stress space and shows its meridian and cross section on the π-plane.

Chen and Han 1988, 94, went on to say in that "The Mohr-Coulomb hexagonal failure surface is mathematically convenient only in problems where it is obvious which one of the six sides is to be used. If this information is not known in advance, the corners of the hexagon can cause considerable difficulty and give rise to complications in obtaining a numerical solution. The Drucker-Prager criterion as a smooth approximation to the Mohr-Coulomb criterion, can be made to match the latter by adjusting the size of the cone. For example, if the Drucker-Prager circle is made to agree with the outer apices of the Mohr-Coulomb hexagon, i.e. the two surfaces are made to coincide along the compression meridian ρ_c where $\theta = 60°$, then the constants α and k in Equation" (6.98) "are related to the constants c and ϕ in" Equation (6.50). We therefore get:

$$\alpha = \frac{2\sin\phi}{\sqrt{3}(3 - \sin\phi)}, \qquad k = \frac{6c\cos\phi}{\sqrt{3}(3 - \sin\phi)} \qquad (6.100)$$

The Drucker-Prager cone that corresponds to the constants in Equation (6.100) will circumscribe the Mohr-Coulomb hexagonal pyramid as its smooth approximation, and represents an outer bound of the Mohr-Coulomb failure surface in stress space.

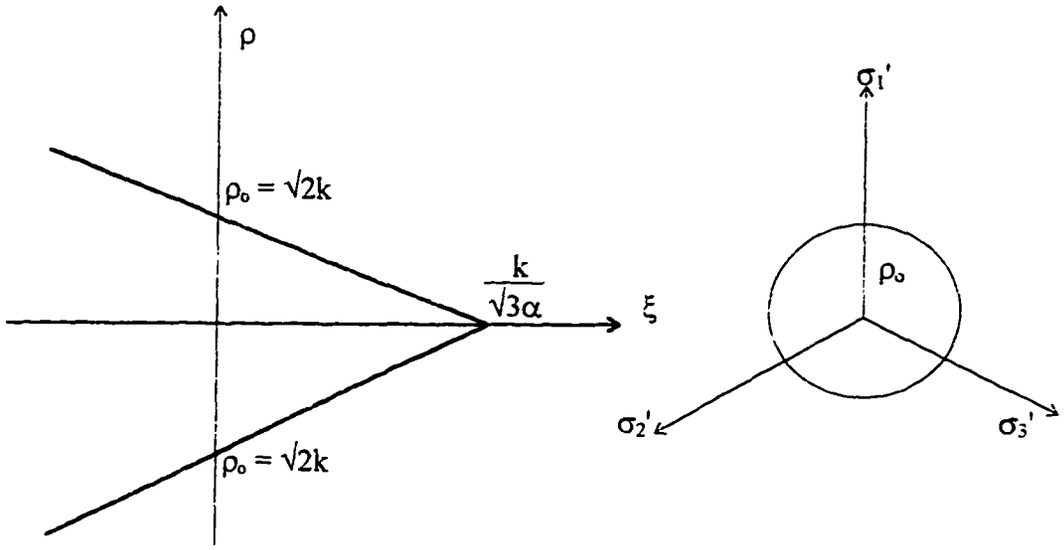

(a) Meridian Plane $\theta = 0$ (b) π–Plane

Figure 6.12

Graphical representation of Drucker-Prager criterion in principal stress space[4].

The Drucker-Prager material behavior option uses the Drucker-Prager yield criterion with either an associative or non associative flow rule as explained above . With this option "...the yield surface does not change with progressive yielding, hence there is no hardening rule and the material is elastic-perfectly plastic." See Figure 6.7.

From the ANSYS User's Manual, Volume IV, Theory, 4-18 & 19, the following has been extracted. To use the symbols employed in the ANSYS manual let us change the symbols in Equation (6.100) as follows.

Let $\alpha = \beta$ and $k = \sigma_p$, so we get:

$$\beta = \frac{2 \sin \phi}{\sqrt{3}(3 - \sin \phi)}, \qquad \sigma_p = \frac{6c \cos \phi}{\sqrt{3}(3 - \sin \phi)} \tag{6.101}$$

In developing the Drucker-Prager yield criterion, remember that from Equation (6.98) that

$$f(I_1, J_2) = \alpha I_1 + \sqrt{J_2} - k = 0 \tag{6.102}$$

If we substitute the relationships from Equation (6.58),

$$3\sigma_m = 3\{1/3(\sigma_1 + \sigma_2 + \sigma_3)\} = I_1 \quad (6.103)$$

and from Chen and Han 1988, 58,

$$J_2 = {}^1/_2 s_{ij}s_{ji} \quad (6.104)$$

$$= {}^1/_2\{s\}\{s\}^T$$

We can take these relationships and state that the equivalent stress for the Drucker-Prager yield criterion is:

$$\sigma_e = 3\beta\sigma_m + [1/2\{s\}\{s\}^T]^{1/2} \quad (6.105)$$

where: $\sigma_m = 1/3(\sigma_x + \sigma_y + \sigma_z)$

the mean or hydrostatic stress from Equation (6.58).

$\{s\}$ = the deviatoric stress

$= \{\sigma\} - \sigma_m[1 \quad 1 \quad 1 \quad 0 \quad 0 \quad 0]^T$

(Reference 6, 4-12)

β = material constant [α in Equation (6.102)]

ϕ = the angle of internal friction

The material yield parameter is defined as:

$$\sigma_p = \frac{6c\cos\phi}{\sqrt{3}(3 - \sin\phi)} \quad (6.106)$$

From Equation (6.100) represented by *k*

where c = the input cohesion angle

The yield criterion is therefore defined as:

$$F_y = \sigma_e - \sigma_p = 0 \text{ [from Equation (6.46)]}$$

$$= 3\beta\sigma_m + [1/2\{s\}\{s\}^T]^{1/2} - \sigma_p = 0 \qquad (6.107)$$

$\{\partial F_y/\partial\sigma\}$ is readily computed from (6.107) as:

$$\{\partial F_y/\partial\sigma\} = \beta[1 \quad 1 \quad 1 \quad 0 \quad 0 \quad 0]^T + \frac{1}{[1/2\{s\}\{s\}^T]^{1/2}}\{s\} \qquad (6.108)$$

$\{\partial Q/\partial\sigma\}$ to be treated later is similar to $\{\partial F_y/\partial\sigma\}$.

The material constant β is evaluated using ϕ_f (the "dilatancy" constant). When $\phi_f = \phi$, (as used in this analysis) the flow rule is associative and plastic straining occurs normal to the yield surface, resulting in material heave or swell, and irreversible plastic strains[6]. The Drucker-Prager yield surface is a circular cone as shown in Figure 6.13. (See References 4 & 6).

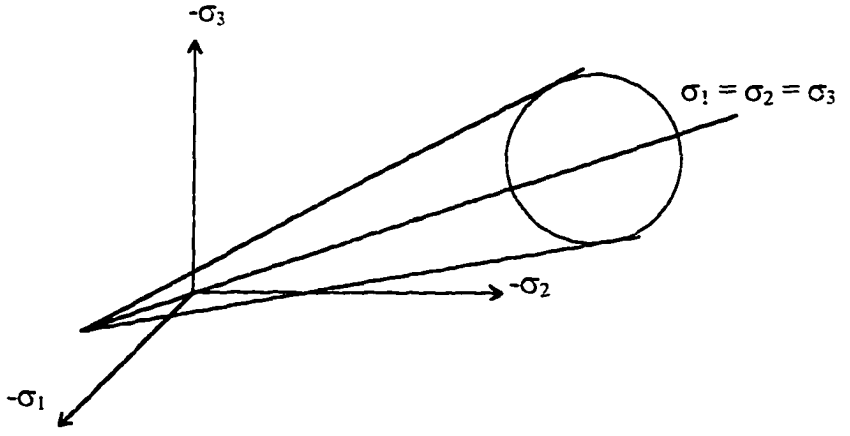

Figure 6.13

Yield Surface for the Drucker-Prager Option[6]

The yield surface for the yield criterion used by the ANSYS Solid 45 model and used in this research is the Drucker-Prager yield surface. This surface uses material parameters from Equation (6.99) chosen such that they correspond to the outer apices of the hexagonal Mohr-Coulomb yield surface[6]. (See Figure 6.14 reproduced from the text[6]). This figure shows the Drucker-Prager yield surface touching all of the apices of

the Mohr-Coulomb yield surface. It should be noted that this theoretical approach used by the ANSYS application is a modification to the theory in Reference 4 and does not follow the diagram shown in Chen, p96, in which the Drucker-Prager yield surface touches only the apices of the compressive meridians where $\theta = 60°$.

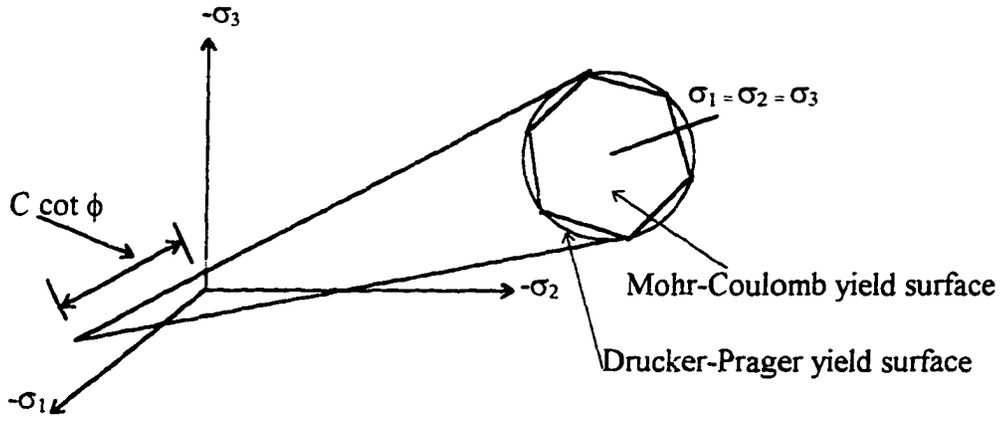

Figure 6.14

The Drucker-Prager and Mohr-Coulomb Yield Surfaces matched at the compression and tension meridians as used in the ANSYS analysis[6].

The Plastic Flow Rule

"The flow rule used in the ANSYS application employed in this research, determines the direction of plastic straining, and is given as:

$$\{d\varepsilon^{Pl}\} = \lambda\{dQ/d\sigma\} \qquad (6.109)$$

where: λ = plastic multiplier (which determines the amount of plastic straining. See Equation 6.118)

Q = function of stress termed the plastic potential (which determines the direction of plastic straining)

If Q is the yield function (as is normally assumed), the flow rule is termed associative and the plastic strains occur in a direction normal to the yield surface." (ANSYS User's Manual, Volume IV, Theory, p4-8)

In terms of the plastic strain increment we have seen before that if the equivalent stress exceeds the yield stress, permanent deformation will occur in the material. If we ignore work hardening and kinematic hardening (not considered in the Drucker-Prager option), we can modify Equation (4 1-4) in Reference 6

$$F_y(\{\sigma\}, \quad \chi, \quad \{\alpha\}) = 0 \tag{6.110}$$

where

$F_y(\{\sigma\}$ = σ_p, the yield parameter

χ = plastic work

$\{\alpha\}$ = translation of the yield surface

and get:

$$F_y(\{\sigma\}) = 0 \tag{6.111}$$

Differentiating Equation (6.111) we get

$$dF_y = \{\partial F_y/\partial\sigma\}^T \{d\sigma\} = 0 \tag{6.112}$$

where from Equation (6.34):

$$\{d\sigma\} = [C]_\varepsilon \{d\varepsilon^{el}\} \tag{6.113}$$

and [C] is the elastic constitutive matrix[2]:

We also have $\{d\varepsilon^{el}\} = \{d\varepsilon\} - \{d\varepsilon^{pl}\}$ (6.114)

where: $\{d\varepsilon\}$ = Total strain

$\{d\varepsilon^{el}\}$ = Elastic strain

$$\{d\varepsilon^{pl}\} = \text{Plastic strain}$$

Note, that the total strain increment is made up of the elastic strain plus the plastic strain.

From Equation (6.109) we have:

$$\{d\varepsilon^{pl}\} = \lambda\{dQ/d\sigma\}$$

From Equation (6.34) we know that

$$\{\sigma\} = [C]\{\varepsilon\}$$

so as shown in the text[6]

$$\{d\sigma\} = [C]\{d\varepsilon^{el}\} \qquad (6.115)$$

Taking Equation (6.112)

$$\{\partial F_y/\partial\sigma\}^T\{d\sigma\} = 0$$

we get

$$\{\partial F_y/\partial\sigma\}^T[C]_\varepsilon\{d\varepsilon^{el}\} = 0 \qquad (6.116)$$

substituting Equations (6.109) and (6.114) into Equation (6.116), we get

$$\{\partial F_y/\partial\sigma\}^T[C]_\varepsilon\{d\varepsilon\} - \{\partial F_y/\partial\sigma\}^T[C]_\varepsilon\lambda\{dQ/d\sigma\} = 0 \qquad (6.117)$$

Reducing Equation (4.1-13) in Reference 6, the resulting plastic multiplier for the Drucker-Prager option becomes

$$\lambda = \{d\varepsilon\}\{d\sigma/dQ\} \qquad (6.118)$$

Reviewing Equation (6.109) and looking at the relationship in Equation (6.118) it shows that the size of the plastic strain increment is related to the total strain increment for the Drucker-Prager option.

Finite Element Formulation

"The general governing equations of the finite element method for a static analysis can be derived from the principle of virtual work. (Chen and Han 1988, 161-163, 296-299).

$$\int_V \sigma_{ij}\,\delta\varepsilon_{ij}\,dV = \int_A T_i\,\delta u_i\,dA + \int_V q_i\,\delta u_i\,dV \qquad (6.119)$$

"where δu_i and $\delta\varepsilon_{ij}$ are virtual displacement increments and virtual strain increments, respectively, and they form a compatible set of deformations; T_i and q_i are surface traction and body force, respectively; and σ_{ij} with T_i and q_i form an equilibrium set."[4] In matrix form Equation (6.119) becomes

$$\int_V \{\delta\varepsilon\}^T\{\sigma\}\,dV = \int_A \{\delta u\}^T\{T\}\,dA + \int_V \{\delta u\}^T\{q\}\,dV \qquad (6.120)$$

where $\{u\}$ is the displacement vector and $\{\varepsilon\}$ is the strain vector and $\{\sigma\}$ can be represented as the equivalent stress. These are defined in the relationships of Equations (6.33) and (6.36) and can be defined here again as follows:

$$\{u\}^T = \{u, v, w\}, \qquad \{\delta u\}^T = \{\delta u, \delta v, \delta w\} \qquad (6.121)$$

$$\{\varepsilon\}^T = \{\varepsilon_x, \varepsilon_y, \varepsilon_z, \gamma_{yz}, \gamma_{zx}, \gamma_{xy}\} \qquad (6.122)$$

$$\{\delta\varepsilon\}^T = \{\delta\varepsilon_x, \delta\varepsilon_y, \delta\varepsilon_z, \delta\gamma_{yz}, \delta\gamma_{zx}, \delta\gamma_{xy}\} \qquad (6.123)$$

$$\{\sigma\}^T = \{\sigma_x, \sigma_y, \sigma_z, \tau_{yz}, \tau_{zx}, \tau_{xy}\} \qquad (6.124)$$

From Chen and Han 1988, 297 "...for a geometrically linear analysis, or a small-deformation analysis, we have":

$$\{\varepsilon\} = [B]\{U\}, \qquad \{\delta\varepsilon\} = [B]\{\delta U\} \qquad (6.125)$$

where Chen continues by saying that displacement $\{U\}$ is the displacement vector of the nodal points that is related to the distributed displacement $\{u\}$ by

$$\{u\} = [N]\{U\} \tag{6.126}$$

where [N] is called the matrix of the *shape function* or *the displacement interpolation function*. "The N_i's express the shape of the assumed displacement function over the domain of the element when the i^{th} degree of freedom has unit value and all other degrees of freedom are zero." (Logan 1986, 28).

Let us pause a while to examine the shape function used in Equation (6.126). In the isoparametric formulation of a 3-dimensional element let us look at the basic (linear) hexahedral eight-node element with isoparametric coordinates *s*, *t* and *z'* as shown in Figure 6.15 below. The faces of the element are now defined as s, t, z' = ± 1.

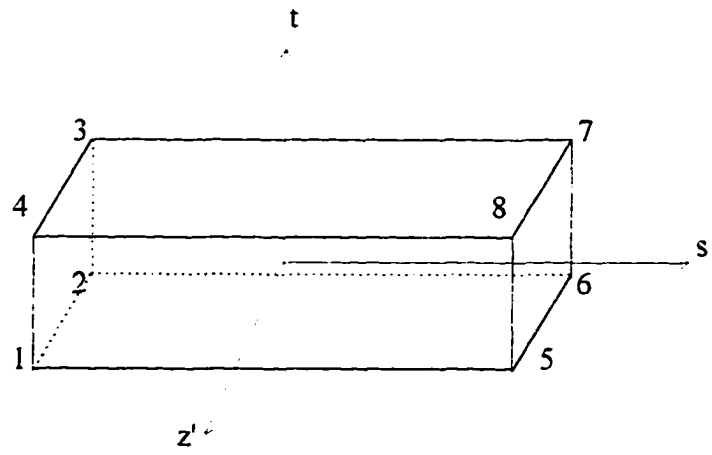

Figure 6.15

Linear hexahedral element[1].

Expanding the shape function matrix for the 4-node Tetrahedron (Logan, p377), to that of the 8-node hexahedron, we get:

$$\begin{Bmatrix} u \\ v \\ w \end{Bmatrix} = \begin{bmatrix} N_1 & 0 & 0 & N_2 & 0 & 0 & N_3 & 0 & 0 & N_4 & 0 & 0 & \cdots \\ 0 & N_1 & 0 & 0 & N_2 & 0 & 0 & N_3 & 0 & 0 & N_4 & 0 & \cdots \\ 0 & 0 & N_1 & 0 & 0 & N_2 & 0 & 0 & N_3 & 0 & 0 & N_4 & \cdots \end{bmatrix} \begin{Bmatrix} u_1 \\ v_1 \\ w_1 \\ . \\ . \\ . \\ u_8 \\ v_8 \\ w_8 \end{Bmatrix} \quad (6.127)$$

where:

u, v and w are displacements parallel to the global coordinates X, Y and Z, respectively.

and shape functions are defined as;

$$N_i = \frac{(1 + ss_i)(1 + tt_i)(1 + z'z'_i)}{8} \quad (6.128)$$

with s_i, t_i, $z_i = \pm 1$ and $i = 1, 2, \ldots, 8$. Thus

$$N_1 = \frac{(1 + ss_1)(1 + tt_1)(1 + z'z'_1)}{8} \quad (6.129)$$

and for $s_i = -1$, $t_i = -1$, and $z_i = +1$, and substituting in Equation (6.128) we get

$$N_1 = \frac{(1 - s)(1 - t)(1 + z')}{8} \quad (6.130)$$

The text can be consulted for the remaining N_i relationships.

The text show the relationship of the isoparametric axes to the global X, Y and Z axes and we get the global displacements within the element as given by Equation (6.127) in the form[1]:

$$\begin{Bmatrix} X \\ Y \\ Z \end{Bmatrix} = \sum_{i=1}^{8} \begin{bmatrix} N_i & 0 & 0 \\ 0 & N_i & 0 \\ 0 & 0 & N_i \end{bmatrix} \begin{Bmatrix} X_i \\ Y_i \\ Z_i \end{Bmatrix} \quad (6.131)$$

Now continuing from Equation (6.126) in which the displacement vector relationship is shown as

$$\{u\} = [N]\{U\} \tag{6.132}$$

where:

$\{U\}$ is the displacement vector

$[N]$ is the matrix of the displacement interpolation function, or the shape function and the strain-displacement matrix $[B]$ in Equation (6.125) is defined as

$$[B] = [L][N] \tag{6.133}$$

and $[L]$ is the differential operator matrix as shown in Equation (6.33)

$$[L] = \begin{bmatrix} \frac{\partial}{\partial x} & 0 & 0 \\ 0 & \frac{\partial}{\partial y} & 0 \\ 0 & 0 & \frac{\partial}{\partial z} \\ \frac{\partial}{\partial y} & \frac{\partial}{\partial x} & 0 \\ 0 & \frac{\partial}{\partial z} & \frac{\partial}{\partial y} \\ \frac{\partial}{\partial z} & 0 & \frac{\partial}{\partial x} \end{bmatrix} \tag{6.134}$$

Rewriting Equation (6.33) we have

$$\{\varepsilon\} = [L]\{u\} \tag{6.135}$$

As shown in Chen and Han 1988, 298, if we substitute Equations (6.125) and (6.126) in Equation (6.120) we get the main equation for a small deformation analysis

$$\int_V \{B\}^T \{\sigma\}\, dV = \int_A \{N\}^T \{T\}\, dA + \int_V \{N\}^T \{q\}\, dV \quad (6.136)$$

or

$$\int_V \{B\}^T \{\sigma\}\, dV = \{R\} \quad (6.137)$$

where {R} is the equivalent external force acting on the nodal points. This equation is referred to as the Newton-Raphson restoring force in Reference 5, 3-8).

In a linear stress strain relationship the main equation for a linear analysis is defined as

$$[K][U] = \{R\} \quad (6.138)$$

where [K] is the stiffness matrix of the structure or model in the case of this research, which can be expressed as[4.6]

$$[K] = \int_V [B]^T [C] [B]\, dV \quad (6.139)$$

where [C] is the elastic constitutive matrix for an isotropic material from Equation (6.34).

The reader wishing more information into the theory of finite element methods and plasticity theory can refer to the ANSYS manuals and the text in the references at the end of this chapter. Reference 6, 4-11 & 12 outlines the implementation procedure for the operations of the ANSYS finite element program.

REFERENCES

[1] Logan, D. L., A First Course in the Finite Element Method. Rose-Hulman Institute of Technology, 1986.

[2] Grandlin, H, Jr., Fundamentals of the Finite Element Method, 1986, 1991.

[3] Prager, W and Hodge, P. G. Jr., Theory of Perfectly Plastic Solids, 1951, 1968.

[4] Chen, W. F. and Han, D. J., Plasticity for Structural Engineers, 1988.

[5] ANSYS - Engineering Analysis System, Revision 5.0A User's Manual, Vol. III Elements, 1991.

[6] ANSYS - Engineering Analysis System, Revision 5.0A User's Manual, Vol. IV Theory, 1991.

CHAPTER VII

THE MODEL

In order to pursue the theoretical studies in this research effort, 3-D finite element analyses were conducted on small utility cuts of size 3 ft x 3 ft, for unsupported depths up to 5 feet. The general range of depths for utility excavations in city street pavements is from 3 feet to 5 feet. (US Occupational Safety and Health Administration regulations dated 1974 states that the maximum unsupported depth of excavations should be 5 feet).

Pavement Components

The following pavement structural components were considered in the analyses conducted in this research effort:

1. An asphaltic concrete surface thickness of 4 ins.
2. A granular base thickness of 8 ins.
3. A granular fill/subgrade thickness of 8 feet (divided into 6 inches layers). This depth was used to determine the extent of the excavation impacts in the soil mass around and below the cut.

Model Selection for Analysis

Because of the symmetry of the square utility cut, the model was designed to conduct an axi-symmetric analysis on a 1/8 section of the soil surrounding the cut, assuming homogeneous and isotropic conditions in the soil. (See Figure 7.1). The typical 1/8 section was determined to be adequately representative of the remaining seven 1/8

sections that surround the cut, in determining the failure characteristics that exist in the pavement structure in the vicinity of small utility cuts.

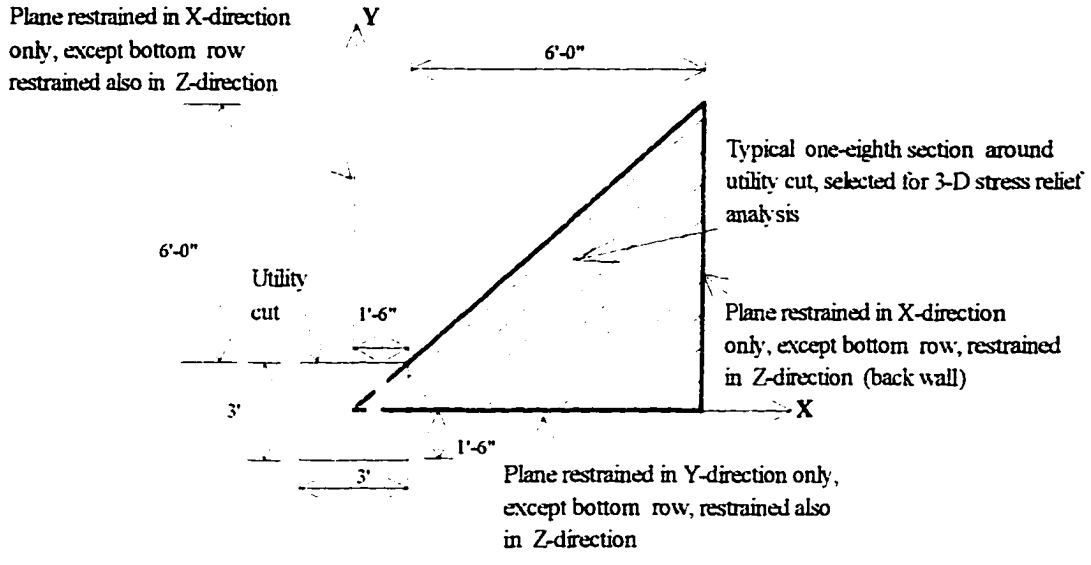

Figure 7.1.
Plan View of Small Utility Cut Site and Typical 1/8 Section Used in Stress Relief Analysis.

The theory and assumptions supporting the required width of models for the respective depths are included in Chapter IV of this dissertation. Table 4.4 shows the model widths (rounded to the nearest 0.5 feet) required for individual analysis of the respective cut depths. However, for this analysis, the width of the model was established at 6 inches greater than required for the 5 feet deep analysis, in order to measure the pavement performance, up to and beyond the computed zone of influence for this cut depth in table 4.4.

Material Selection

In making the most generic selection of materials for this theoretical research, it was decided to use the material types and properties taken from the text, which most generally fit within the types of materials used in road construction. (Yoder and Witczak

1975, 236-7, and Lambe and Whitman 1969, 149). For the base, a well graded gravel or sandy gravel was used, and for the fill/subgrade, a well graded sand or gravely sand was used. (See Table 7.1). (The research assumed, that in these materials, there is some intrinsic cohesion value, discussed in previous chapters).

Table 7.1

Material properties used in the utility cut analysis (From Lambe and Whitman 1969)

			FRICTION ANGLE $\phi(°)$			
			Slope Angle of Repose	At Ultimate Strength	At Peak Strength	
Location	**Material**	**Density (pcf)**	**(Vertical to Horizontal)**		**Medium Dense**	**Dense**
Fill	Well Graded Sand or gravely sand	110-130	30-34	30-34	34-40	38-46
Base	Gravel or sandy gravel, well graded.	125-140	32-36	32-36	36-42	40-48

During the research process utility cuts were examined using three density combinations found in the selected pavement materials. (Yoder and Witczak 1975, 236-237). Table 7.2 below shows the density combinations used, which covered the density range of the respective materials.

Table 7.2

Density combinations for the materials used in the utility cut research

Location	Material	Density (lb/ft^2)		
		Combination #1	Combination #2	Combination #3
Fill	Well Graded Sand	110	120	130
Base	Sand and Gravel	125	133	140

Three combinations of angles of internal friction (ϕ-angles) were selected between loose and medium dense/dense range, that were pertinent to the respective materials selected. (See Table 7.1 above). Table 7.3 shows the angles of internal friction (ϕ angles) used in the analyses of the pavement materials. (Lambe and Whitman 1969, 149).

Table 7.3

Angle of internal friction test scenarios

		Angle of Internal Friction Scenarios		
		#1	#2	#3
Location	Material	ϕ	ϕ	ϕ
Base	Gravel or Sandy Gravel, Well Graded	32	36	40
Fill	Well Graded Sand or Gravely sand	30	34	38

By comparison, Harris and O'Rourke 1983, reported that they studied two soil types, (loose and medium dense/dense sand in their pipeline trench study). The soils they analyzed were typical of the soils used for bedding and backfilling around utility pipes in urban areas. The loose sand had moist density characteristics of 115 lb/ft^3 and an angle of internal friction of 32°. The medium dense/dense sand was modeled as having a moist density of 137 lb/ ft^3 and an angle of internal friction of 40°.

Description of the model

The models used in the utility cut research covers the 1/8 area, shown in the plan view in Figure 7.1. The height of the main model is 9 feet. The model was designed to allow a step analysis that would simulate the excavation process of a utility cut for depths up to 5 feet.

In the respective models, the nodal locations from the edge of the cut were marked off in 0.5 foot intervals, except the last column of elements, which is 1 foot wide. (See Figures 7 (a) and (b) and Figure 7.3(a)). The granular fill/subgrade material was laid out in 6 in. layers. The analyses used an 8 in. thick base and a 4 in. thick asphalt surface.

Composition of the three-dimensional Models

Earlier work in this effort had analyzed three density combinations, with three ϕ scenarios in each density combination. Similarities in the impacts of the utility cuts over the three density combinations for depths 3 feet and $3^1/_2$ feet, resulted in the analysis being mainly confined to density combination 2 (γ_{BASE} = 133 lb/ft^2 and $\gamma_{SUBBASE}$ = 120 lb/ft^2).

In conducting earlier analyses sensitivity tests were done to determine the minimum cohesion value required to maintain stability of the cut for depths, 3 to 5 feet. Twenty-seven worst case models were tested to conduct this sensitivity analysis. The worst case model assumed that the model was free to slide on a plane, located at the floor elevation of the utility cut and that no resisting force acted on the soil mass from below the plane of the cut floor. In addition, the worst case models analyzed the soil around the cut after the excavation was completed. Geostatic forces were applied to the back-wall nodes of the worst case model, to push the soil mass towards the open cut.

The analysis determined that the minimum cohesion value required for the Density Combination 2, ϕ Scenario #2 material (the material used in this analysis) at depth 5 feet was 0.325 lb/in^2. This cohesion value was later applied in the Time Step analysis, to aid the application of the Drucker-Prager failure criterion needed for granular material analysis.

ANSYS Solid 45 version 5.2, 1995 was used to analyze the three-dimensional FEM model, created to simulate the graduated excavation process. The model was created with 2040 nodes and 1680 elements. The 4 inches asphalt surface has elements 6"x6"x4". The 8 inches granular base has elements 6"x6"x8". The 8 feet thick fill/subgrade is divided into 6 inches layers for the first 6 feet depth, with elements 6"x6"x6". The lower 2 feet of the fill/subgrade material is divided into 12 inches layers with element sizes 6"x6"x12". The exception to these element sizes are found along the diagonal side of the model, where prism shaped elements, with 6 inches perpendicular sides are used. The model in this analysis is 7'-6" wide, commencing at the centerline of the 3' x 3' utility cut, with an 18" cut area and a 6 feet wide soil mass behind the face of the utility cut. The model represents a 9 feet depth of soil mass.

The inputs to the model included the modulus of elasticity, density, Poisson's ratio the Drucker-Prager constants (the cohesion value, the angle of internal friction and the dilatancy angle), and gravity loading. See Table A.1 in the Appendix.

The model used in this analysis tested a 1/8 section of the soil mass surrounding the utility cut, assuming symmetry and constant material properties around the square utility cut. Figure 7.2 shows a plan view and front elevation of the uncut soil model

showing the node numbers assigned to the model. Figure 7.3 shows the 10 excavation models used in the Time Step analysis. In the Time Step 1 analysis, the model was restrained with a zero displacement in the X-direction on the vertical plane that is bounded by node # 15 through node #295. The vertical plane bounded by node #1 to node #15 was restrained with a zero displacement in the Y-direction, and the vertical diagonal plane bounded by node #1 through node #295 was restrained with a zero displacement in the Y-direction, perpendicular to that plane. All nodes at the bottom of the model were restrained with a zero displacement in the Z-direction. See Figure 7.2(c).

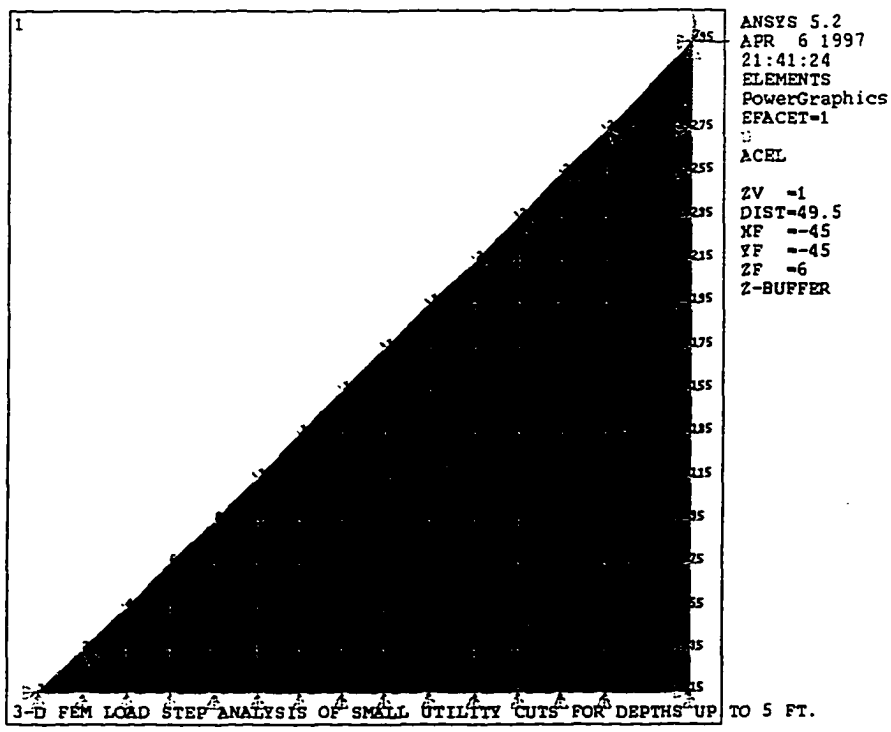

Figure 7.2(a)

Plan View of the Finite Element Model for Analysis of the Soil in the Vicinity of the Utility Cut

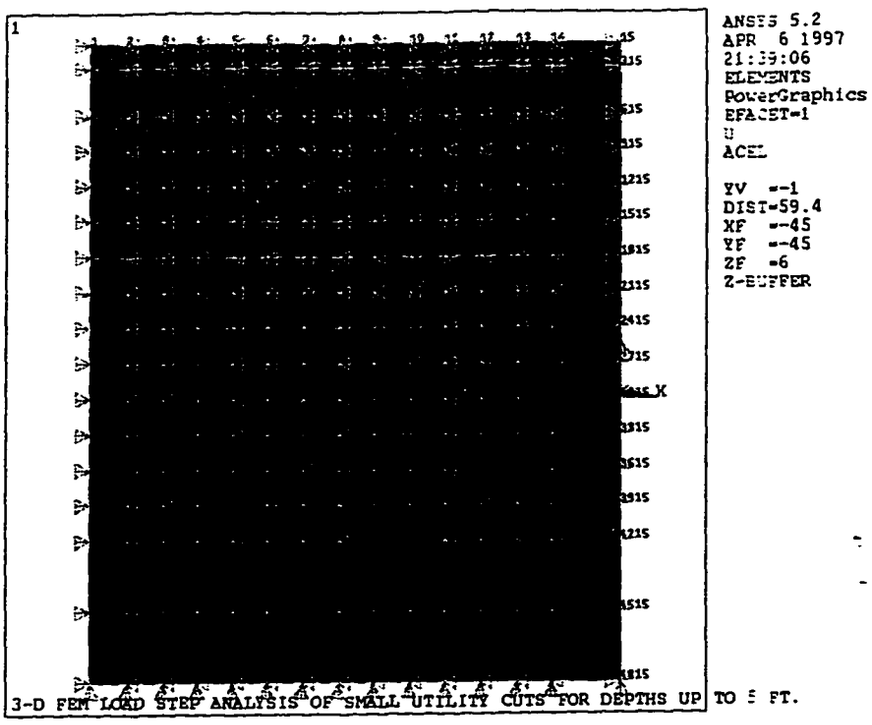

Figure 7.2(b)
Elevation of the Finite Element Model for Analysis of the Soil in the Vicinity of the Utility Cut

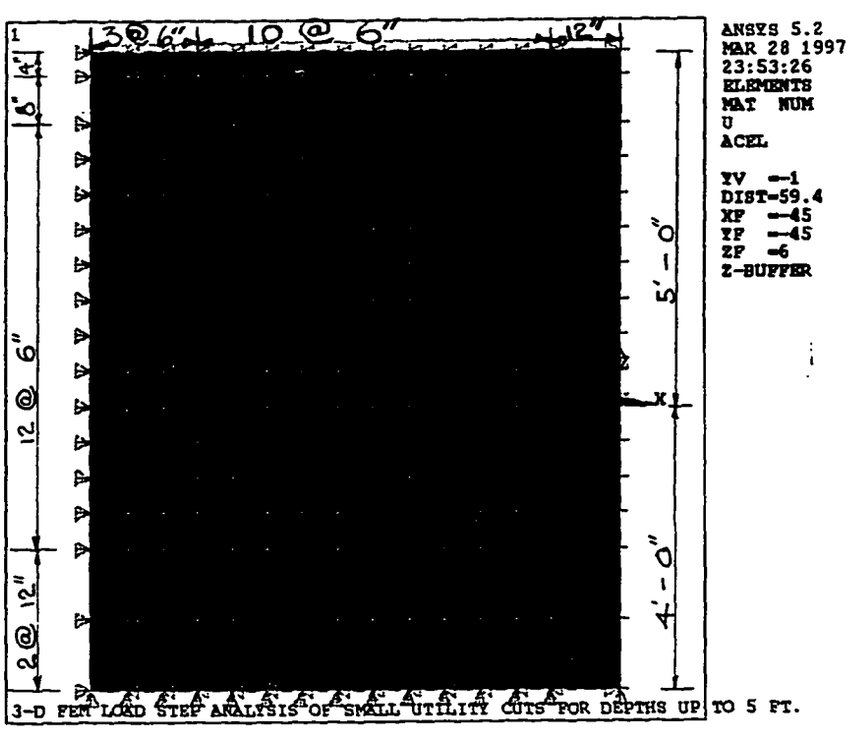

Figure 7.2(c)
Elevation of the Finite Element Model Used in the Time Step 1 Analysis of the Utility Cut

Figures 7.3(a) to 7.3(j) show the composition of the models used in the load step analysis for the excavation process, commencing with Time Step 2 (depth 0.33 feet) and ending with Time Step 11 (depth 5 feet).

Based on the assumption that beyond a distance of 6 feet from the face of the utility cut, the excavation will have little or no influence on the soil mass., from Time Step 2, and for the remainder of the Time Step analyses, the vertical plane of nodes bounded by node #15 through node #295, (see Figures 7.2(a) and 7.2b)) received a Z-direction constraint, with the respective layer displacement values obtained from the results of the Time Step 1 analysis. The nodes were also restrained in the Y-direction to ensure complete fixity of the displaced model from Time Step 1. (See Figures 7.3(b) to 7.3(k)).

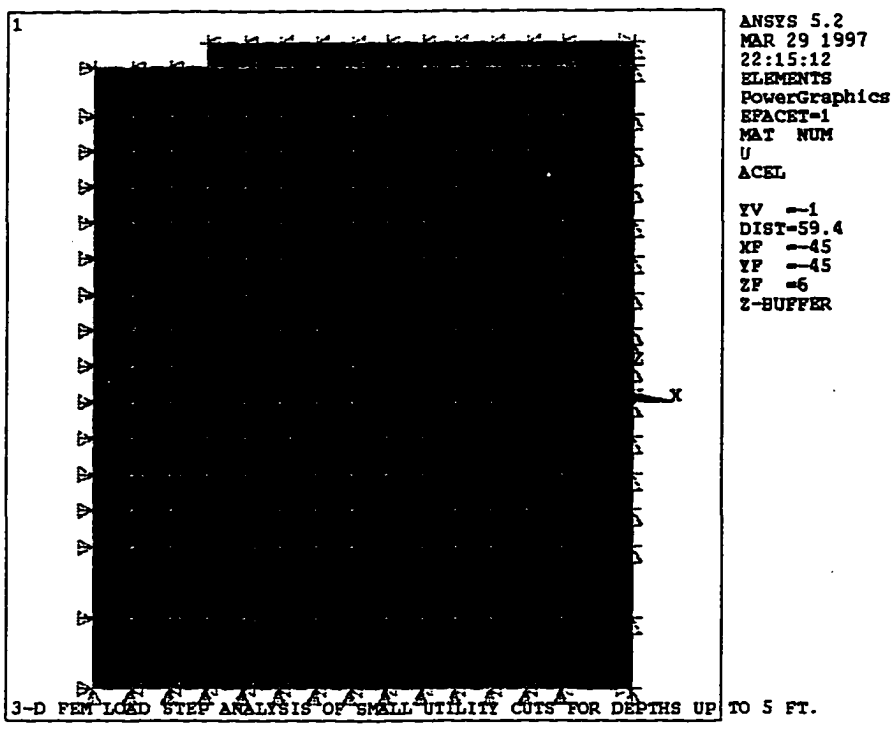

Figure 7.3(a)

Elevation of the Finite Element Model Used in Time Step 2. Cut Excavation 0.33 ft. Deep.

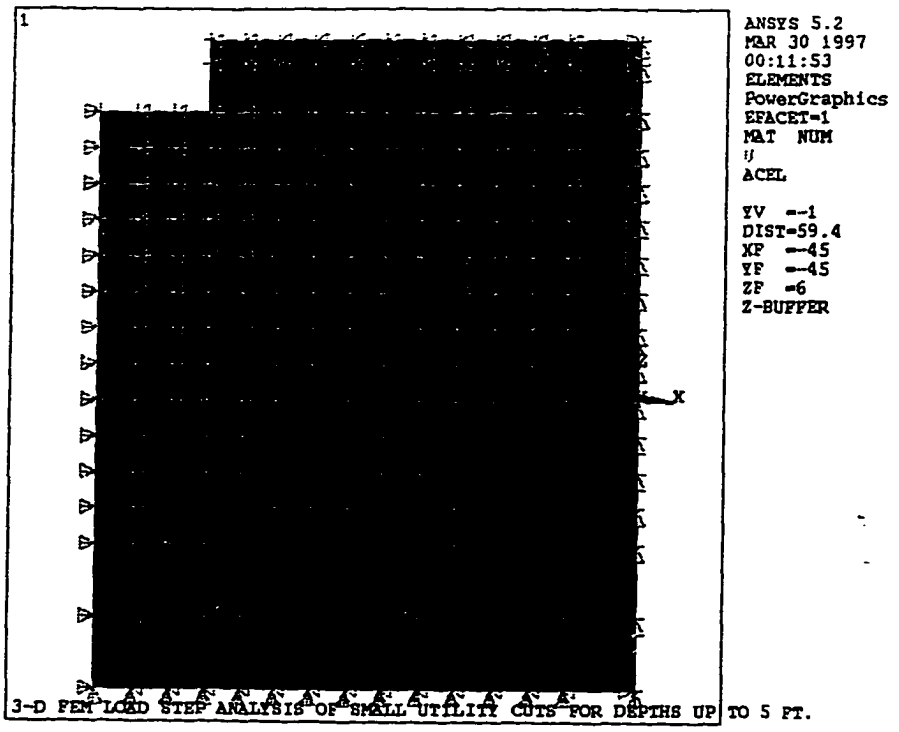

Figure 7.3(b)

Elevation of the Finite Element Model used in Time Step 3. Cut Excavation 1 ft. Deep.

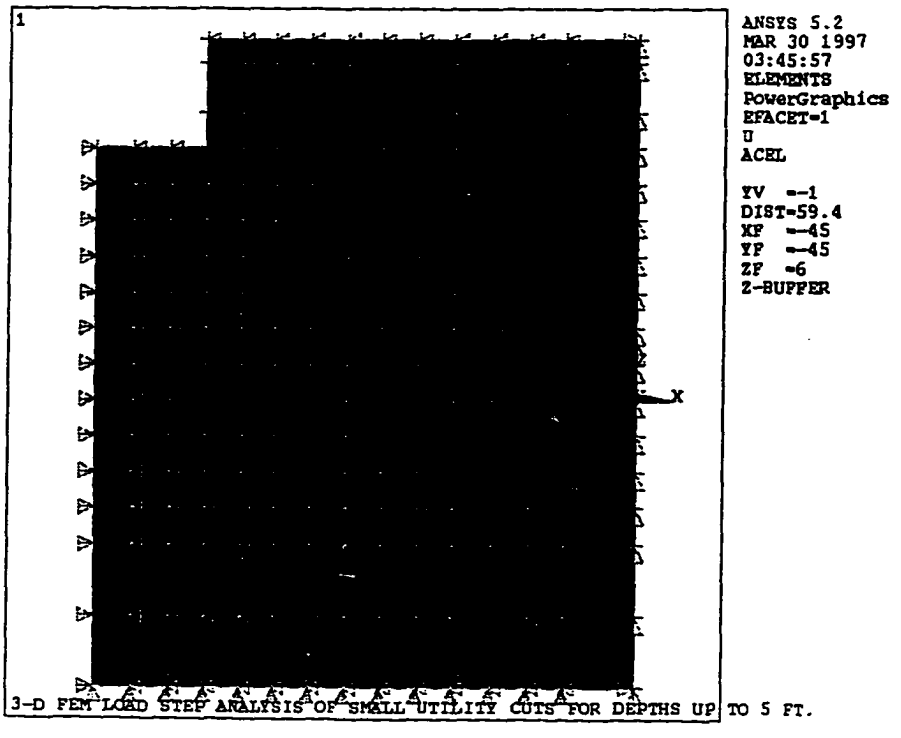

Figure 7.3(c)

Elevation of the Finite Element Model used in Time Step 4. Cut Excavation 1.5 ft. Deep.

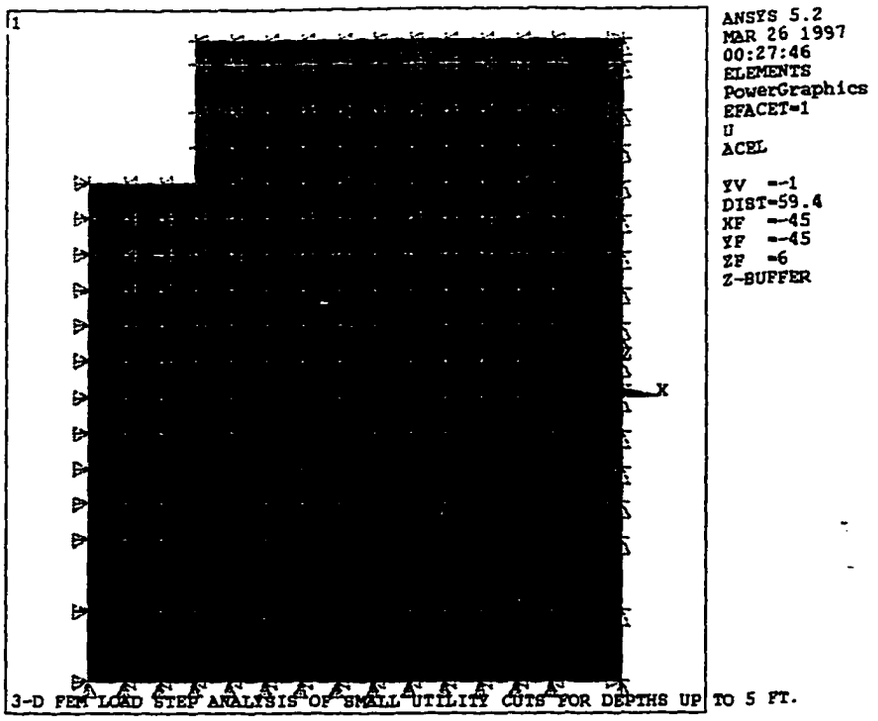

Figure 7.3(d)
Elevation of the Finite Element Model used in Time Step 5. Cut Excavation 2 ft. Deep.

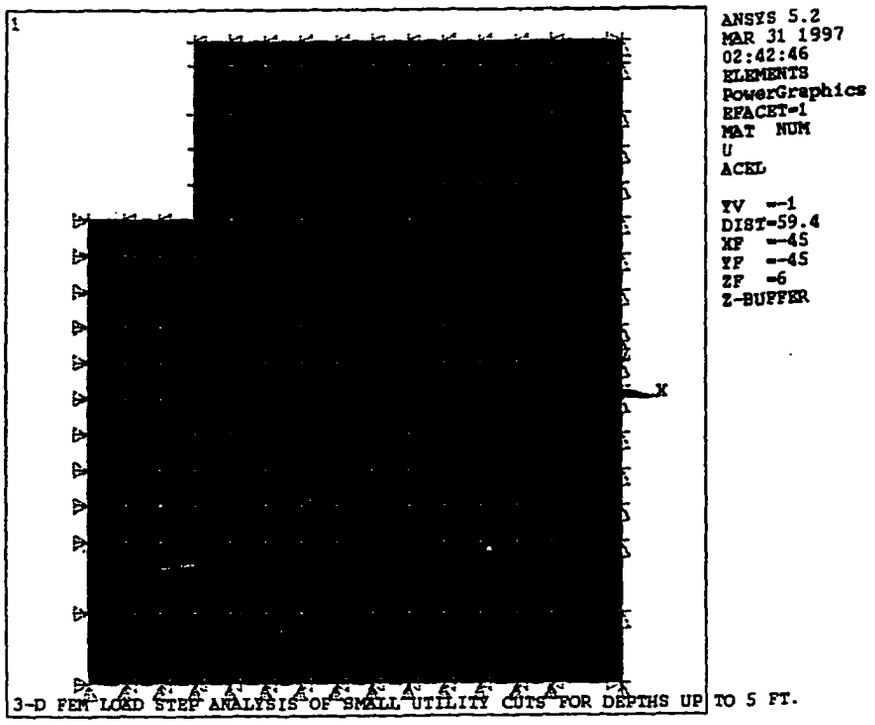

Figure 7.3(e)
Elevation of the Finite Element Model used in Time Step 6. Cut Excavation 2.5 ft. Deep.

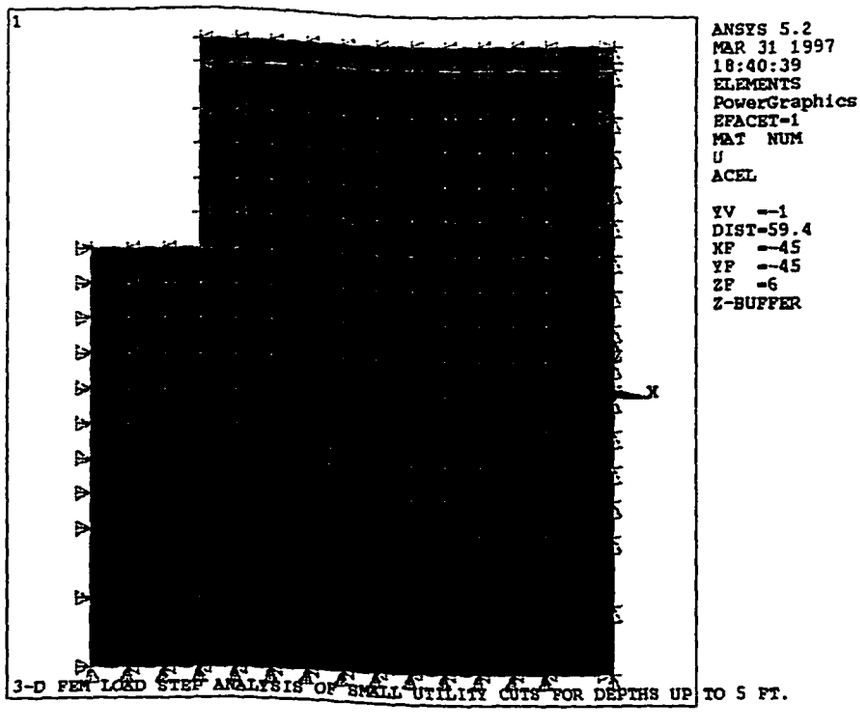

Figure 7.3(f)
Elevation of the Finite Element Model used in Time Step 7. Cut Excavation 3 ft. Deep.

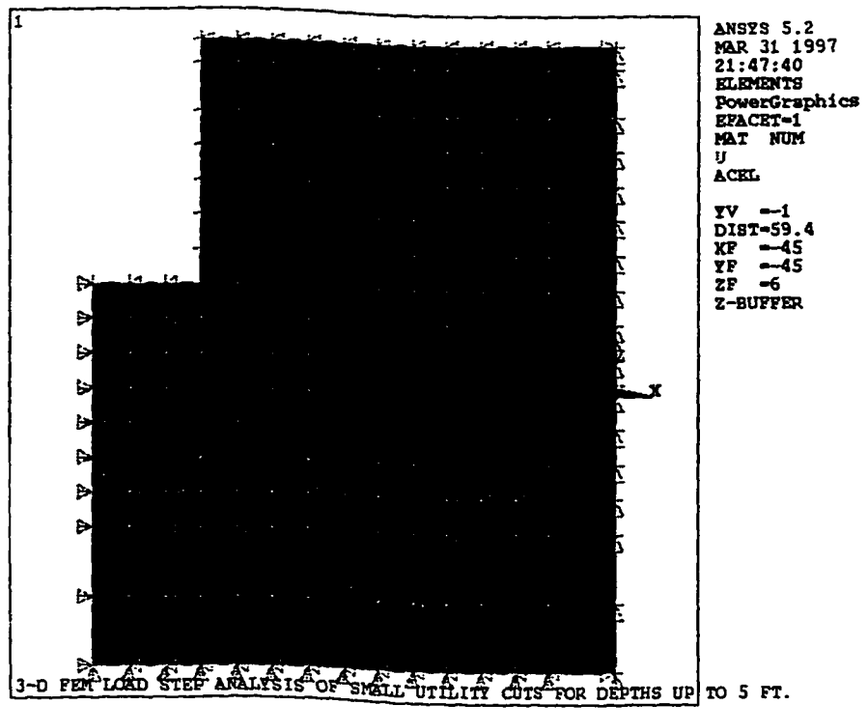

Figure 7.3(g)
Elevation of the Finite Element Model used in Time Step 8. Cut Excavation 3.5 ft. Deep.

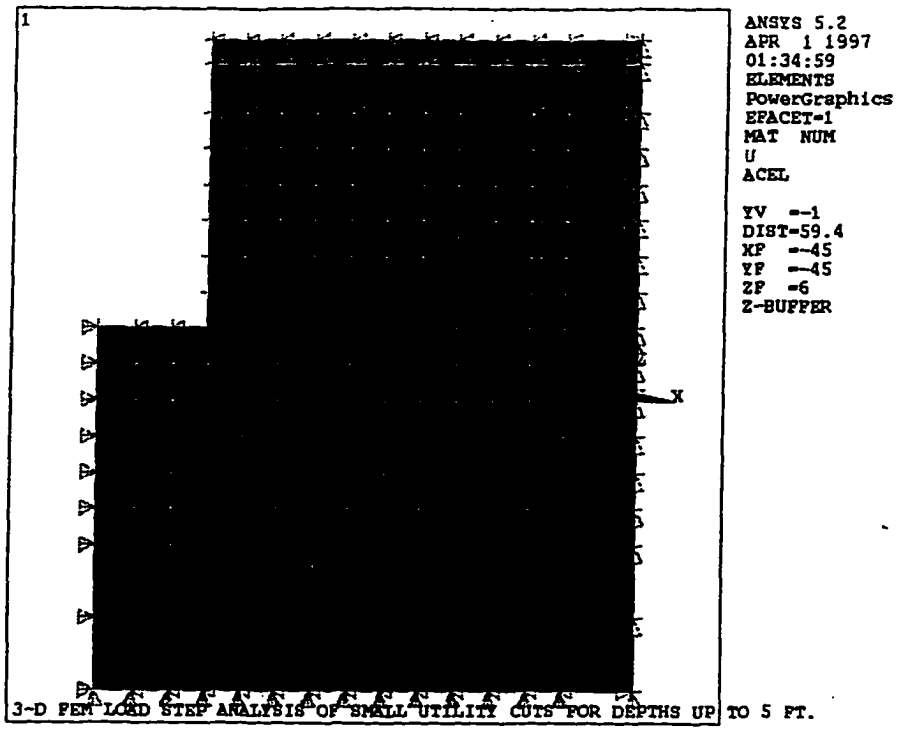

Figure 7.3(h)

Elevation of the Finite Element Model used in Time Step 9. Cut Excavation 4 ft. Deep.

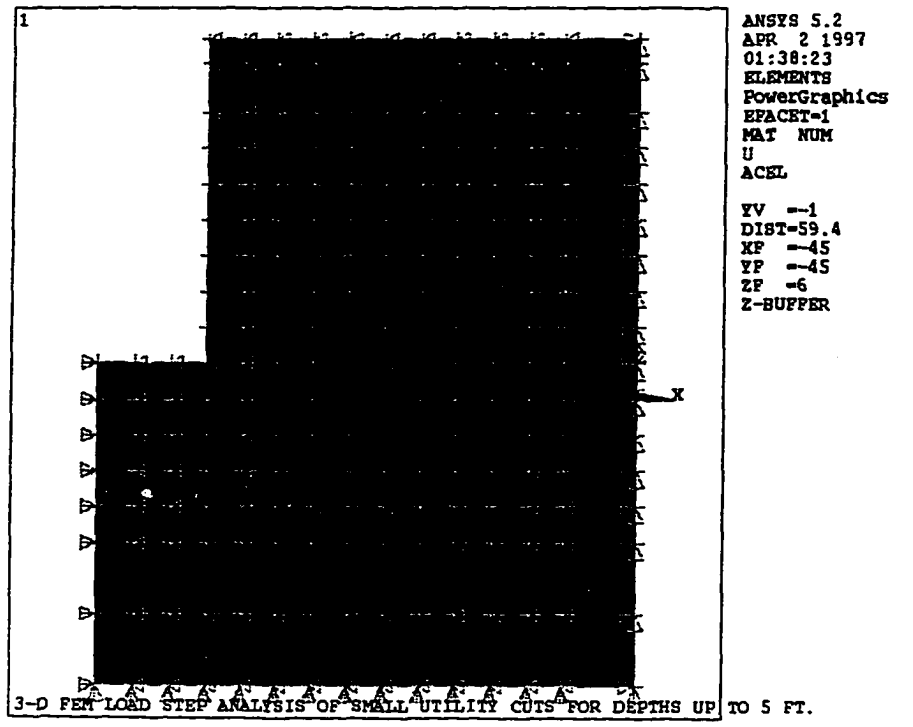

Figure 7.3(i)

Elevation of the Finite Element Model used in Time Step 10. Cut Excavation 4.5 ft. Deep.

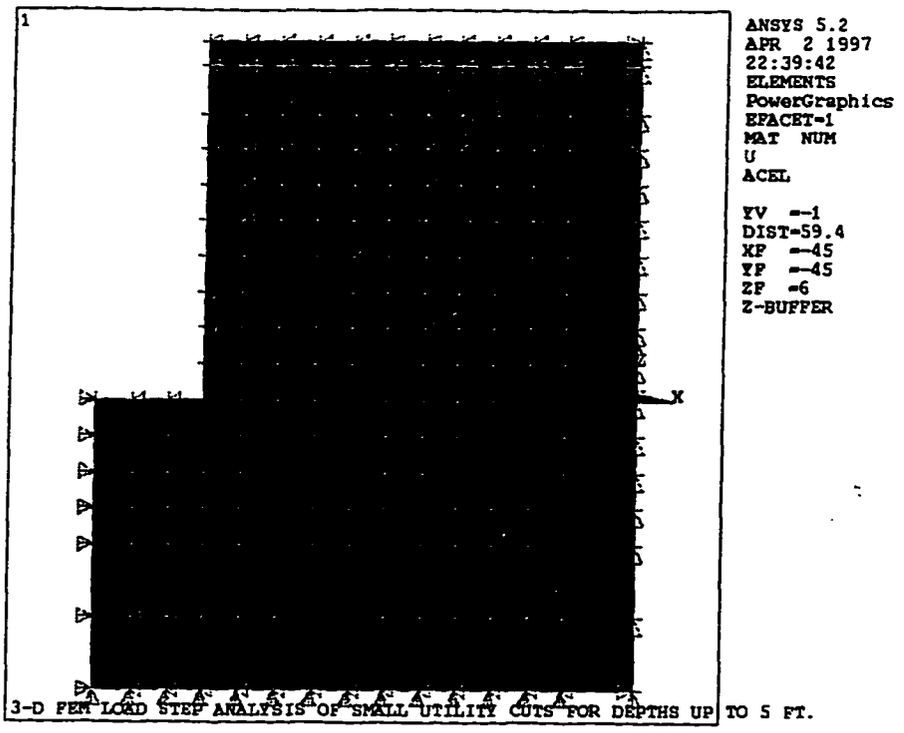

Figure 7.3(j)

Elevation of the Finite Element Model used in Time Step 11. Cut Excavation 5 ft. Deep.

The models were constructed to measure, in some detail, the nodal distresses in the soil due to progressive excavation to a depth of 5 feet. From the foregoing we can summarize the following.

For Time Step 1:

- All nodes located on the vertical plane established along the centerline X-axis of the utility cut are restrained with a zero displacement in the Y-direction, except the bottom nodes which are also restrained with a zero displacement in the Z-direction. (See Figure 7.1 and Figure 7.2).
- All nodes located at the apex of the 1/8 model on the vertical plane established along the centerline Y-axis of the utility cut are restrained in the X-direction, except the

bottom nodes, which are also restrained with a zero displacement in the Z-direction. (See Figure 7.2).

- The nodes along the back wall which runs parallel to the Y-axis and bounded by Nodes 15 through 295 are restrained with a zero displacement in the X-direction, except the bottom nodes which are also restrained with a zero displacement in the Z-direction. (See Figure 7.2).
- The diagonal plane bounded by node #1 through node #295 were restrained with a zero displacement in the Y-direction, perpendicular to that plane. See Figure 7.2(a).
- All other nodes in the model have 3 degrees of freedom, except the nodes located at the bottom of the model which are restrained with a zero displacement in the Z-direction only.

For Time Step 2 to Time Step 11

- With the assumption that beyond a distance of 6 feet from the face of the utility cut, for Time Steps 2 to 11, the vertical plane of nodes bounded by node #15 through node #295, (see Figures 7.1(a) and 7.1(b)) received a Z-direction constraint, with the respective layer displacement values obtained from the results of the Time Step 1 analysis.
- The vertical plane of nodes bounded by node #15 through node #295 were also restrained in the Y-direction to ensure complete fixity of the displaced model from Time Step 1, assuming no impacts from the cut at this distance from the cut and stable soil conditions. (See Figures 7.2(a) to 2(j)).

- The model assumes no support to the wall of the utility cut during the Time Step analysis.

LOADING

Inertia Loading

The model was subjected to gravity forces in the Z-direction only and allowed to respond to the release of stresses due to the excavation process

Asphalt Concrete Modulus

The asphalt concrete (AC) surface modulus of elasticity (E) values can range from 0.3 x 10^6 to 1.8 x 10^6 psi, (Oglesby and Hicks 1982, 687), for moderate temperatures. The E values for AC are recorded as ranging among 1.8 x 10^6 psi at 40°F; 0.6 x 10^6 psi at 60°F; 0.27 x 10^6 at 80°F; 0.145 x 10^6 psi at 100°F and 0.1 x 10^6 psi at 120°F (Yoder and Witczak 1975, 520). This research assumed an asphalt concrete E value of 0.48 x 10^6 psi, corresponding to an average temperature of 70° in the warmer months. The research further assumed that the AC remained in the elastic range after the utility cut is made, because of the low stress applications to the material and more so, when modeled plastically did not yield solutions. The AC surface is expected to contribute some stiffness to the model, considering the magnitude of its E value, compared to the significantly lower E value in the base layer at interface of the materials.

Granular Material Modulus

The modulus of elasticity (E) values for the granular materials in the model were developed from an elastic relationship commencing with the computation of the effective vertical stresses, σ_v. From this stress the average effective confining stress was computed:

$$\bar{\sigma}_c = \frac{\bar{\sigma}_v(1 + 2K_0)}{3} \quad (7.1)$$

where it was assumed in this analysis that:

the coefficient of lateral stress $K_0 = \frac{\nu}{1 + \nu} = 0.8$ (7.2)

This was based on the assumption that the road materials were well compacted when laid, and that with time the road structure is kneaded into a denser state from traffic loading and vibration. The literature states that for a material that was tamped in layers such as a roadbed material the K_0 value would be in the region of 0.8. (Terzaghi & Peck, p188). The roadbed having satisfied this condition for compaction, this value was used in the research to determine the horizontal stress in the model.

From Equation (7.2), and for $K_0 = 0.8$, Poisson's ratio is computed to be;

$$\nu = 0.4444$$

From Hardin and Black, 1968 the shear modulus, G_{max} was defined as:

$$G_{max} = \frac{1230(2.973 - e)^2 \bar{\sigma}_c^{1/2}}{1 + e} \quad (7.3)$$

(Lambe and Whitman 1969, 455)

where $\bar{\sigma}_c$ is the average effective confining pressure:

$$\bar{\sigma}_c = \frac{1}{3}(\bar{\sigma}_1 + \bar{\sigma}_2 + \bar{\sigma}_3) \quad (7.4)$$

where, $\bar{\sigma}_1$, $\bar{\sigma}_2$, $\bar{\sigma}_3$, are the major, intermediate, and minor effective principal stresses. See Equation (6.48).

Based on the material properties selected, the analysis assumes:

$$e = 0.48$$

and from (6.18a) the modulus of elasticity,

$$E = 2(1+\nu)G_{max} \tag{7.5}$$

To determine the material modulus by layer, the average vertical stresses were first determined employing the use of Equation (7.6) and the average effective confining stress computed from Equation (7.1). This enabled the modulii to be computed for the mid-depth of each layer of the model.

$$\sigma_v = \sum \gamma \Delta z \tag{7.6}$$

where

σ_v = Vertical geostatic stress

γ = Unit weight for the respective soil layer

Δz = The respective layer depths

Computer Software Application

The software used for the analysis Utility Cut models is the ANSYS - Engineering Analysis System, Revision 5.0A, 1993, produced by Swanson Analysis Systems Inc. The education version of ANSYS was used for this analysis.

The research specifically used the ANSYS SOLID 45 three dimensional structural element with the Drucker-Prager (DP) material behavior option for soils analysis, which enables the application of the Mohr-Coulomb failure criteria. (See Chapter VI of this

dissertation for more details of the Drucker-Prager failure criterion used in this research). The ANSYS Solid 45 Element was used to analyze the 3-D solid models for the soil structures used in this research. The Solid 45 Element has 8 nodes, each with 3 degrees of freedom, and with translations in the nodal X, Y and Z directions. The Solid 45 Element has the capabilities for plasticity, creep, swelling, stress stiffening, large deflections and large strain and is described below in Figure 7.7.

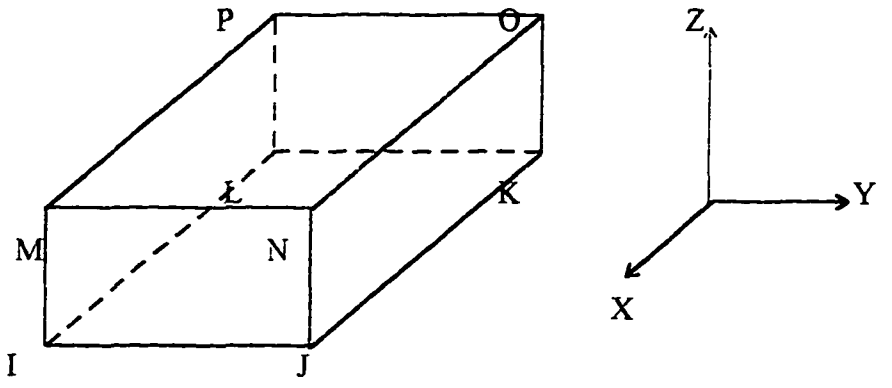

Figure 7.7

ANSYS Solid 45 - three-dimensional structural solid

The figure shows the element and its relationship to the global coordinate system and this is the identical numbering sequence that is used in detailing the elements of the models used in this research. With the use of the Drucker-Prager option the research effort was able to carry out non-linear static analysis on the models.

Appendix C shows an example of an input file and shows what material properties are required. Basically the material property inputs required are:

- Modulus of Elasticity
- Poisson's Ratio
- Density

For the application of the Drucker-Prager option the information required are:

- Cohesion value (must be > 0).
- Angle of internal friction (in degrees).
- Dilatancy angle (in degrees). This is the increase in material volume due to yielding. (For the application of the associative rule used in this research, the dilatancy angle is the same as the input angle of internal friction). "If the dilatancy angle is equal to the friction angle, the rule is associative. If the dilatancy angle is zero (or less than the friction angle), there is no (or less of an) increase in material volume when yielding and the flow rule is non-associative." (ANSYS User's Manual, Volume III, Elements 1991, 2-16).

The Cohesion Value

The Drucker-Prager option used in this research was explained in Chapter VI. This option which. is applicable to granular (frictional) material such as soil, requires the inclusion of a cohesion value (which must be > 0) in order to enable its formulation.

The Researcher, in previous tests had tested the model with an almost pure combination of cohesionless materials. This attempt resulted in stability problems in the model, requiring high angles of internal friction to obtain stable solutions. Actual field conditions show cuts that are stable due to the presence of cohesive properties in the road structure soils. Sensitivity analyses were conducted to determine the region of the minimum cohesion value necessary to obtain cut stability (considering Northeast USA weather related impacts), that could be input into the model.

The analysis performed for each Time Step in this research is that for rate independent plasticity in the pavement material surrounding the Utility Cut. Rate independent plasticity is defined as, "...the irreversible straining that occurs in a material once a certain level of stress is reached (ANSYS User's Manual, Volume IV, Theory 1991, 4-4). The plastic strains are assumed to develop instantaneously, that is, independent of time."

The DP material behavior option "...is applicable to granular (frictional) material such as soils, rock and concrete and uses the outer cone approximation to the Mohr-Coulomb law." (ANSYS User's Manual, Volume III, Elements 1991, 2-16).

Any further information required by the reader on the use of the ANSYS software can be obtained by consulting the referenced software manuals.

MODEL INPUTS

To evaluate the impacts of utility cuts in urban street pavements, a 9 feet deep model was analyzed in this research, subject to gravity forces, discussed earlier. Table A.1 in Appendix A shows the inputs to the model in Time Step 1. Succeeding Time Steps used the input data except for modifications to the E-values for some layers, which will be explained in Chapter VIII.

CHAPTER VIII

ANALYSIS AND RESULTS

This chapter reports on the analyses conducted to determine the impacts of small utility cuts in urban street pavements. Results from the theoretical analyses in this research indicated that when a utility cut is made in granular road bed materials, the lateral compression from geostatic forces and vertical pressure from soil overburden caused localized stretching to occur in the soil surrounding the open utility cut.

The stretching in the soil was represented in the analysis by displacement and strain characteristics, generated by the release of soil confinement, as the utility cut excavation progressed. Soil stretching around a utility cut was portrayed by positive strains which continued up to a point (edge of the stretching zone) beyond which, the soil exhibited constant strain, then negative strain characteristics (indicating compression) near the back wall of the model. The stretching pattern was also shown in the displacement results. These results showed an initially large nodal displacement at the face of the cut and a decreasing pattern of displacement in each succeeding node, up to the end of the stretching zone. Beyond the stretching zone, an almost constant displacement was seen, indicating some soil stability. The stretching pattern in the soil indicated that a localized distress zone is created in the soil surrounding the utility cut after it is opened, with these distress characteristics being identified for distances up to approximately 3.5 feet from the face of the utility cut, for depths up to 5 feet.

Further evidence of distress to the area surrounding the utility cut was determined from the results of the confining stress in the material. These results showed a degradation of the confining stresses as the cut depth increased. Vertical stress distributions also indicated stable vertical stresses away from the cut and a decreasing pattern of vertical stresses in the area close to the face of the utility cut. Together with these observations of distress, the displacement plot of the model indicated face displacements and a decreasing pattern of nodal displacements in the planes parallel to the face of the cut as the distance increased from the face of the cut into the soil mass.

The results obtained in this research may explain to some extent the surface distress characteristics observed by the investigators (Shahin and Crovetti 1985), when they conducted their study on street pavement distresses in the vicinity of utility cuts. (See Chapter II). Their analysis, which did not consider cut depth and material characteristics, determined that the pavement area, adjacent to the utility cut, exhibited deflection characteristics, for measured distances of up to approximately 3 feet from the face of the cut.

Early analyses in this research determined that the affected distance from the face of the small utility cut is a function of depth of the cut, soil angle of internal friction and soil cohesion. For the similar properties just mentioned, the research determined that density did not impact the extent of the distress in the material.

It is important to be reminded of the definition of plastic equilibrium in Chapter I. An element of soil can be changed from a state of *elastic equilibrium* to that of *plastic equilibrium* by stretching the entire mass uniformly in a horizontal direction, or by

uniformly compressing the mass in the same direction, with the pressure on the base remaining the same. (Karl Terzaghi 1943, 28).

Worst Case Analysis

Several computer runs were done with the worst case model (defined in Chapter VII) to determine the minimum cohesion value, with which a stable solution (plastic equilibrium) could be obtained. Based on results obtained from the 2^7 worst case models analyzed, distinct trends were observed in the soil surrounding the utility cut, as the mass achieved plastic equilibrium, due in part to the application of the geostatic loading to the back wall of the model. Two patterns of soil behavior were observed:

1. Soil node movement in each layer indicated a maximum displacement at the face of the utility cut, with succeeding nodes behind the face node displaying decreasing displacement values, up to a distance where the decreasing pattern of nodal displacements ceased. This area is referred to in this research as the *stretching zone*. The point where the decreasing pattern of nodal displacements ceased for each layer, is referred to in this research, as the *locus of the displacement/distress envelope.*
2. It was observed in the results, that beyond the boundary of the displacement/distress envelope, the horizontal nodal displacements showed an increasing pattern in each succeeding node, with nodal displacement increasing over and above that of the preceding node, as the distance increased away from the face of the cut. This area is referred to in this research, as the *compression zone.*

The 27 worst case models were initially tested at the 3 feet and 3.5 feet depths, with three density combinations, representing the lower, middle and upper values for the

density ranges of the selected materials. (See Table 7.2). These combinations are detailed in Table 8.1. In Chapter VII, the matter of including a cohesion value in a granular soil analysis was explained. The Researcher reviewed the results of the 3 feet, and 3.5 feet utility cut analyses, in which the approximate minimum cohesion values for stability were determined for the respective states of plastic equilibrium. The review of the stretching impacts showed general similarities among the three density combinations and three ϕ scenarios, used in this research. (See Table 8.1). Based on this similarity, the Researcher determined that an analysis of Density Combination 2 (the mid-range of the density combinations used in this research),with the three ϕ scenarios, would suffice to determine typical distresses that could occur in the vicinity of utility cuts.

Table 8.1 gives a summary of the results of the analyses done on the 27 worst case models, indicating the main results of the analysis. The information in the table includes:

- The maximum distance of the stretching zone from the face of the utility cut.
- The maximum nodal displacement towards the cut.
- The minimum cohesion value required to ensure cut stability.
- A table showing, the three density combinations used in the research.
- A table showing, the three ϕ scenarios used in the research.
- A chart showing the relationship between cut depth and the minimum cohesion value for each ϕ scenario, under Density Combination 2.

For example, for Density Combination 2, ϕ Scenario #2, the table shows a maximum stretching zone of 3.5 feet from the face of the cut, with a maximum displacement of 0.031991 in., for a soil cohesion value of 0.295 lb/in^2.

Table 8.1

Maximum stretching distance in the fill, measured from the face of the utility cut (feet) - worst case model (for minimum cohesion values)

Note: Maximum nodal displacement distances (inches), located (in italics) below the respective maximum stretching distances

CUT DEPTH (feet)	DENSITY COMBINATION 1			DENSITY COMBINATION 2			DENSITY COMBINATION 3		
	PHI SCENARIO			PHI SCENARIO			PHI SCENARIO		
	Scenario #1	Scenario #2	Scenario #3	Scenario #1	Scenario #2	Scenario #3	Scenario #1	Scenario #2	Scenario #3
3	2.5	3	2.5	2.5	3	2.5	2.5	3	2.5
	0.018293 in.	*0.021291 in.*	*0.019999 in.*	*0.018731 in.*	*0.020905 in.*	*0.020791 in.*	*0.018788 in.*	*0.021747 in.*	*0.021709 in.*
3.5	2.5	3	3	2.5	3	3.5	2.5	3	3.5
	0.018268 in.	*0.021270 in.*	*0.025796 in.*	*0.018780 in.*	*0.021682 in.*	*0.027392 in.*	*0.019145 in.*	*0.022355 in.*	*0.028130 in.*
4				3	3.5	3			
				0.025993 in.	*0.027327 in.*	*0.027841 in.*			
4.5				3	3.5	3			
				0.026733 in.	*0.031991 in.*	*0.030342 in.*			
5				3	3	2.5			
				0.033282 in.	*0.034088 in.*	*0.036065 in.*			

MINIMUM COHESION VALUES (lb/in^2)

CUT DEPTH (feet)	DENSITY COMBINATION 1			DENSITY COMBINATION 2			DENSITY COMBINATION 3		
	PHI SCENARIO			PHI SCENARIO			PHI SCENARIO		
	Scenario #1	Scenario #2	Scenario #3	Scenario #1	Scenario #2	Scenario #3	Scenario #1	Scenario #2	Scenario #3
3	0.3354775	0.265	0.20575	0.35785	0.287	0.2175	0.38125	0.3025	0.2275
3.5	0.38	0.29	0.178739	0.40625	0.3125	0.1871	0.4325	0.33	0.19875
4				0.40875	0.30125	0.1825			
4.5				0.43625	0.295	0.25875			
5				0.4525	0.325	0.32078			

DETAILS OF THE DENSITY COMBINATIONS USED IN THE RESEARCH (lb/ft^3)

	1	2	3
BASE	125	133	140
FILL	110	120	130

DETAILS OF THE PHI SCENARIOS USED IN THE RESEARCH (Degrees)

	#1	#2	#3
BASE	32	36	40
FILL	30	34	38

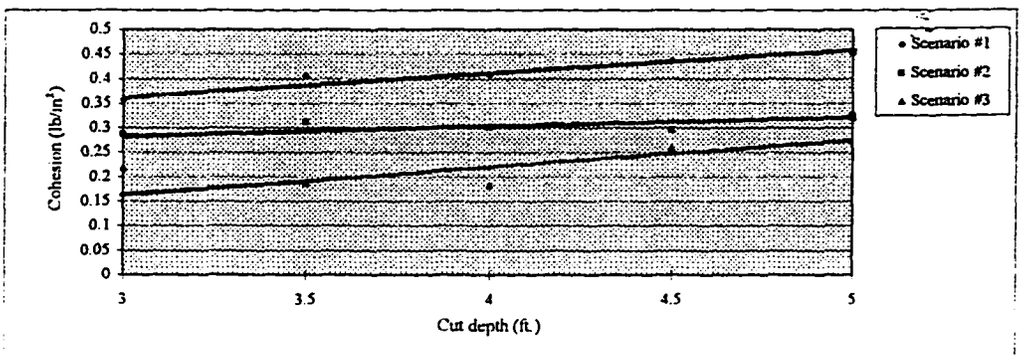

Plot of minimum cohesion values from table above which enabled cut stability for the three Phi Scenarios, Density Combination 2

Stress Relief Analysis

Comparative analyses were done, using a stress relief approach, which tended to simulate a graduated excavation process. This simulation of the excavation process was achieved via the use of a time step analysis, which used the results from the previous time step to analyze the next time step, after the graduated excavation was simulated for the new step. The new time steps used the element stress results from the previous time step analysis to determine the average effective confining stress of the respective layers to obtain modified E-values. These modified values were included in the inputs to the model for the new time step analysis.

For the time step analysis, a road structure was analyzed as follows:

1. A 4" asphaltic surface and with material properties $\gamma_{SURFACE} = 148$ lb/ft^3
2. An 8" base course with material properties $\gamma_{BASE} = 133$ lb/ft^3 and $\phi_{BASE} = 36°$
3. A 96" fill/subgrade material with properties $\gamma_{FILL/SUBGRADE} = 120$ lb/ft^3 and $\phi_{FILL/SUBGRADE} = 34°$

These properties corresponded to the properties used in the worst case analysis and typical of the material types used in road construction practice.

The analysis was conducted to determine the graduated distresses to the soil in the vicinity of utility cuts during excavation, for unsupported depths up to 5 feet. The model in Figure 7.2(c) was subjected to the effects of gravity in Time Step 1 and analyzed.

Figures 7.3(a) to 7.3(j) show the elevations of the soil models and the excavation sequence from Time Step 2 to Time Step 11. Time Step 2 has the asphaltic concrete surface removed in the excavation area for the utility cut. Time Step 3 has the granular

base removed. Time Step 4 has the first 6" of fill/subgrade layer removed. Each succeeding Time Step removed 6" of fill/subgrade material until the 5 ft. Depth was achieved.

It was assumed for the time step analysis that at a distance of approximately 6 feet from the face of the utility cut there will be no influence from the utility cut on the soil mass around the cut. Therefore, from Time Step 2, and for the remainder of the Time Step analyses, the vertical plane of nodes bounded by node #15 through node #295, (see Figures 7.1(a) and 7.1(b)) received X-, Y- and Z-direction constraints, with the respective Z-displacement values for each layer obtained from the results of the Time Step 1 analysis.

The material properties in Table 8.2 were input into the model for time step 1 and the analysis conducted. From element solutions for nodal stresses, the 24 nodal element stresses were averaged to obtain the effective element confining pressure, and then G_{max}-value and E-value were computed per Equations (7.3) and (7.5). The E-values computed from the average effective element confining stress showed that the initial input E-values into the model were the same as the model generated results after the completion of Time Step 1.

Table 8.2

CALCULATION OF MODULUS OF ELASTICITY FOR UTILITY CUT ANALYSIS FOR CUTS UP TO 5'-0" DEEP

COMPUTED E-VALUES PRIOR TO CONDUCTING THE LOAD STEP 1 ANALYSIS

GEOSTATIC STRESSES (pv)					Shear Modulus (G_{max})		Modulus of Elasticity (E)	
Vert. Press. (p_v)	lb/ft^2	lb/in^2	$p_{v\ avg}$ (psi)	Sigma$_o$ (psi)	by layer	(psi)	by Layer	(psi)
P_1	49.33	0.34			G_1		E_1	480,000
P_2	138.00	0.96	0.65	0.56	G_2	3,878	E_2	11,203
P_3	198.00	1.37	1.17	1.01	G_3	5,194	E_3	15,004
P_4	258.00	1.79	1.58	1.37	G_4	6,051	E_4	17,479
P_5	318.00	2.21	2.00	1.73	G_5	6,800	E_5	19,645
P_6	378.00	2.62	2.42	2.09	G_6	7,475	E_6	21,594
P_7	438.00	3.04	2.83	2.46	G_7	8,094	E_7	23,382
P_8	498.00	3.46	3.25	2.82	G_8	8,669	E_8	25,042
P_9	558.00	3.87	3.67	3.18	G_9	9,208	E_9	26,599
P_{10}	618.00	4.29	4.08	3.54	G_{10}	9,717	E_{10}	28,070
P_{11}	678.00	4.71	4.50	3.90	G_{11}	10,200	E_{11}	29,467
P_{12}	738.00	5.12	4.92	4.26	G_{12}	10,662	E_{12}	30,801
P_{35}	798.00	5.54	5.33	4.62	G_{35}	11,105	E_{35}	32,080
P_{36}	858.00	5.96	5.75	4.98	G_{36}	11,530	E_{36}	33,309
P_{37}	978.00	6.79	6.37	5.52	G_{37}	12,141	E_{37}	35,073
P_{38}	1098.00	7.62	7.21	6.25	G_{38}	12,910	E_{38}	37,295

Model Width = 6 feet

d_1 (ft)	0.33	
d_2 (ft)	0.6667	
d_3 (ft)	0.5	
d_4 (ft)	0.5	
d_5 (ft)	0.5	
d_6 (ft)	0.5	
d_7 (ft)	0.5	
d_8 (ft)	0.5	
d_9 (ft)	0.5	
d_{10} (ft)	0.5	Floor elev. of 5 ft. deep utility cut.
d_{11} (ft)	0.5	
d_{12} (ft)	0.5	
d_{35} (ft)	0.5	
d_{36} (ft)	0.5	
d_{37} (ft)	1	
d_{38} (ft)	1	

NOTE: For this test;

Material Density	lb/ft^3	lb/in^3
Asphalt Density	148	0.0856
Base Density	133	0.0770
Subbase Density	120	0.0694

Material	e_{95}
Base	0.48
Fill	0.48

Phi_{base} 36°

Phi_{FILL} 34°

The first layer (asphaltic concrete surface) was then removed, using the EKILL command available in ANSYS. This command removes all influences of mass and loading of killed elements and assigns a factor of 1E-10 to input properties. As a safety factor, the Researcher assigned an overriding factor of 1E-50 to the input properties to ensure there were no influences of the killed elements on the model.

Using the computed average confining pressure from Equation (7.4), the E-value for layers 3, 4 and 5 under the cut area were modified, together with the two wall elements adjacent to the respective layers. This was done in accordance with the reduced stresses from overburden removal.

Time Step 2 was then run, the average effective confining stresses were computed and the E-values modified for the three layers of elements below the base course layer of the cut, for use in Time Step 3. The first two column elements of these layers bordering the cut face also received modified E-values, based on the computed E-values and comparison with the previous input E-values.

In order to determine the typical elements to be used in the stress relief analysis, the stress results of Time Step 2 were used to compute the E-values of all of the elements in the first layer of the fill/subgrade material, as well as all of the two column wall elements for that layer. The average E-value of the floor elements and the two wall elements were found and the elements that closely matched the respective average values were selected as the typical element locations for determining the average E-value to be input into the succeeding Time Step models. In each succeeding step of the analysis, the elements located directly below these selected elements were used for input into the model. The reader should be reminded that because of the nature of the soil, the E-values for the individual elements will vary, but to minimize voluminous inputs, the average E-values were used as being representative of the array of E-values for the respective layers and wall elements. On completion of the Time Step 2 analysis, the E-values for layers 4, 5 and 6 and their respective wall elements were then computed and modified in line with the

average stresses. The base course (second layer) was then killed giving a 1 foot depth of excavation and Time Step 3 was run to obtain the average effective confining stresses, for the computation of the modified E-values for use in the next time step. The simulated excavation process continued and the third layer elements within the cut were killed, E-values modified and Time Step 4 run. Steps 5 through 11 were analyzed in a similar manner, with each succeeding removal of the 6-inch layer of fill until the 5 feet depth was reached.

Results

Figures 8.1(a), (b) and (c) show the results of the Time Step 1 analysis and depict the vertical displacements, horizontal and vertical stress distributions that occurred in the un-excavated model.

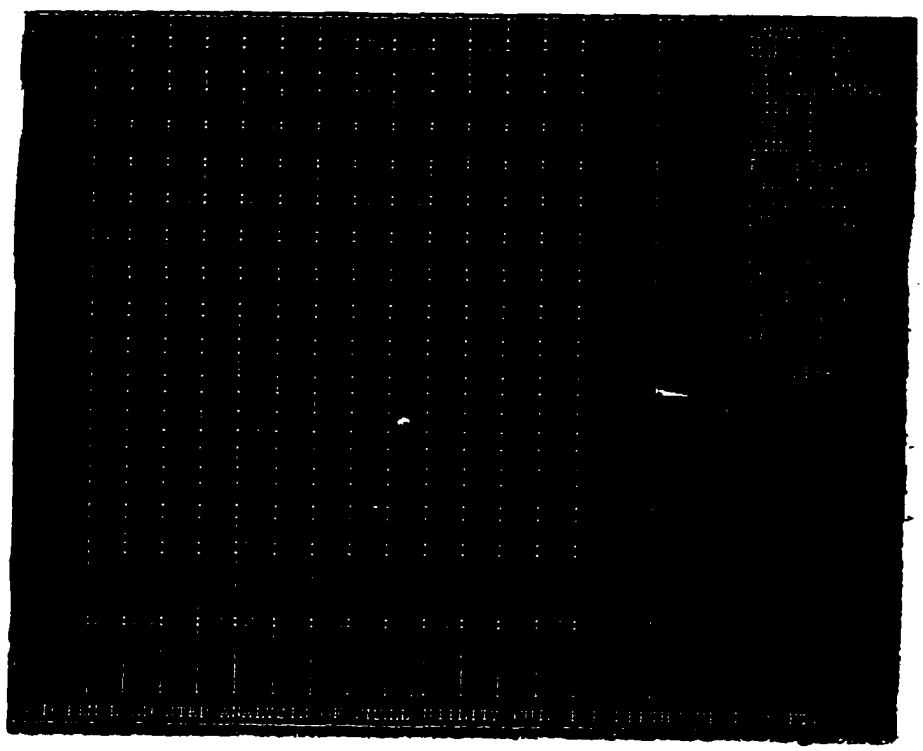

Figure 8.1(a)

Vertical Displacements in the Un-excavated Model. Time Step 1.

Figure 8.1(a) shows the maximum displacement in inches, (DMX) = 0.004153 in., which occurs in this case in the Z-direction, and is the value shared by all of the nodes located at the top row of the model. This vertical displacement of the model was due to the effects of the gravitational forces.

Figure 8.1(b) shows the stresses experienced by the model in the X-direction in psi and shows the levels of confining stresses experienced throughout the model. For example, the uppermost band indicates confining stresses in the range of -0.114133 psi to -0.741746 psi, while the lower band indicates confining stress in the range of -5.135 psi to -5.763 psi. (See legend in figure). Note that the maximum and minimum results are indicated in terms of positive tension stresses, hence Figure 8.1(b) indicates the minimum stress (SMN) as -5.763 psi and the maximum stress (SMX) as -0.114133 psi.

Similarly for the stress in the Z-direction, the uppermost band indicates vertical stresses in the range of -0.1712 psi to -0.952689 psi, while the lower band indicates confining stress in the range of -6.423 psi to -7.205 psi. (See legend in figure). Note here again that the maximum and minimum results are indicated in terms of positive tension stresses, hence Figure 8.1(c) indicates the minimum stress (SMN) as -7.205 psi and the maximum stress (SMX) as -0.1712 psi.

The interpretations just given above will apply to Figures 8.3 and 8.4. In Figure 8.2 the direction of the maximum displacement will either be in the X-direction or a combined direction, as the excavation progresses. These will be identified in the reporting of the results.

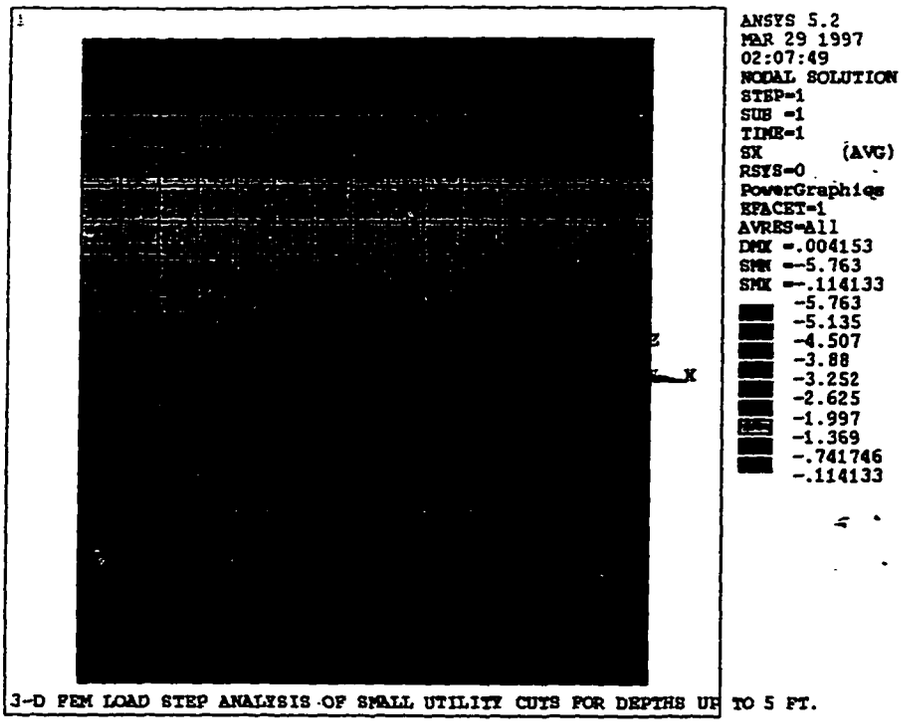

Figure 8.1(b)
Horizontal Stress in the X-direction in the Un-excavated Model. Time Step 1.

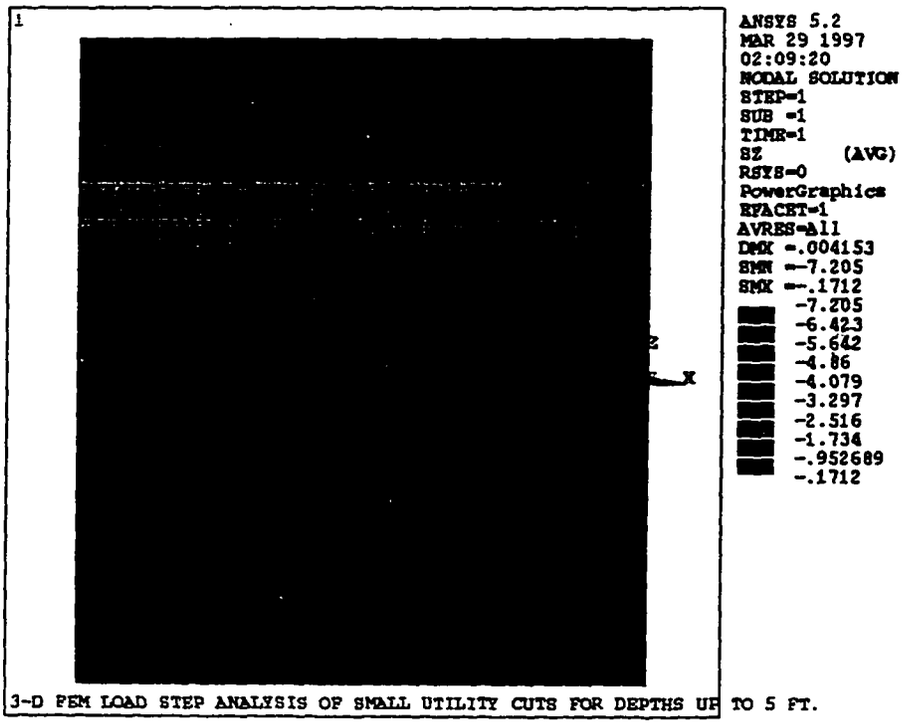

Figure 8.1(c)
Vertical stress in the in the un-excavated model. Time Step 1.

Figure 8.2 shows the development of the nodal displacements in the model from Time Step 2 through Time Step 11, and shows the soil deformation in the floor and the surrounding soil of the utility cut as the excavation progressed. The DMX value in Figure 8.2(a) to Figure 8.2(e) occurs in the Z-direction at Node #190 on the top row diagonal. The DMX value in Figure 8.2(f) occurs at Node #10 for a combined displacement. The DMX value in Figure 8.2(g) to Figure 8.2(j) occurs at Node #9 for a combined displacement. Maximum displacement values in the X-direction, for all steps, can be found in Figure 8.7.

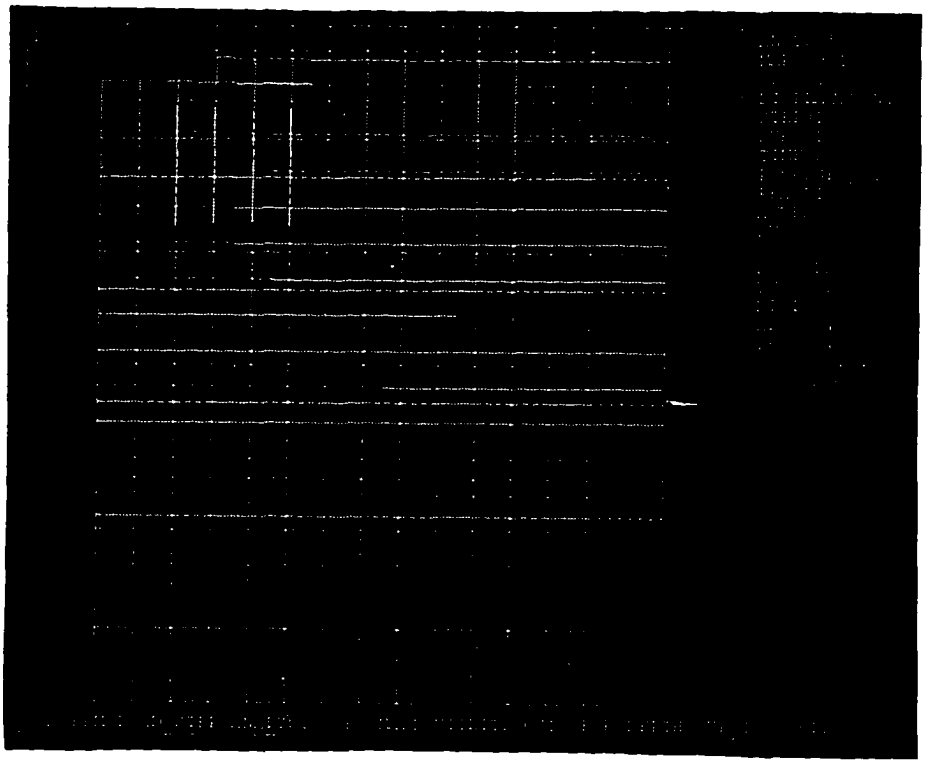

Figure 8.2(a)
Model Displacements in the FEM Model. Time Step 2. Cut Excavation 0.33 ft. Deep.

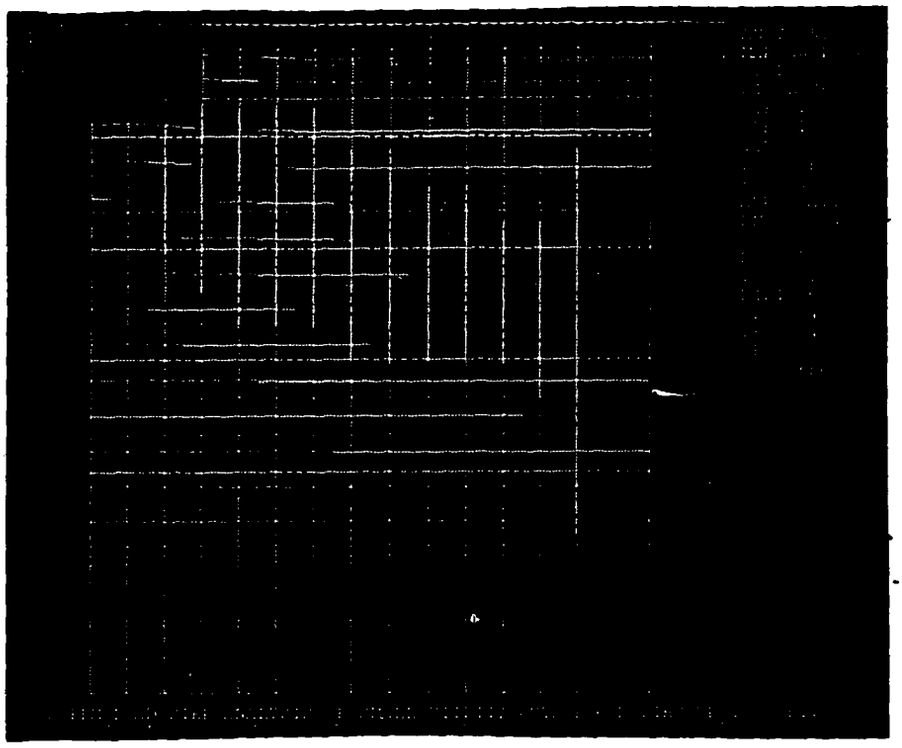

Figure 8.2(b)
Model Displacements in the FEM Model. Time Step 3. Cut Excavation 1 ft. Deep.

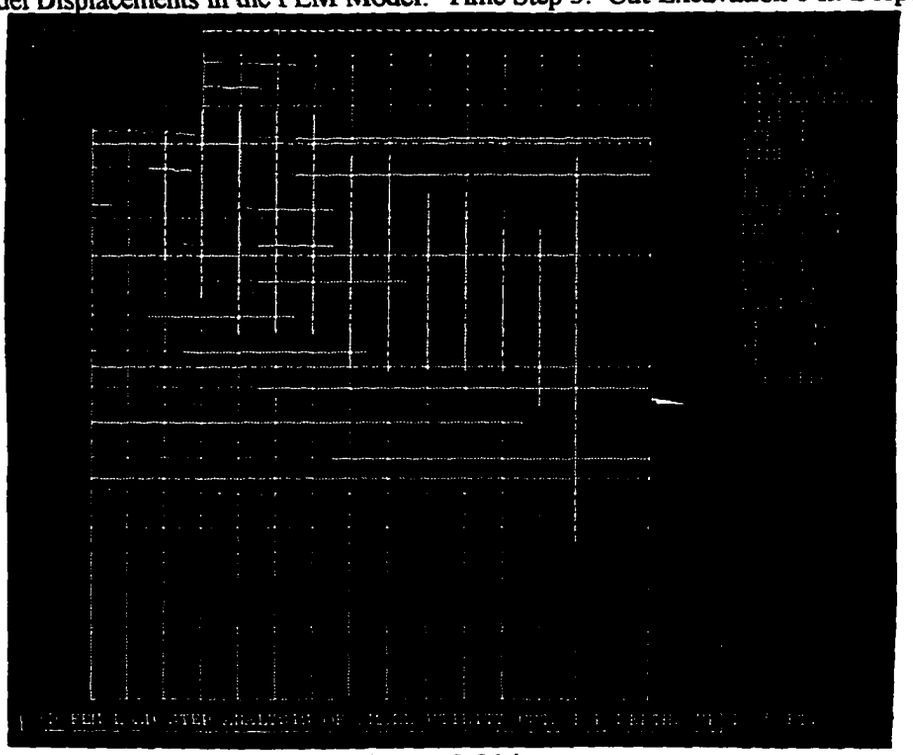

Figure 8.2(c)
Model Displacements in the FEM Model. Time Step 4. Cut Excavation 1.5 ft. Deep.

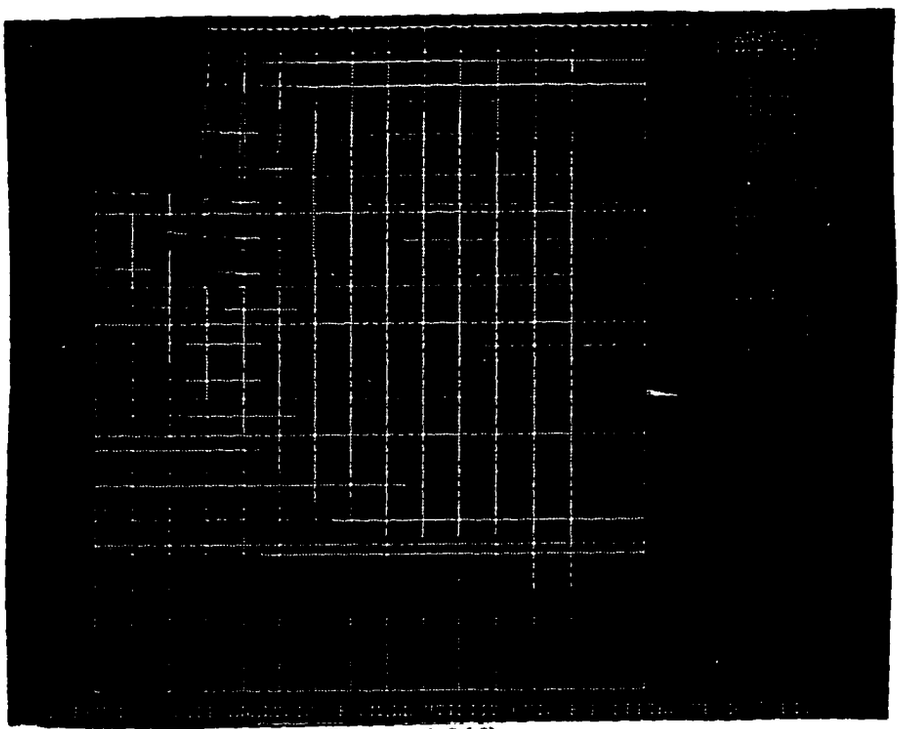

Figure 8.2(d)
Model Displacements in the FEM Model. Time Step 5. Cut Excavation 2 ft. Deep.

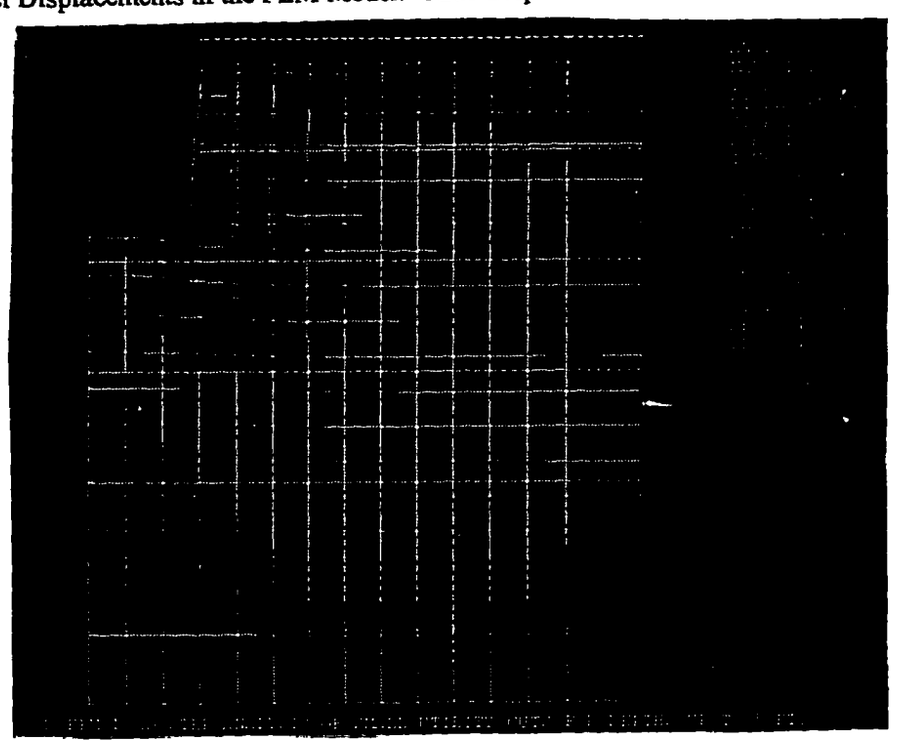

Figure 8.2(e)
Model Displacements in the FEM Model. Time Step 6. Cut Excavation 2.5 ft. Deep.

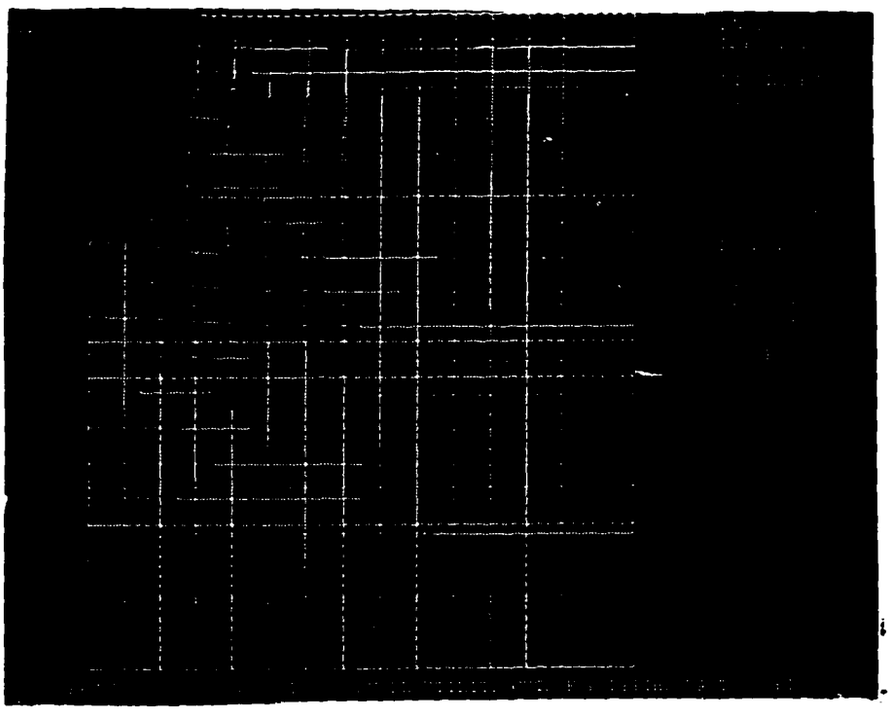

Figure 8.2(f)
Model Displacements in the FEM Model. Time Step 7. Cut Excavation 3 ft. Deep.

Figure 8.2(g)
Model Displacements in the FEM Model. Time Step 8. Cut Excavation 3.5 ft. Deep.

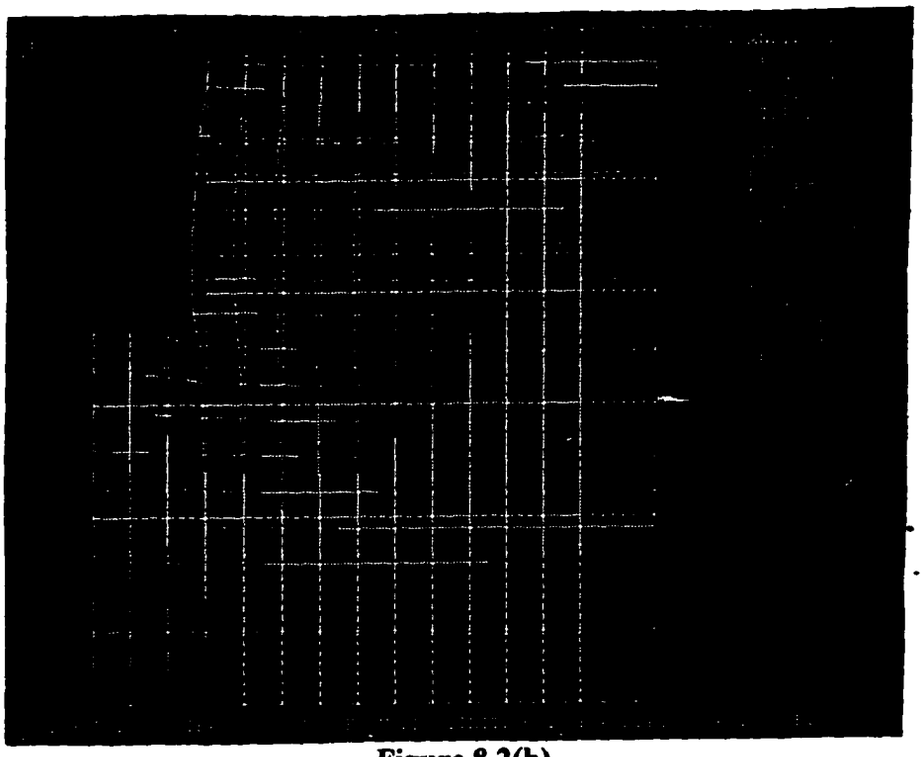

Figure 8.2(h)
Model Displacements in the FEM Model. Time Step 9. Cut Excavation 4 ft. Deep.

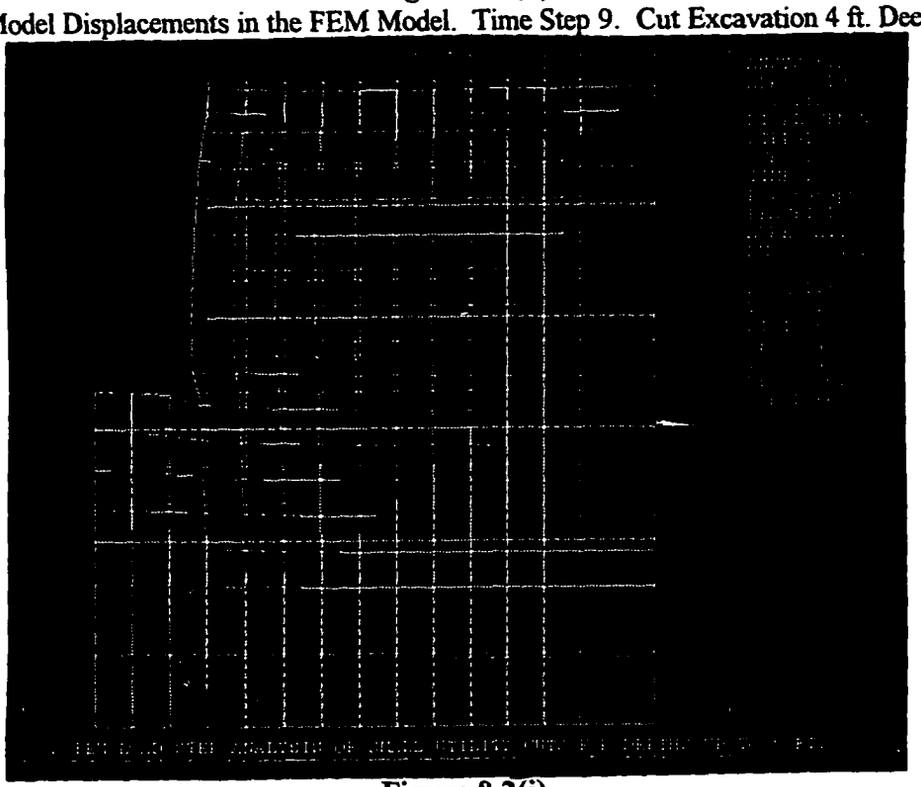

Figure 8.2(i)
Model Displacements in the FEM Model. Time Step 10. Cut Excavation 4.5 ft. Deep.

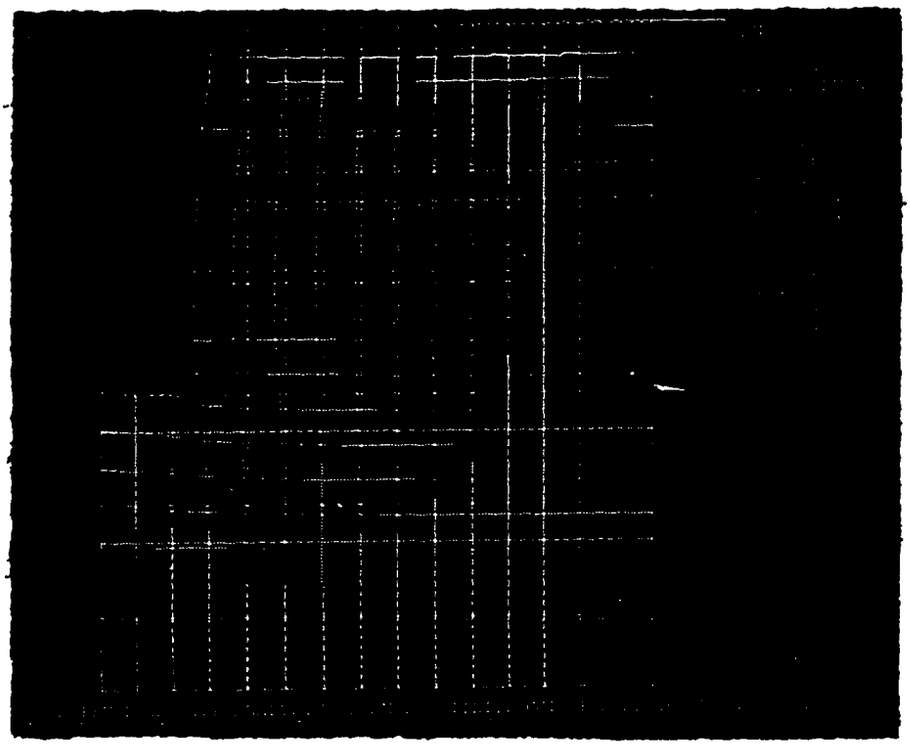

Figure 8.2(j)
Model Displacements in the FEM Model. Time Step 11. Cut Excavation 5 ft. Deep.

Figures 8.3(a) to (j) show the stresses experienced by the model in the X-direction for Time Steps 2 through 11.

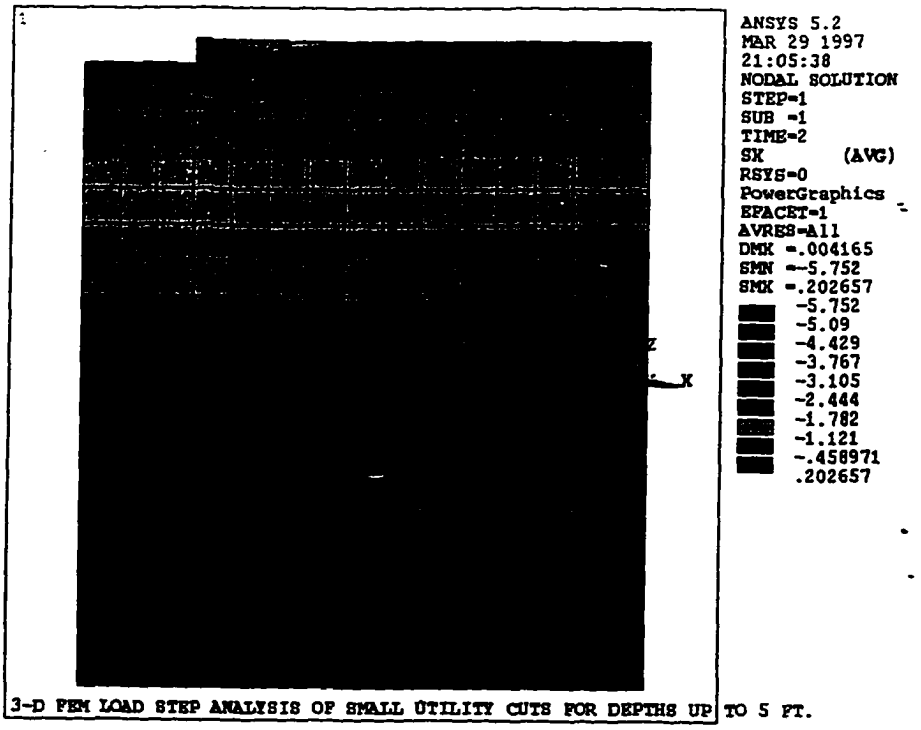

Figure 8.3(a)

Stress in the X-direction in the FEM Model. Time Step 2. Cut Excavation 0.33 ft. Deep.

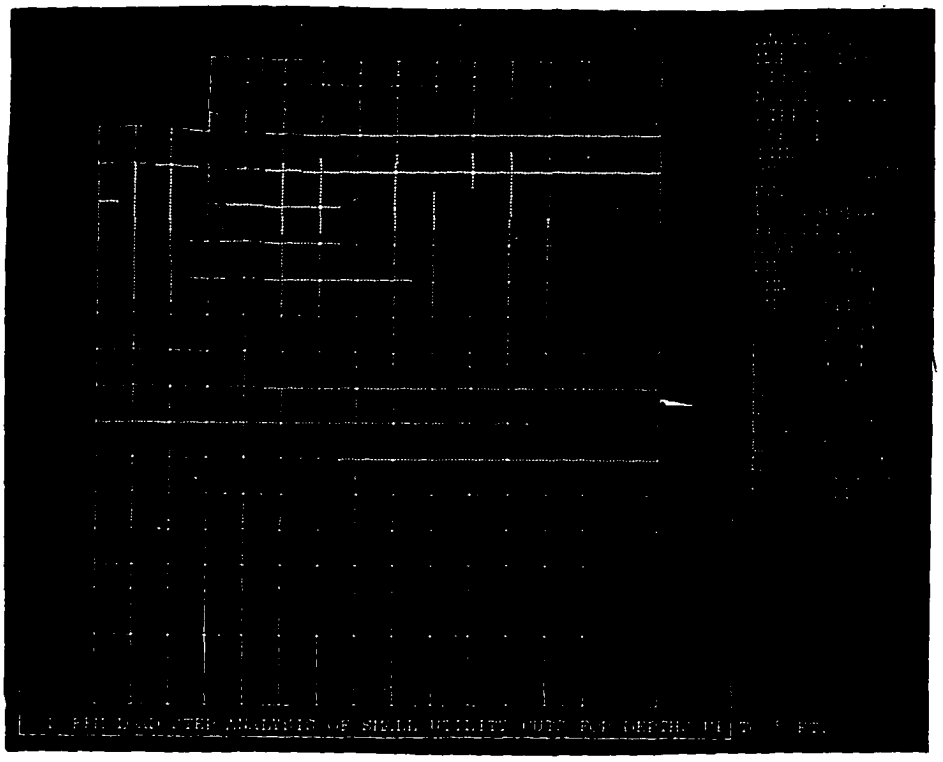

Figure 8.3(b)

Stress in the X-direction in the FEM Model. Time Step 3. Cut Excavation 1 ft. Deep.

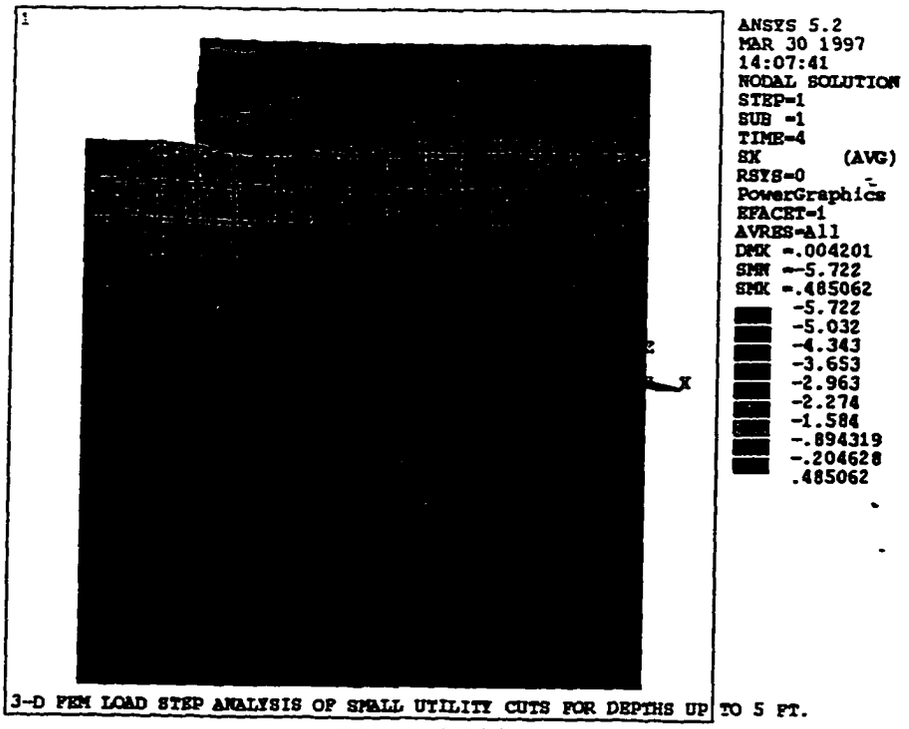

Figure 8.3(c)

Stress in the X-direction in the FEM Model. Time Step 4. Cut Excavation 1.5 ft. Deep.

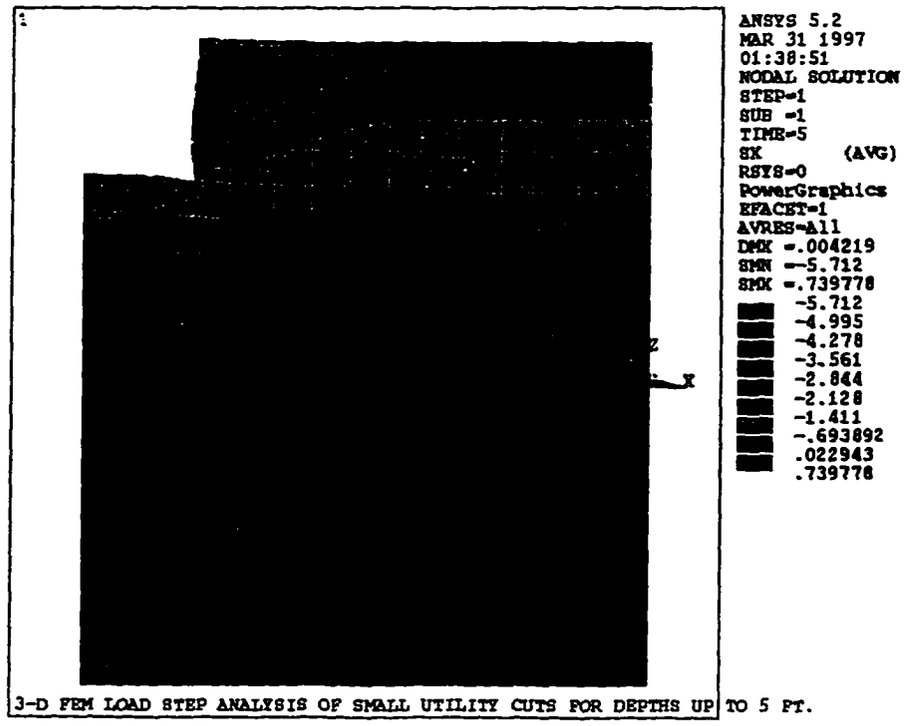

Figure 8.3(d)

Stress in the X-direction in the FEM Model. Time Step 5. Cut Excavation 2 ft. Deep.

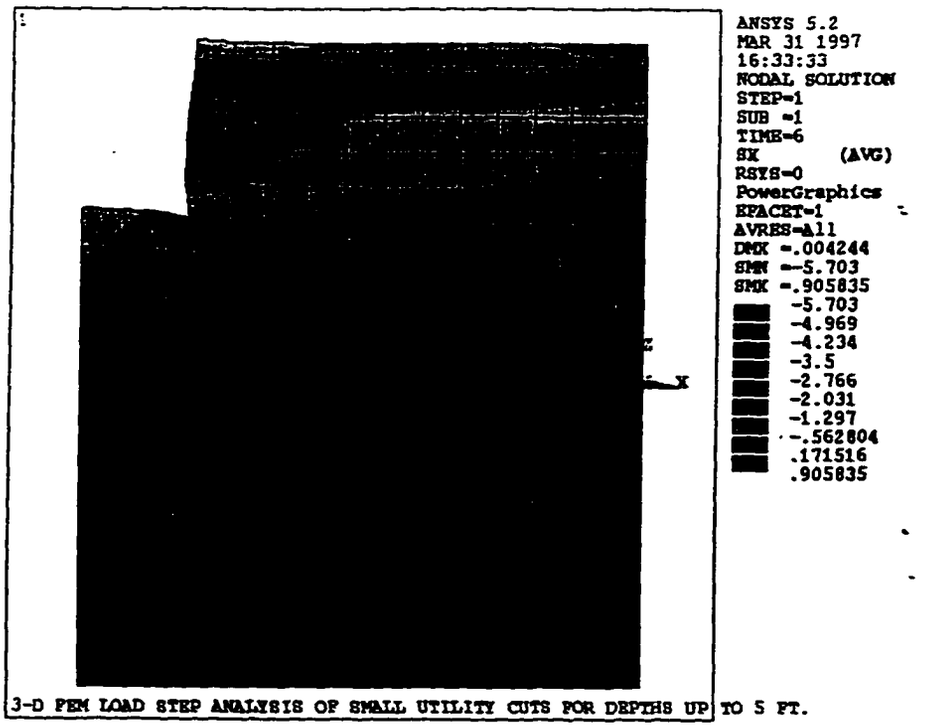

Figure 8.3(e)

Stress in the X-direction in the FEM Model. Time Step 6. Cut Excavation 2.5 ft. Deep.

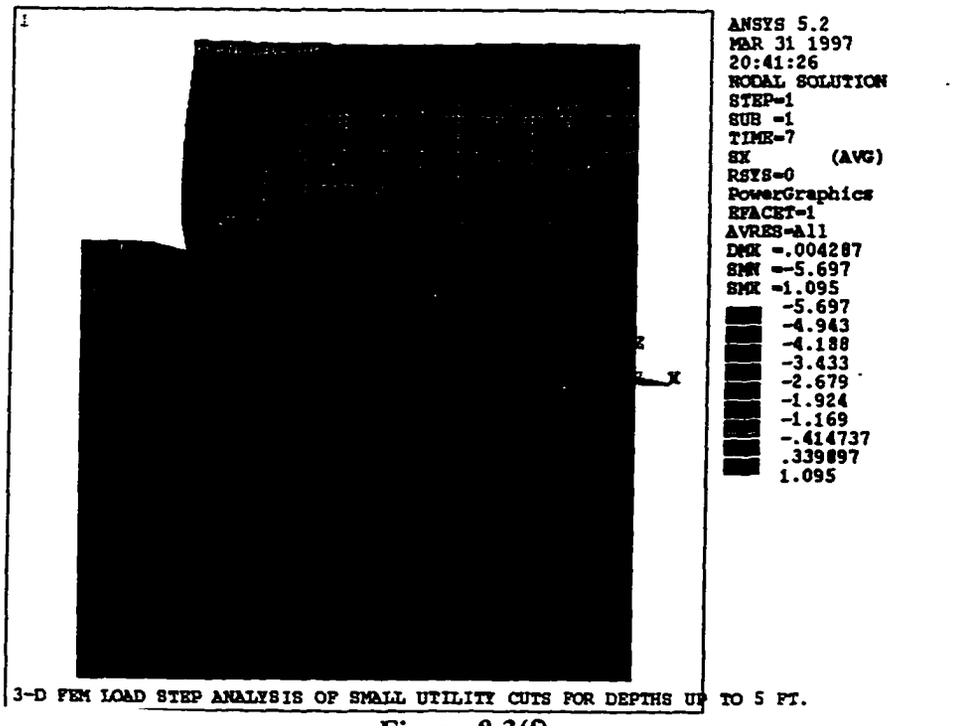

Figure 8.3(f)

Stress in the X-direction in the FEM Model. Time Step 7. Cut Excavation 3 ft. Deep.

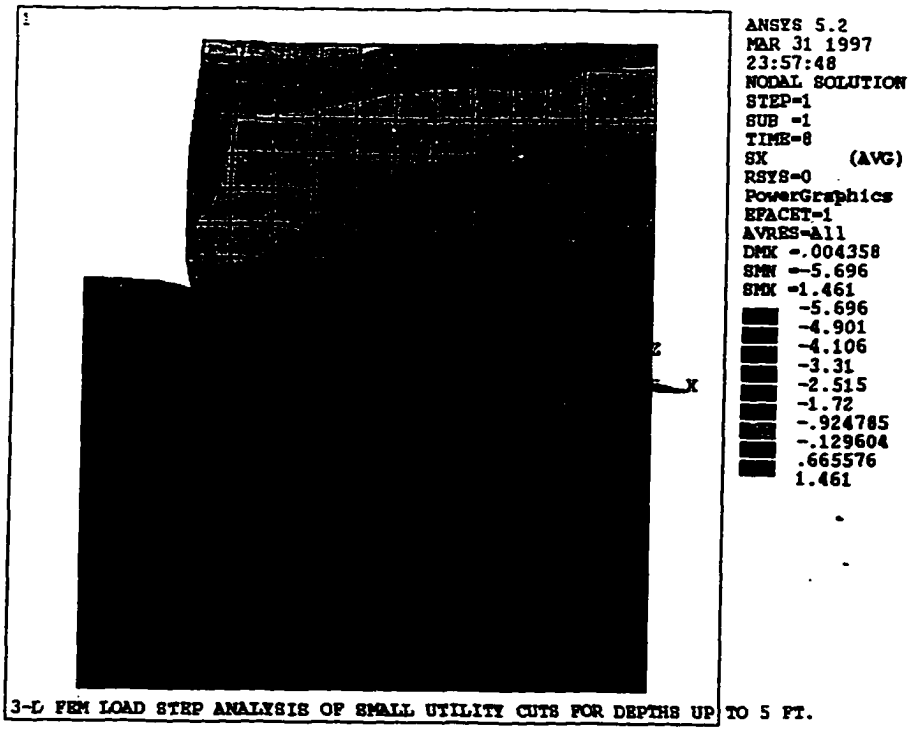

Figure 8.3(g)

Stress in the X-direction in the FEM Model. Time Step 8. Cut Excavation 3.5 ft. Deep.

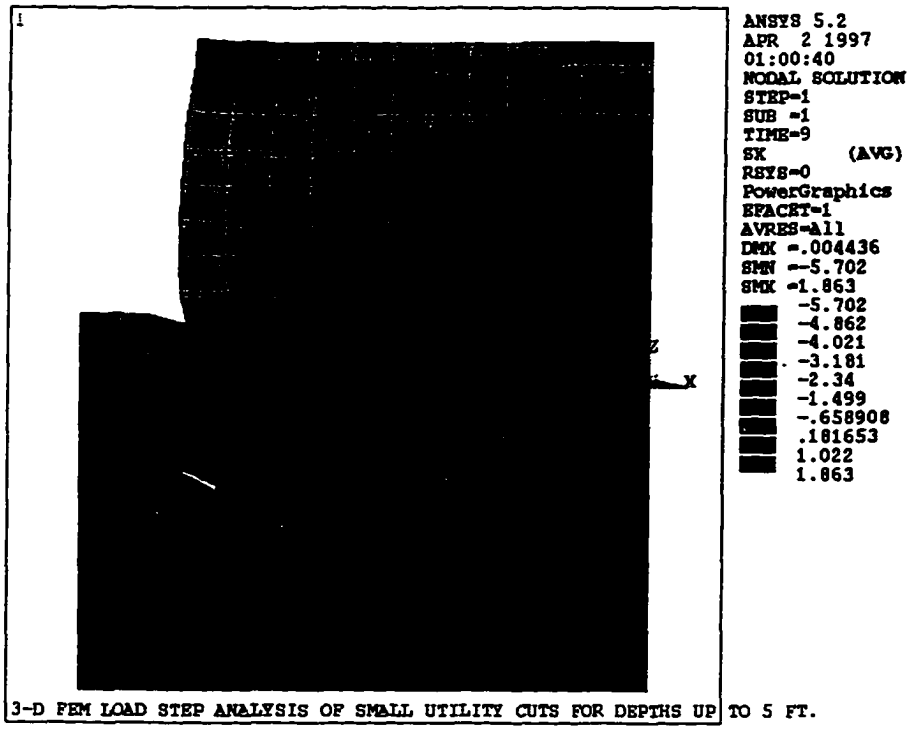

Figure 8.3(h)

Stress in the X-direction in the FEM Model. Time Step 9. Cut Excavation 4 ft. Deep.

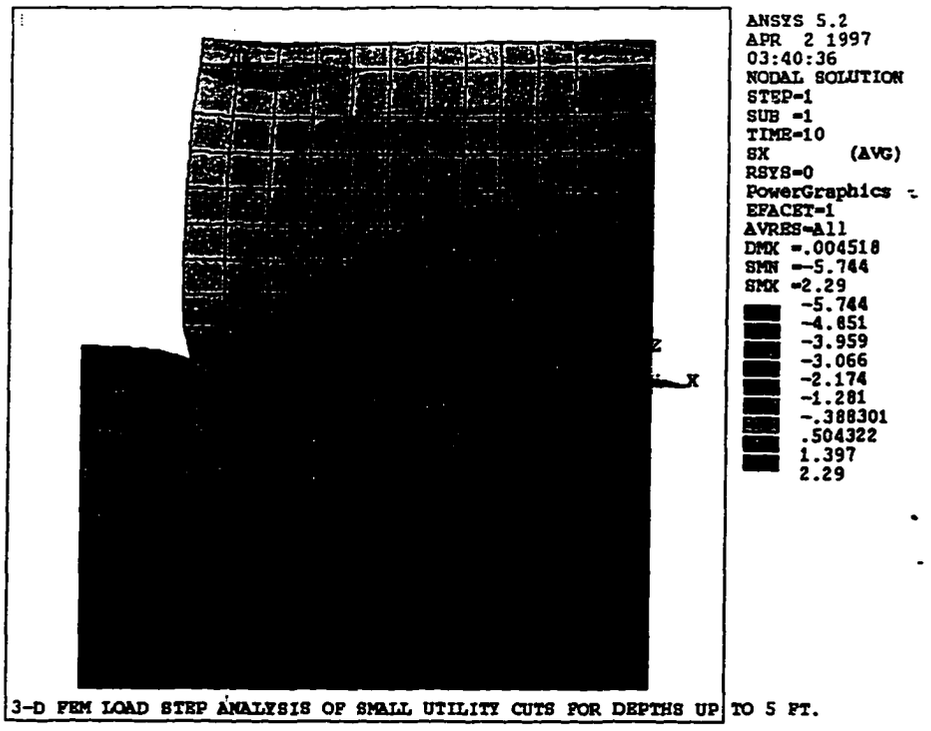

Figure 8.3(i)
Stress in the X-direction in the FEM Model. Time Step 10. Cut Excavation 4.5 ft. Deep.

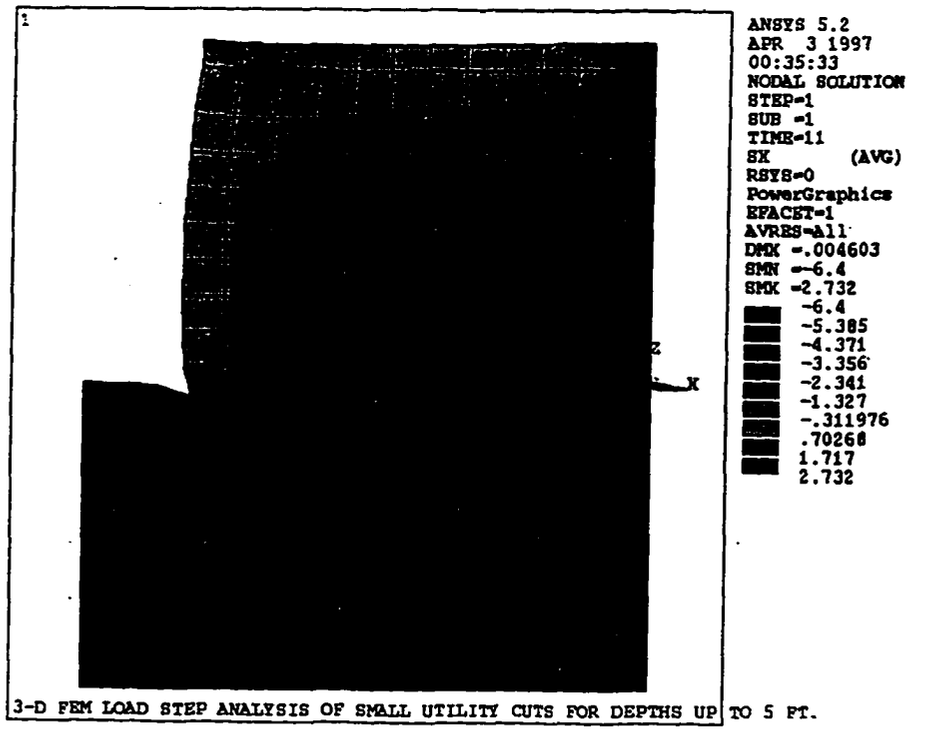

Figure 8.3(j)
Stress in the X-direction in the FEM Model. Time Step 11. Cut Excavation 5 ft. Deep.

Figures 8.4 (a) to (j) show the stresses experienced by the model in the Z-direction for Time Steps 2 through 11.

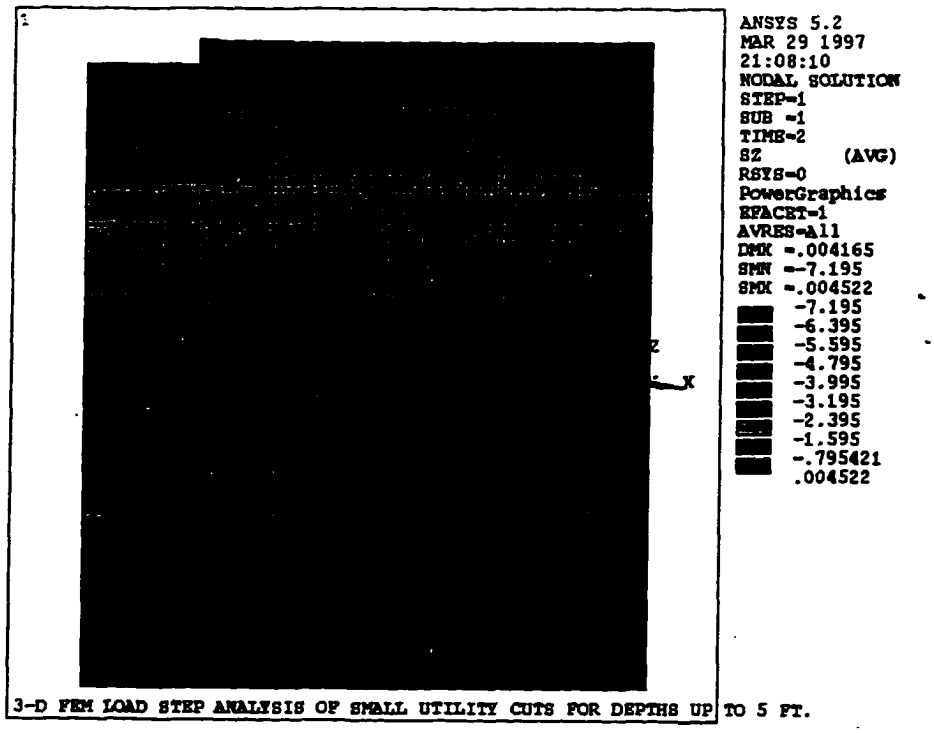

Figure 8.4(a)

Stress in the Z-direction in the FEM Model. Time Step 2. Cut Excavation 0.33 ft. Deep.

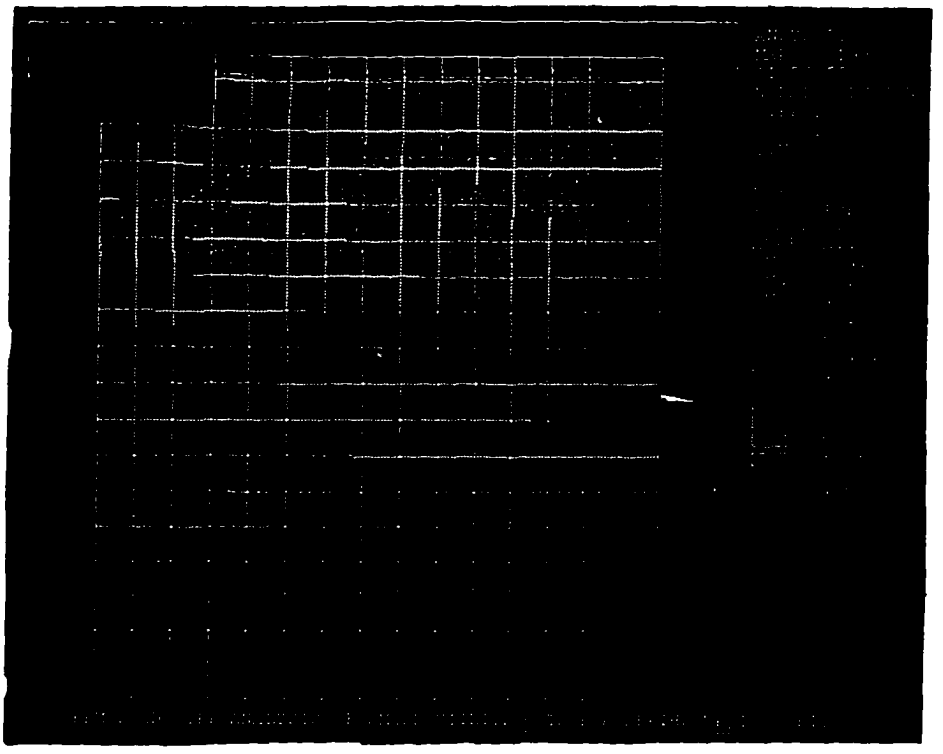

Figure 8.4(b)
Stress in the Z-direction in the FEM Model. Time Step 3. Cut Excavation 1 ft. Deep.

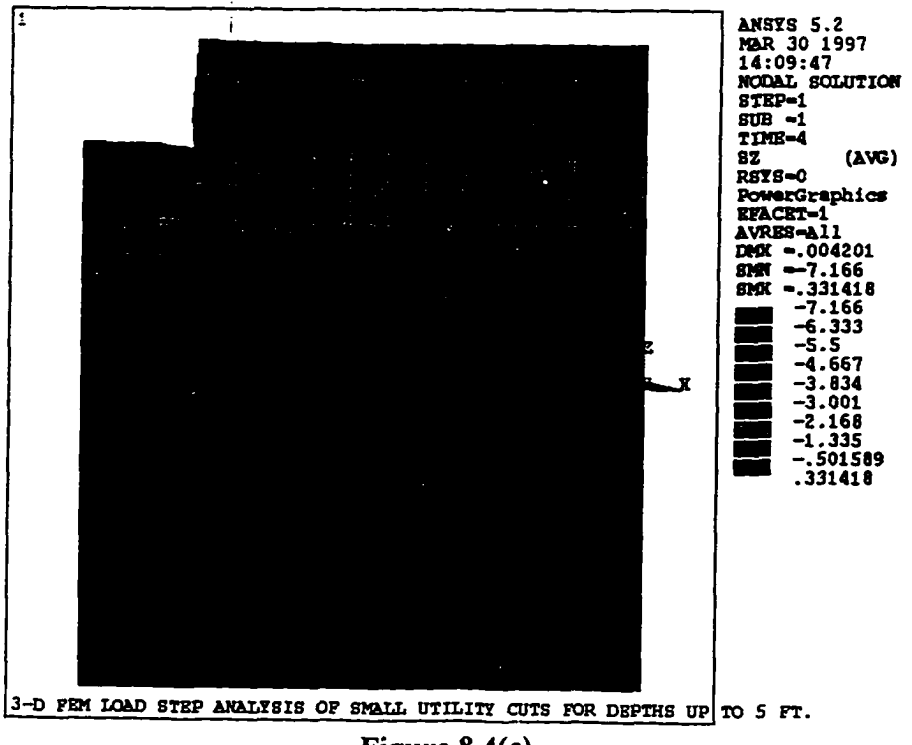

Figure 8.4(c)
Stress in the Z-direction in the FEM Model. Time Step 4. Cut Excavation 1.5 ft. Deep.

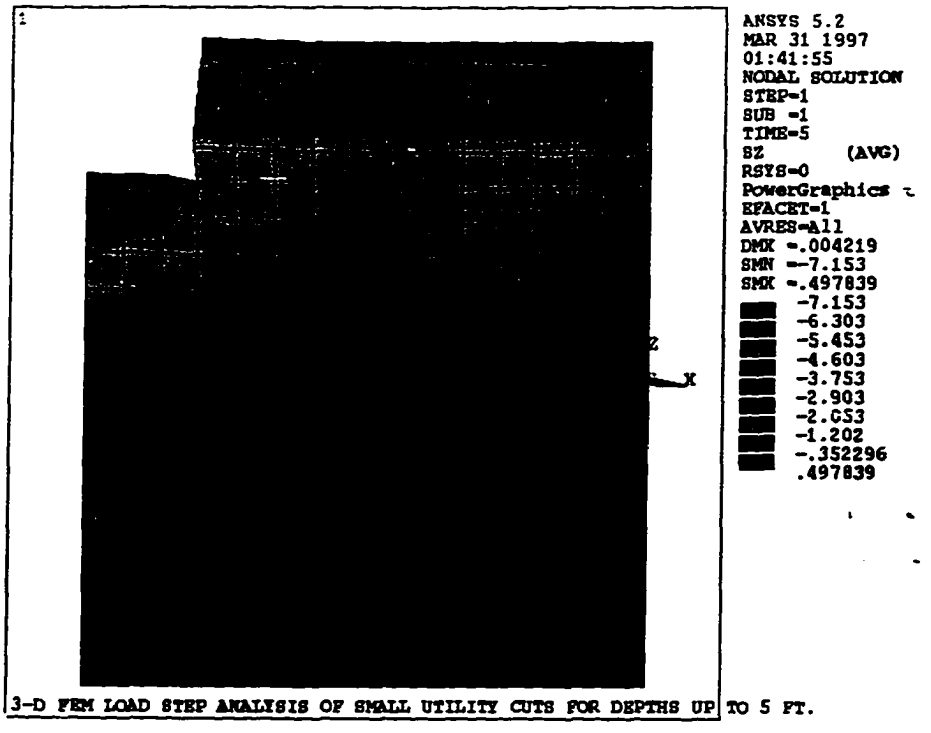

Figure 8.4(d)

Stress in the Z-direction in the FEM Model. Time Step 5. Cut Excavation 2 ft. Deep.

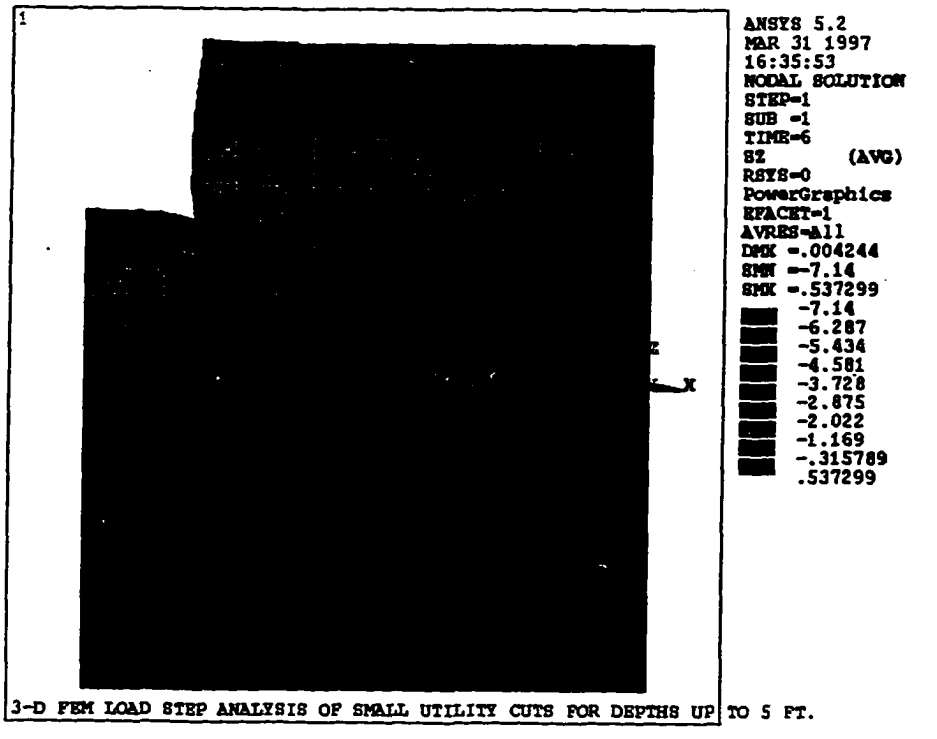

Figure 8.4(e)

Stress in the Z-direction in the FEM Model. Time Step 6. Cut Excavation 2.5 ft. Deep.

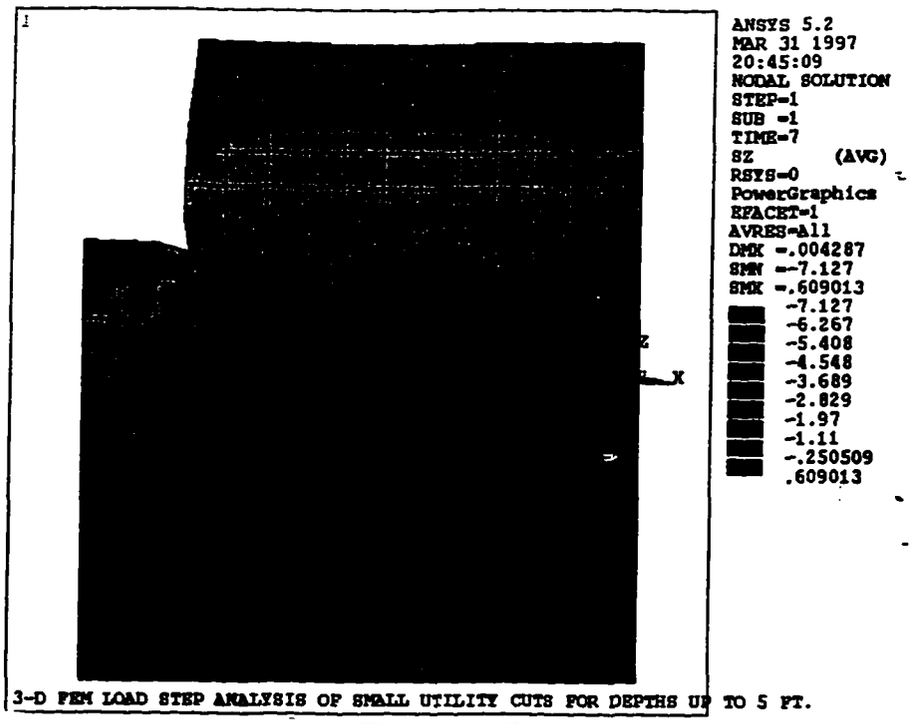

Figure 8.4(f)

Stress in the Z-direction in the FEM Model. Time Step 7. Cut Excavation 3 ft. Deep.

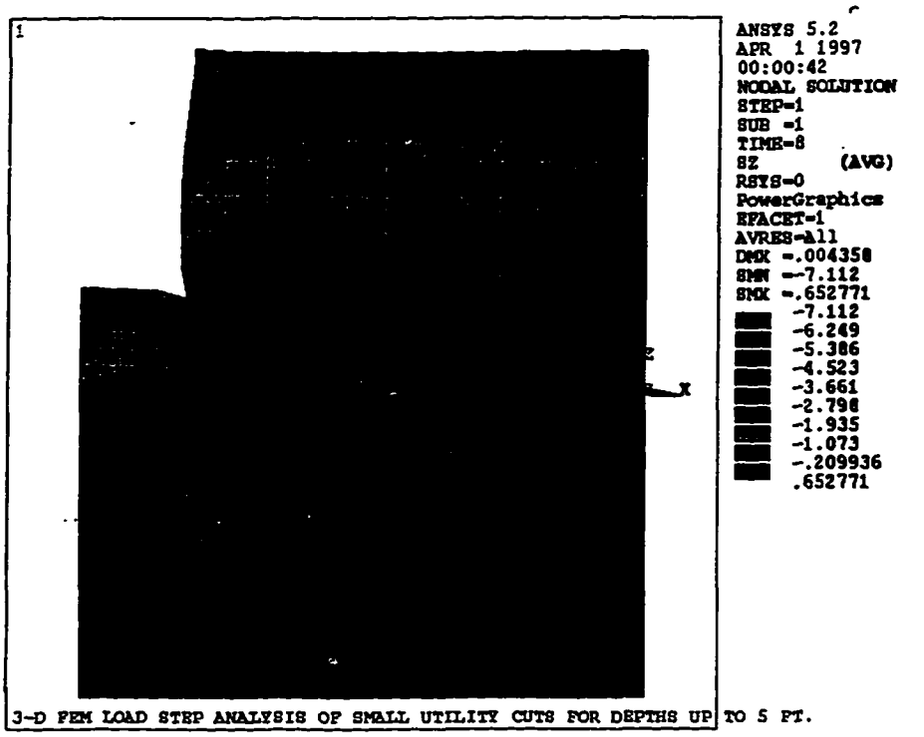

Figure 8.4(g)

Stress in the Z-direction in the FEM Model. Time Step 8. Cut Excavation 3.5 ft. Deep.

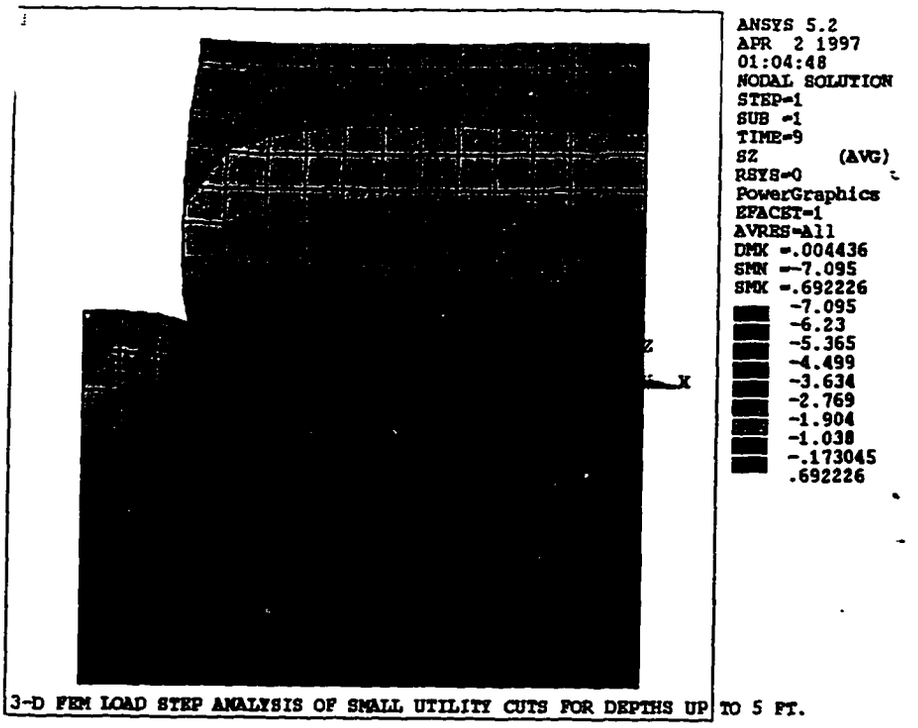

Figure 8.4(h)
Stress in the Z-direction in the FEM Model. Time Step 9. Cut Excavation 4 ft. Deep.

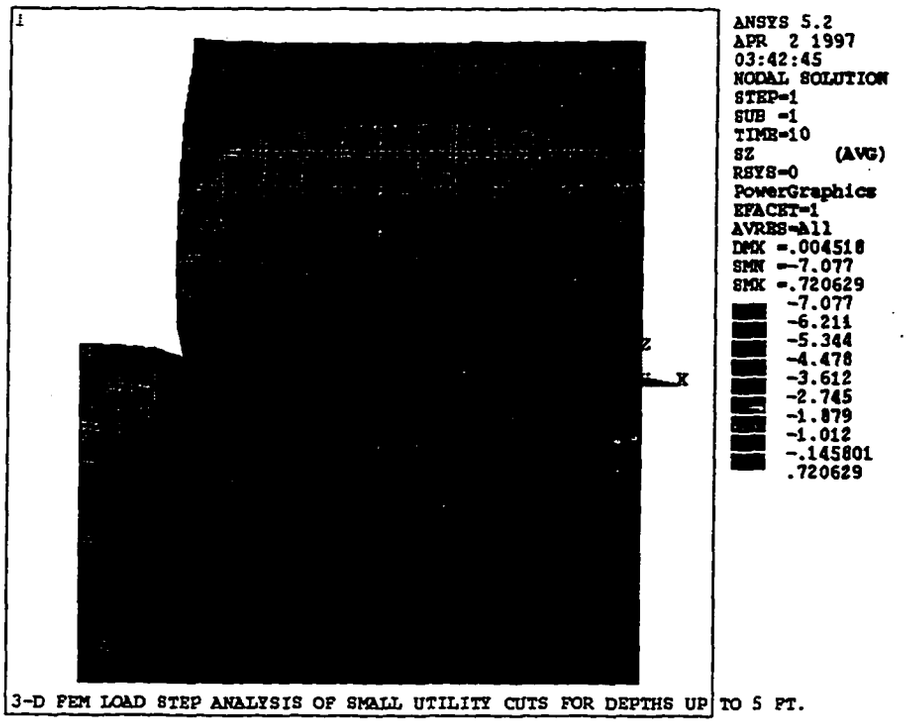

Figure 8.4(i)
Stress in the Z-direction in the FEM Model. Time Step 10. Cut Excavation 4.5 ft. Deep.

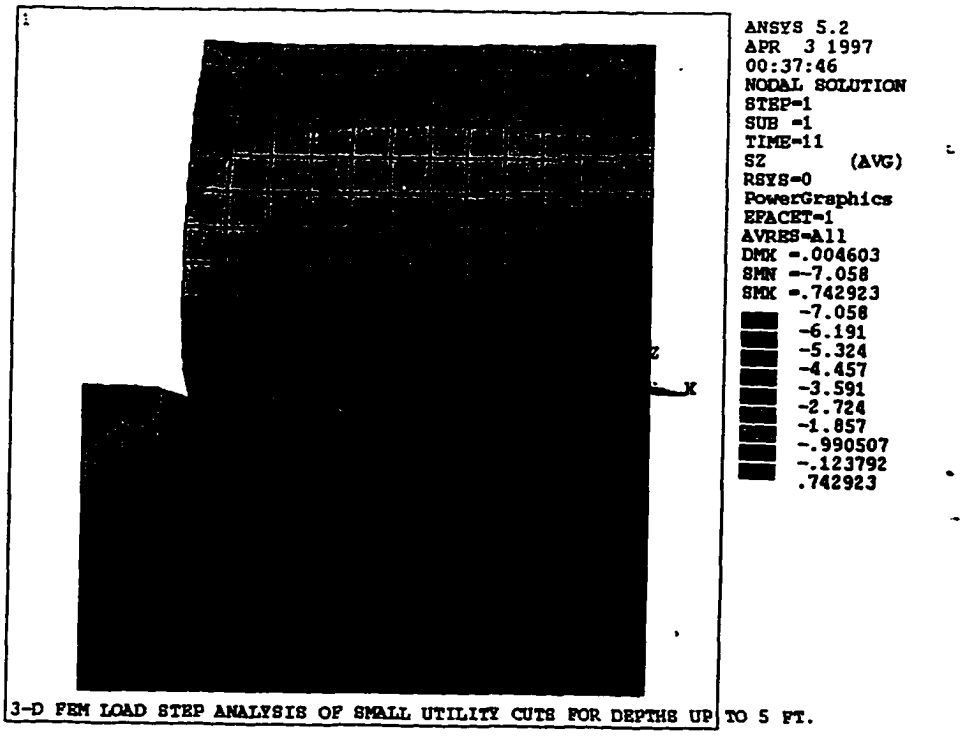

Figure 8.4(j)
Stress in the Z-direction in the FEM Model. Time Step 11. Cut Excavation 5 ft. Deep.

Figures 8.5(a) to (j) show the total strains experienced by the model in the X-direction (EPTOX), from depth 0.33 feet to depth 5 feet. The results for depths 0.33 foot and 1 foot showed minute positive strains in the soil mass, first from the removal of the stiff asphaltic concrete surface material and then from the removal of the first granular base layer. These movements are believed to be the result of elastic rebounding of the material due to the removal of the initial layers. From the removal of the first fill/subgrade layer more concentrated strains were observed.

$$\text{Now, EPTO} = \text{EPEL} + \text{EPPL} + \text{EPCR} \qquad (8.1)$$

where: EPEL represents elastic strains

EPPL represents plastic strains

EPCR represents creep strains

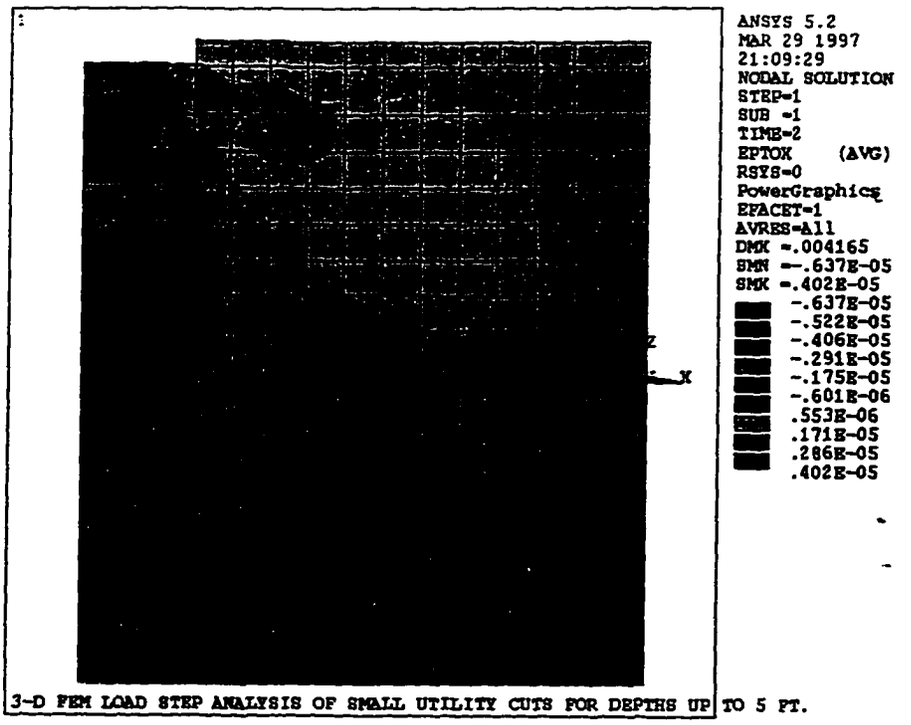

Figure 8.5(a)

Strain in the X-direction in the FEM Model. Time Step 2. Cut Excavation 0.33 ft. Deep.

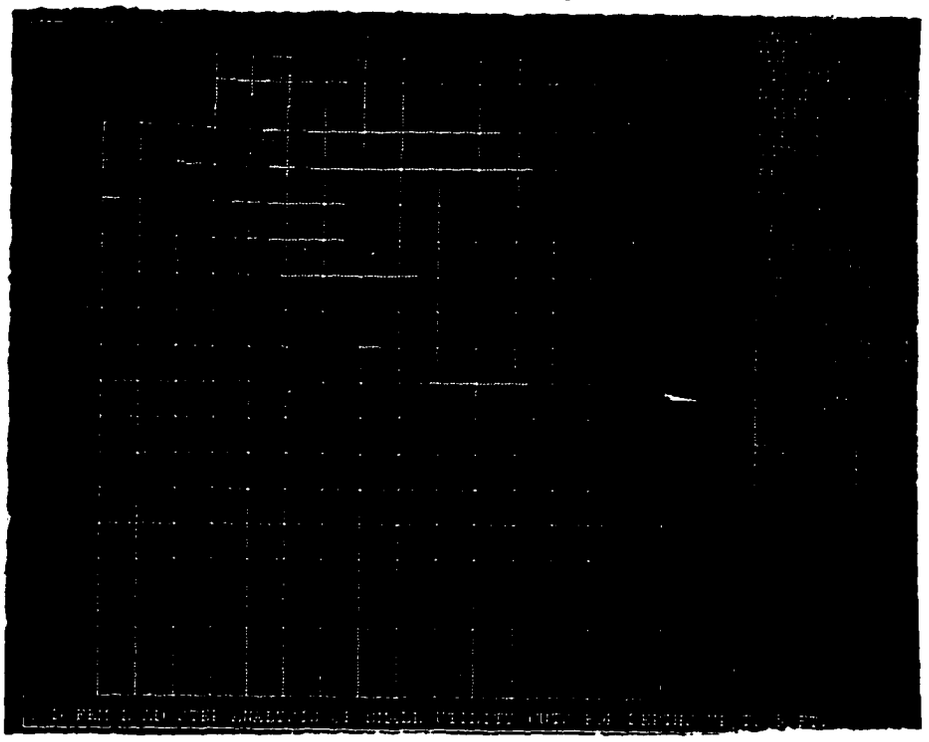

Figure 8.5(b)

Strain in the X-direction in the FEM Model. Time Step 3. Cut Excavation 1 ft. Deep.

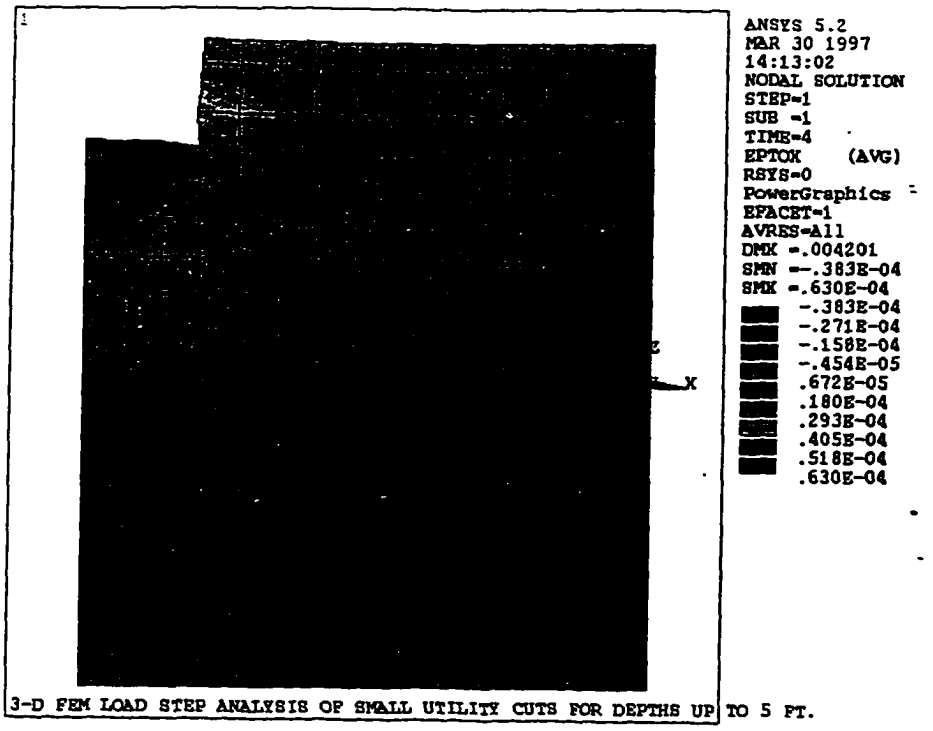

Figure 8.5(c)

Strain in the X-direction in the FEM Model. Time Step 4. Cut Excavation 1.5 ft. Deep.

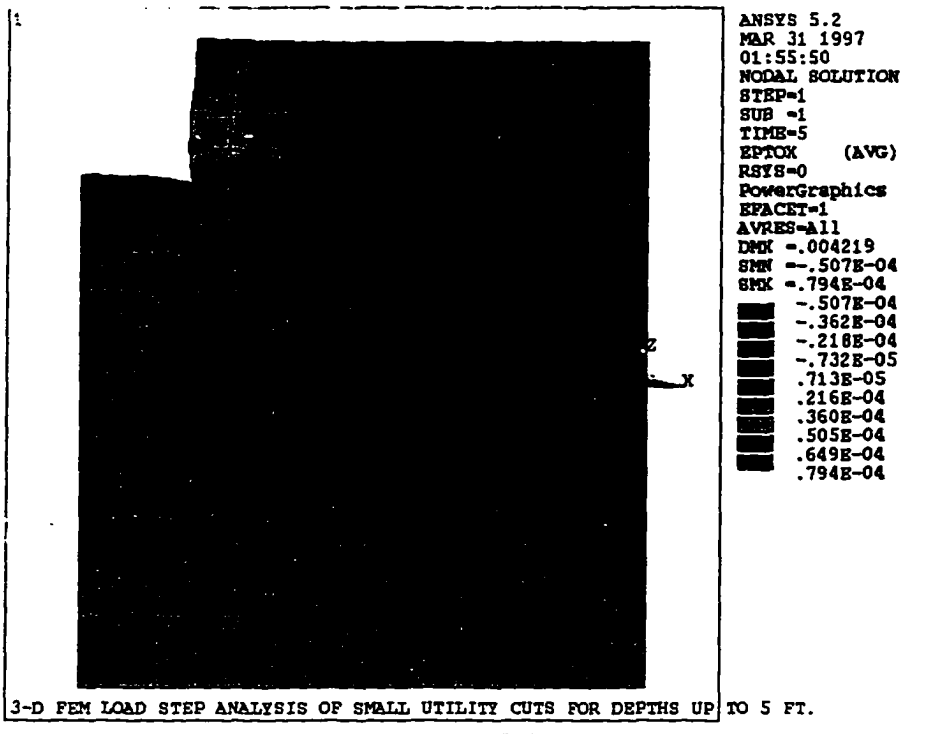

Figure 8.5(d)

Strain in the X-direction in the FEM Model. Time Step 5. Cut Excavation 2 ft. Deep.

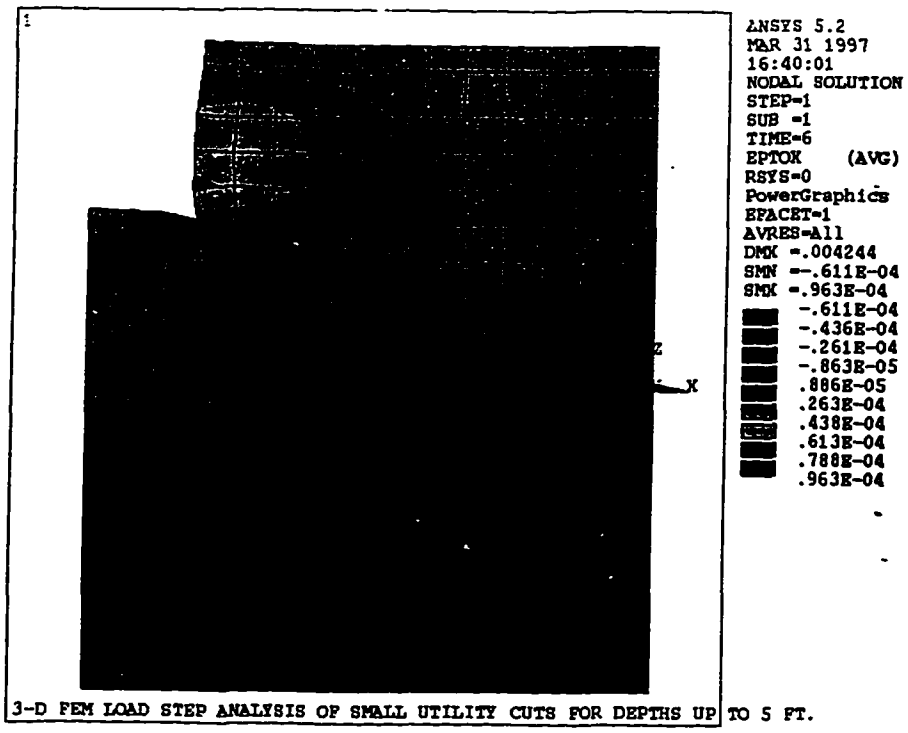

Figure 8.5(e)

Strain in the X-direction in the FEM Model. Time Step 6. Cut Excavation 2.5 ft. Deep.

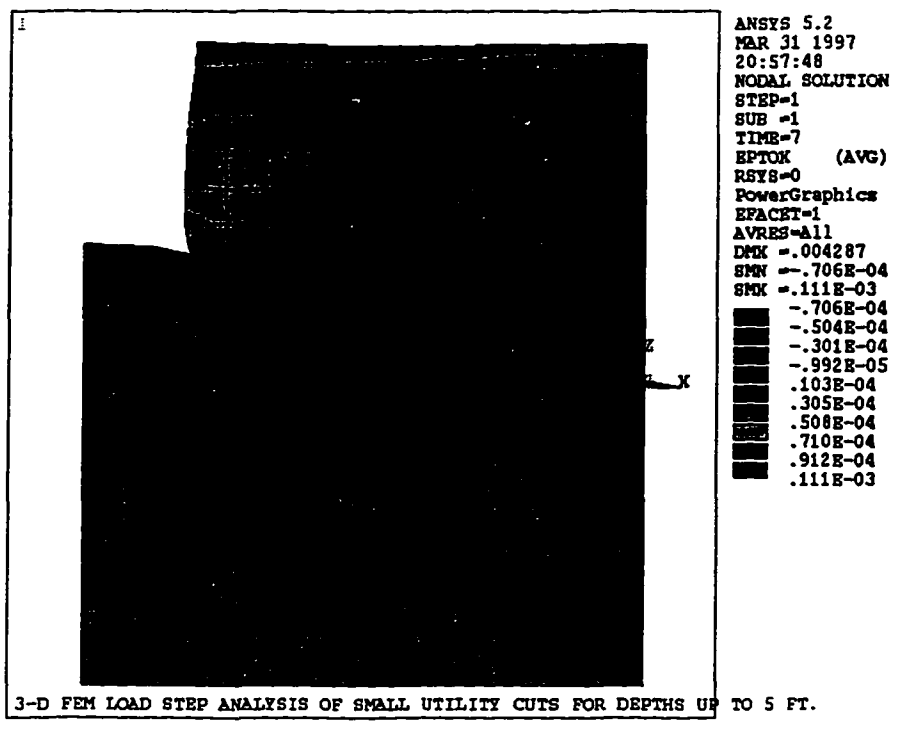

Figure 8.5(f)

Strain in the X-direction in the FEM Model. Time Step 7. Cut Excavation 3 ft. Deep.

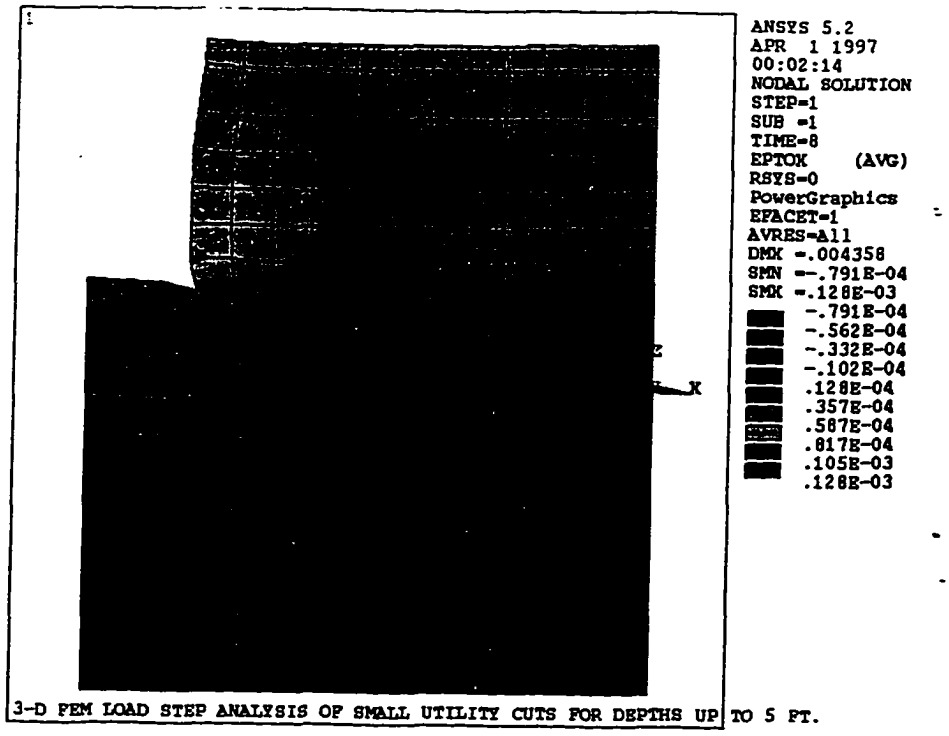

Figure 8.5(g)
Strain in the X-direction in the FEM Model. Time Step 8. Cut Excavation 3.5 ft. Deep.

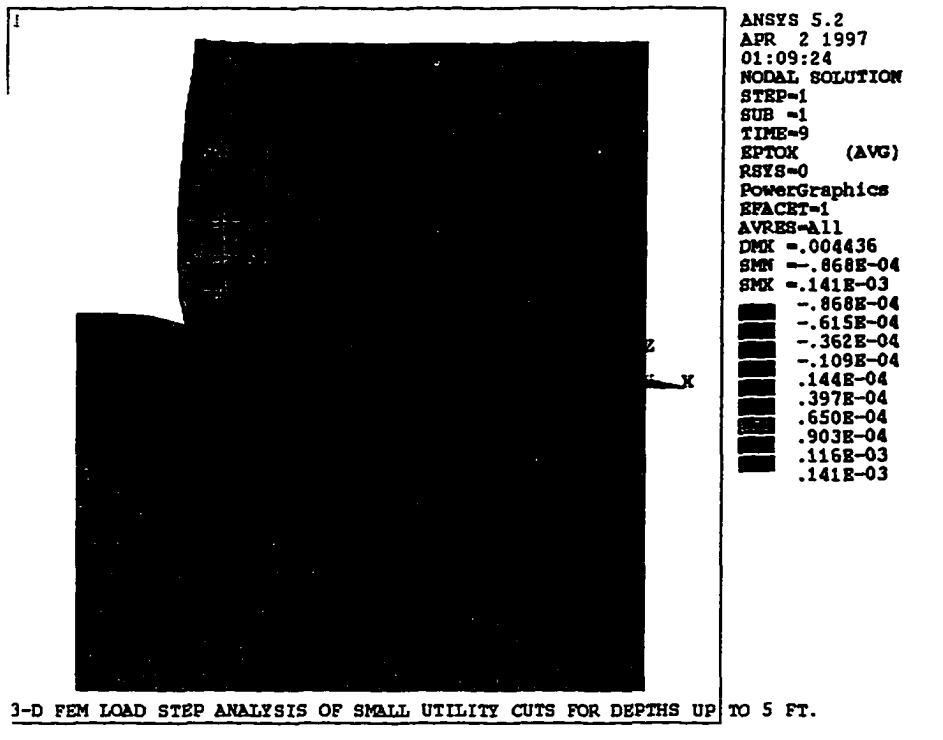

Figure 8.5(h)
Strain in the X-direction in the FEM Model. Time Step 9. Cut Excavation 4 ft. Deep.

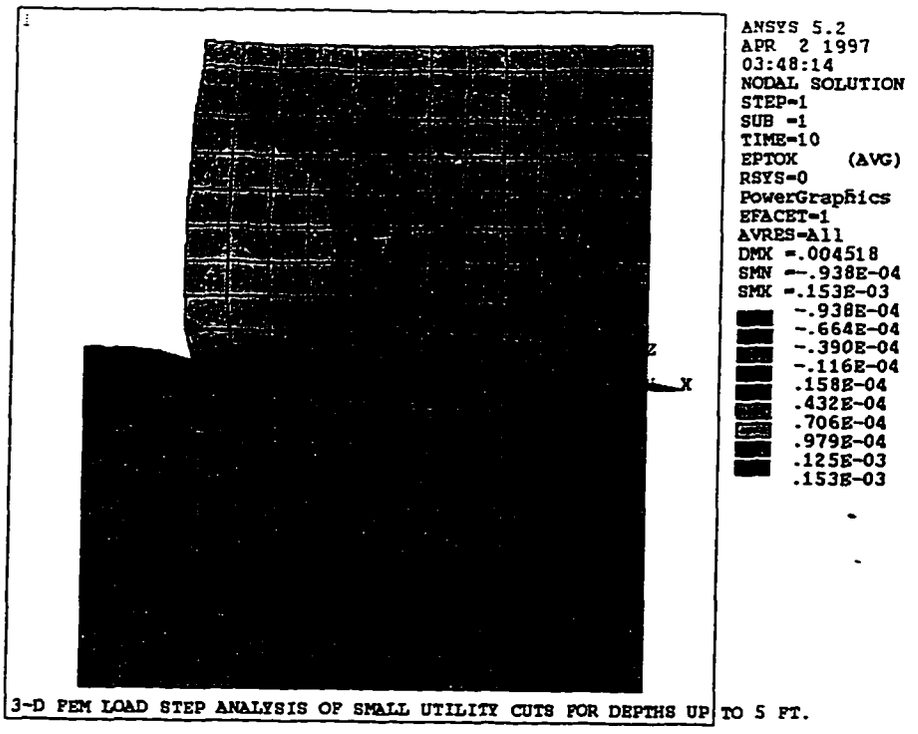

Figure 8.5(i)

Strain in the X-direction in the FEM Model. Time Step 10. Cut Excavation 4.5 ft. Deep.

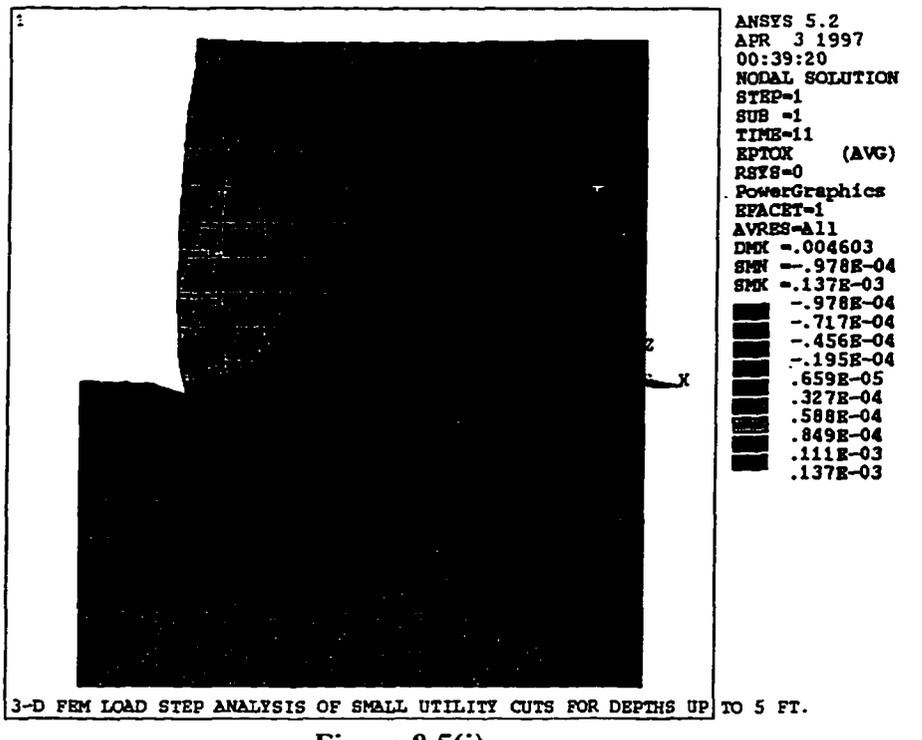

Figure 8.5(j)

Strain in the X-direction in the FEM Model. Time Step 11. Cut Excavation 5 ft. Deep.

For each step of the analysis, Figure 8.5 shows, through measurable positive strains, that soil stretching extends a distance of 2 feet from the face of the cut for the 1.5 feet deep cut and a distance of 3.25 feet for the 3 feet deep. It was also observed that soil stretching extends a distance of 3.25 feet for the 3.5 feet deep cut and a distance of 3.5 feet in the 4 feet, 4.5 feet and 5 feet deep cuts. The graphical results in Figure 5.5(j) show that the outer limits of the positive strain and its transition to a negative strain extends out to 5.5 feet. However, by accessing the total strain (elastic, plastic and creep) results and examining the rate of change of the strain, it was found that the stretching zone extended out to a distance of 3.5 feet. See Table 8.3 for the results of the analysis of strain for depths 3 feet to 5 feet.

Table 8.3

Distress impacts from Stress Relief Analytical Approach, for Comparison with Table 8.1

3 Feet Deep Cut (Stress Relief Approach)

Node	Model Width (ft.)	Displacement (in.)	Diff. (in.)	Diff. of Diff (in.)	Strain (in.)	Diff. (in.)	Diff. of Diff. (in.)	Limit of Stretch Zone
1504	0	-0.001440			0.000091			
1505	0.50	-0.000938	-0.000502		0.000061	0.000030		
1506	1.00	-0.000691	-0.000248	-0.000254	0.000037	0.000024	0.000006	
1507	1.50	-0.000496	-0.000194	-0.000054	0.000026	0.000010	0.000013	
1508	2.00	-0.000366	-0.000131	-0.000063	0.000019	0.000008	0.000003	
1509	2.50	-0.000268	-0.000097	-0.000033	0.000014	0.000005	0.000003	
1510	3.00	-0.000195	-0.000073	-0.000024	0.000011	0.000003	0.000001	3.25 feet
1511	3.50	-0.000139	-0.000057	-0.000016	0.000008	0.000002	0.000001	
1512	4.00	-0.000094	-0.000044	-0.000012	0.000007	0.000002	0.000001	
1513	4.50	-0.000060	-0.000035	-0.000010	0.000005	0.000001	0.000000	
1514	5.00	-0.000033	-0.000027	-0.000008	0.000004	0.000001	0.000000	
1515	6.00	0.000000	-0.000033	0.000006	0.000002	0.000002	-0.000001	

3.5 Feet Deep Cut (Stress Relief Approach)

Node	Model Width (ft.)	Displacement (in.)	Diff. (in.)	Diff. of Diff (in.)	Strain (in.)	Diff. (in.)	Diff. of Diff. (in.)	Limit of Stretch Zone
1804	0	-0.001647			0.000101			
1805	0.50	-0.001076	-0.000571		0.000065	0.000036		
1806	1.00	-0.000804	-0.000272	-0.000299	0.000041	0.000024	0.000011	
1807	1.50	-0.000588	-0.000216	-0.000056	0.000029	0.000011	0.000013	
1808	2.00	-0.000441	-0.000146	-0.000070	0.000021	0.000008	0.000003	
1809	2.50	-0.000329	-0.000112	-0.000035	0.000016	0.000005	0.000003	
1810	3.00	-0.000244	-0.000085	-0.000026	0.000013	0.000004	0.000002	
1811	3.50	-0.000176	-0.000068	-0.000017	0.000010	0.000003	0.000001	3.25 ft.
1812	4.00	-0.000122	-0.000054	-0.000014	0.000008	0.000002	0.000001	
1813	4.50	-0.000078	-0.000044	-0.000010	0.000007	0.000002	0.000000	
1814	5.00	-0.000043	-0.000035	-0.000009	0.000005	0.000001	0.000000	
1815	6.00	0.000000	-0.000043	0.000008	0.000002	0.000003	-0.000001	

4 Feet Deep Cut (Stress Relief Approach)

Node	Model Width (ft.)	Displacement (in.)	Diff. (in.)	Diff. of Diff (in.)	Strain (in.)	Diff. (in.)	Diff. of Diff. (in.)	Limit of Stretch Zone
2104	0.00	-0.001833			0.000112			
2105	0.50	-0.001197	-0.000636		0.000072	0.000040		
2106	1.00	-0.000901	-0.000296	-0.000340	0.000044	0.000028	0.000012	
2107	1.50	-0.000666	-0.000234	-0.000061	0.000032	0.000012	0.000016	
2108	2.00	-0.000506	-0.000161	-0.000074	0.000023	0.000009	0.000003	
2109	2.50	-0.000382	-0.000123	-0.000037	0.000018	0.000005	0.000003	
2110	3.00	-0.000287	-0.000096	-0.000028	0.000014	0.000004	0.000002	
2111	3.50	-0.000209	-0.000077	-0.000018	0.000012	0.000003	0.000001	3.5 feet
2112	4.00	-0.000146	-0.000063	-0.000014	0.000010	0.000002	0.000001	
2113	4.50	-0.000094	-0.000052	-0.000011	0.000008	0.000002	0.000000	
2114	5.00	-0.000052	-0.000042	-0.000010	0.000006	0.000002	0.000000	
2115	6.00	0.000000	-0.000052	0.000010	0.000003	0.000003	-0.000002	

4.5 Feet Deep Cut (Stress Relief Approach)

Node	Model Width (ft.)	Displacement (in.)	Diff. (in.)	Diff. of Diff (in.)	Strain (in.)	Diff. (in.)	Diff. of Diff. (in.)	Limit of Stretch Zone
2404	0	-0.002001			0.000123			
2405	0.50	-0.001306	-0.000695		0.000078	0.000044		
2406	1.00	-0.000988	-0.000318	-0.000377	0.000047	0.000031	0.000013	
2407	1.50	-0.000735	-0.000252	-0.000066	0.000034	0.000013	0.000018	
2408	2.00	-0.000562	-0.000173	-0.000079	0.000025	0.000009	0.000004	
2409	2.50	-0.000428	-0.000134	-0.000040	0.000020	0.000006	0.000004	
2410	3.00	-0.000324	-0.000105	-0.000029	0.000016	0.000004	0.000002	
2411	3.50	-0.000238	-0.000086	-0.000019	0.000013	0.000003	0.000001	3.5 feet
2412	4.00	-0.000167	-0.000071	-0.000015	0.000011	0.000002	0.000001	
2413	4.50	-0.000108	-0.000059	-0.000012	0.000009	0.000002	0.000000	
2414	5.00	-0.000060	-0.000048	-0.000011	0.000007	0.000002	0.000000	
2415	6.00	0.000000	-0.000060	0.000012	0.000003	0.000004	-0.000002	

5 Feet Deep Cut (Stress Relief Approach)

Node	Model Width (ft.)	Displacement (in.)	Diff. (in.)	Diff. of Diff (in.)	Strain (in.)	Diff. (in.)	Diff. of Diff. (in.)	Limit of Stretch Zone
2704	0	-0.002155			0.000132			
2705	0.50	-0.001406	-0.000749		0.000084	0.000048		
2706	1.00	-0.001066	-0.000339	-0.000410	0.000050	0.000034	0.000014	
2707	1.50	-0.000797	-0.000269	-0.000070	0.000037	0.000014	0.000020	
2708	2.00	-0.000612	-0.000185	-0.000084	0.000027	0.000010	0.000004	
2709	2.50	-0.000469	-0.000143	-0.000042	0.000021	0.000006	0.000004	
2710	3.00	-0.000356	-0.000113	-0.000030	0.000017	0.000004	0.000002	
2711	3.50	-0.000264	-0.000093	-0.000020	0.000014	0.000003	0.000001	3.5 feet
2712	4.00	-0.000186	-0.000077	-0.000015	0.000012	0.000002	0.000001	
2713	4.50	-0.000121	-0.000065	-0.000012	0.000010	0.000002	0.000000	
2714	5.00	-0.000068	-0.000053	-0.000012	0.000008	0.000002	0.000000	
2715	6.00	0.000000	-0.000068	0.000014	0.000004	0.000004	-0.000002	

In support of the results in Figure 8.5 and Table 8.3, Figures 8.6(a) to (e) show the measurable negative nodal soil displacements (inches) towards the cut, in the X-direction. These results provide a clearer picture of the extent of the stretching zone around the cut, for utility cuts varying between depths 3 feet to 5 feet. (A minimum cover of approximately 30 inches is used over utilities located under city street pavements, with a minimum cut depth of approximately 36 inches. The OSHA maximum unsupported depth of excavation is 5 feet). The legend in Figures 8.5(a) to (e) is described in terms of positive displacements. The maximum negative displacement in the X-direction, occurring at the face of the cut is described as the minimum displacement (SMN), and the small positive displacement occurring beyond the stretching zone is described as the maximum displacement (SMX). The shading indicated the variability in the nodal displacements.

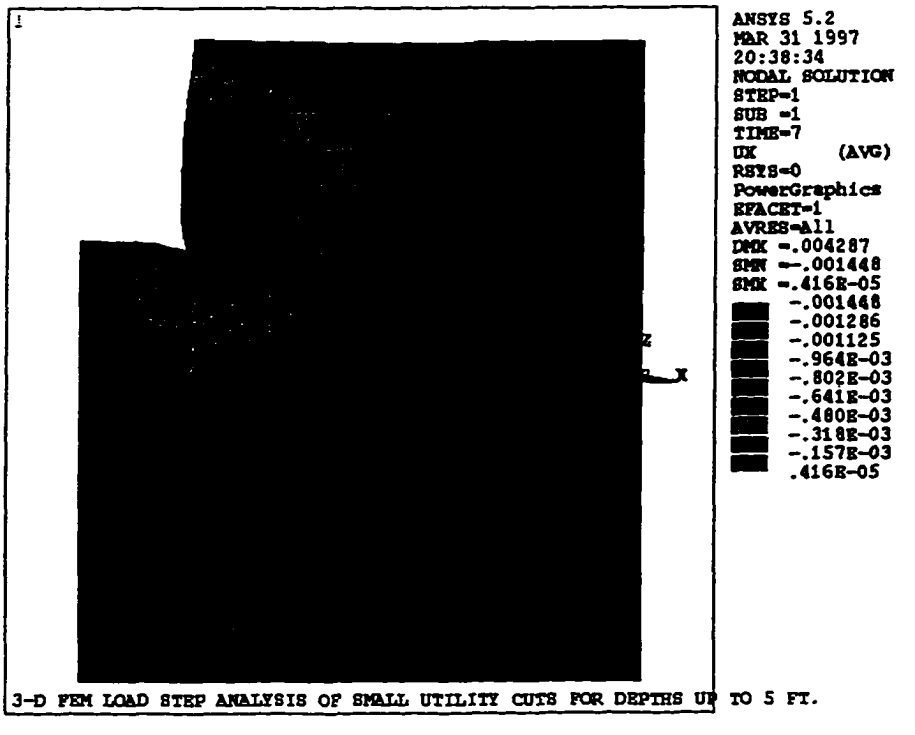

Figure 8.6(a)
Nodal Displacements in the X-direction in the FEM Model. Time Step 7. Cut Excavation 3 ft. Deep.

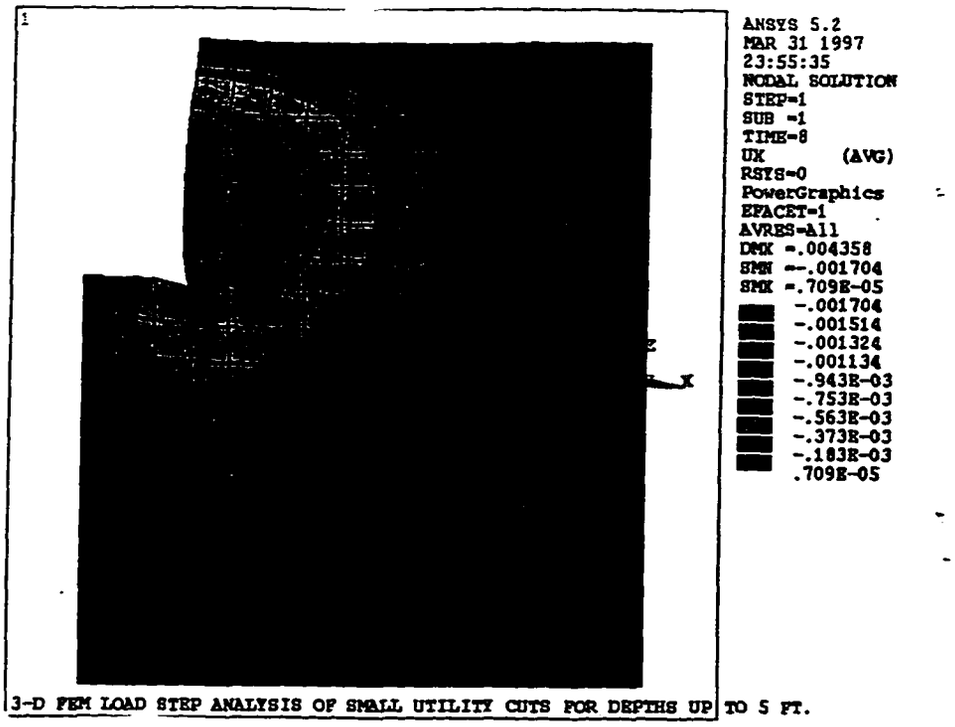

Figure 8.6(b)

Nodal Displacements in the X-direction in the FEM Model. Time Step 8. Cut Excavation 3.5 ft. Deep.

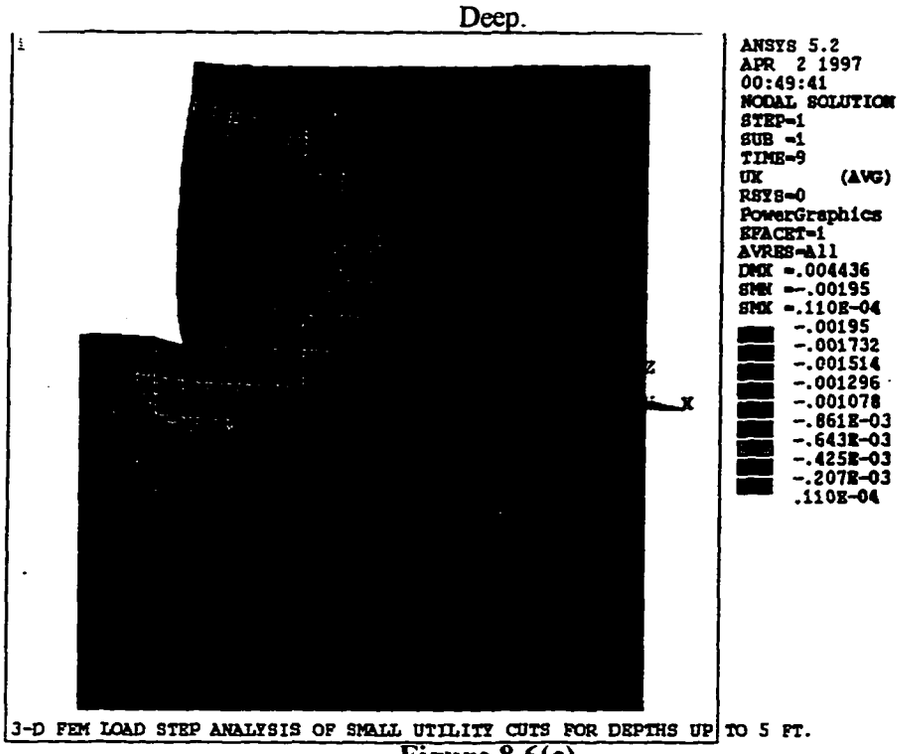

Figure 8.6(c)

Nodal Displacements in the X-direction in the FEM Model. Time Step 9. Cut Excavation 4 ft. Deep.

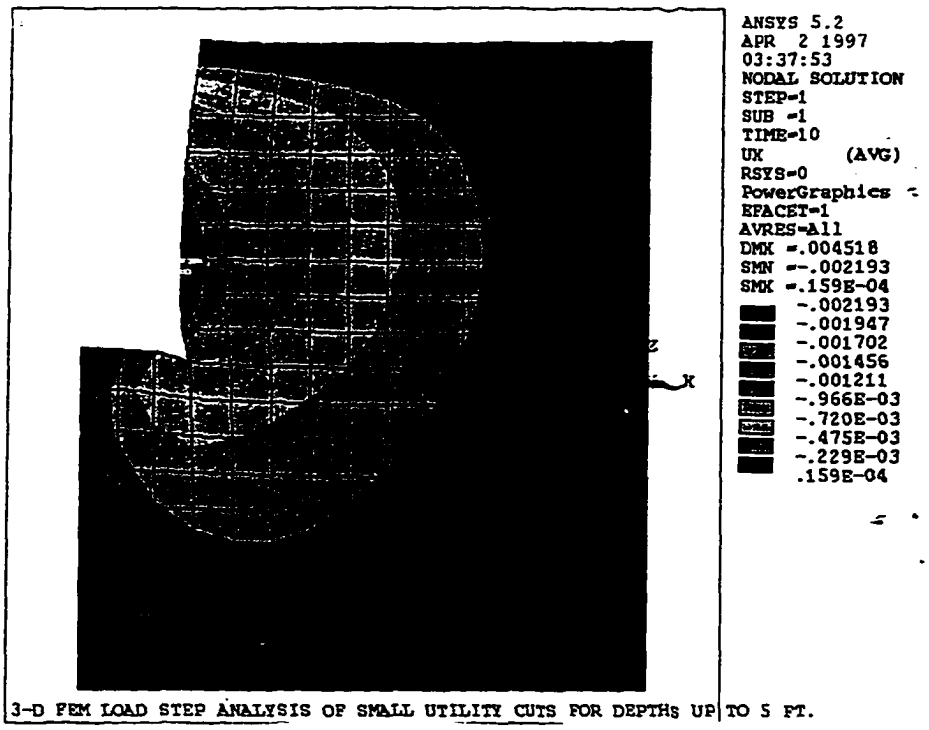

Figure 8.6(d)

Nodal Displacements in the X-direction in the FEM Model. Time Step 10. Cut Excavation 4.5 ft. Deep.

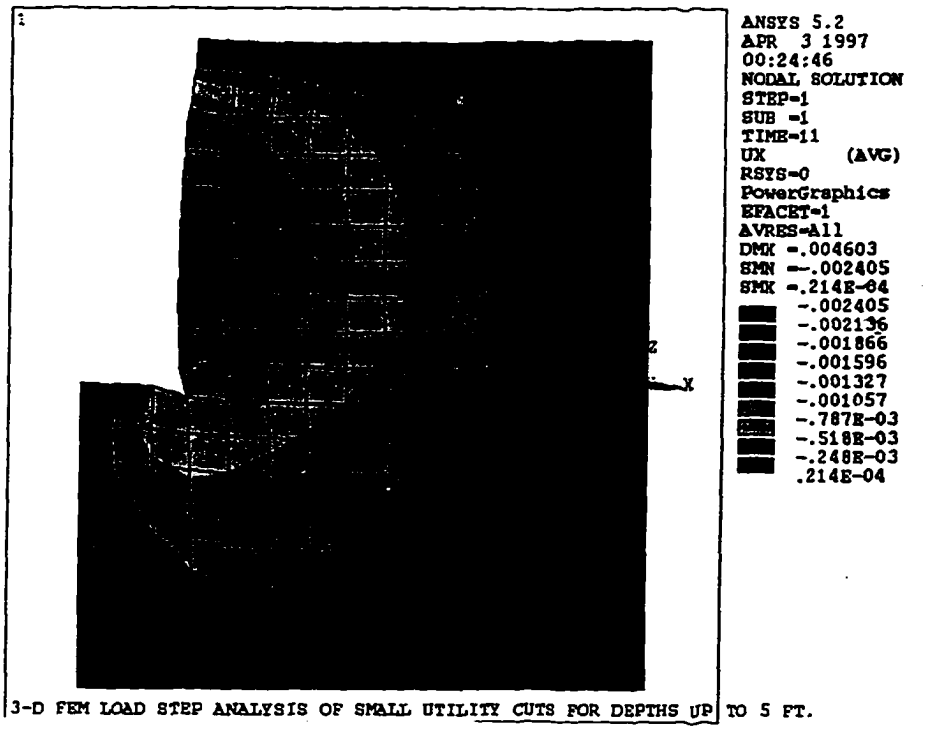

Figure 8.6(e)

Nodal Displacements in the X-direction in the FEM Model. Time Step 11. Cut Excavation 5 ft. Deep.

Figures 8.2, 8.3, 8.4, and 8.5 show the distress below the floor of the cut, reflective of the stress relief from material excavation, and modulus changes in the material below the floor of the cut. The reader should also note that the material heave of the granular portion of the model and the compression in the base course caused arching-up of the asphaltic concrete layer, (determined also in the worst case analyses), thereby putting the bottom of the asphaltic concrete in tension and the top in compression. Note also, that in the attachment of the asphaltic concrete to the restrained plane, the material demonstrated stiffening and restraining properties at the surface of the asphaltic concrete, bounded by nodes #15 through node #295. The material demonstrated tension in this area as the asphaltic concrete sought to prevent the soil mass from moving towards the cut.

Figure 8.7 shows the maximum displacement of the face of the utility cut, increasing with depth of excavation. Observation of the plot shows that for depths 4 to 5 feet the maximum displacement occurs at a location 1.5 feet above the floor of the cut. For depths 3 to 3.5 feet the maximum displacement occurs at a distance of 1 foot above the floor of the cut. For depths 1.5 to 2.5 feet, the maximum displacement occurs 0.5 foot above the floor of the cut. The Time Step 2 & 3 curves show negative displacements at the surface of the asphaltic concrete, because of the material curling up from granular material heave as well as compression in the base. The plot shows that displacements, particularly beyond the 3.0 feet deep cuts appear to be stable at depth 8 feet below the surface of the model.

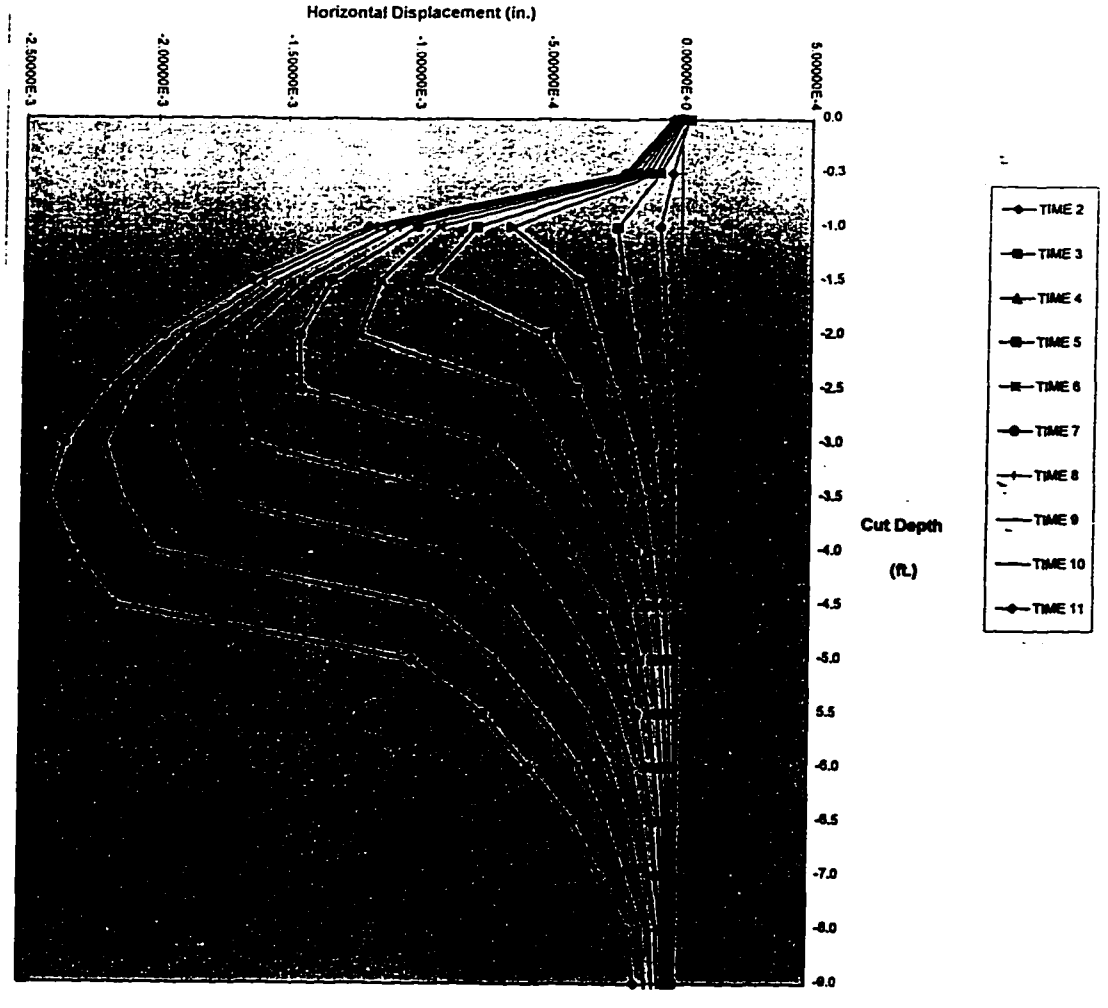

Figure 8.7

Plot of Max. Face Displacements Through Progressive Excavation. Time Steps 2 to 11

A comparison was made between the worst case approach and the stress relief approach for the determination of the impacts of utility cuts in urban street pavements. Table 8.4 shows the close similarities in distress impacts from Table 8.1 for the worst case approach and Table 8.3 for the stress relief approach.

Table 8.4
Comparison of Stretching Impacts between the Worst Case Analysis and the Stress Relief Analyses of Small Utility Cut excavations

	ANALYTICAL APPROACH	
	Worst Case	Stress Relief
Cut Depth (ft.)	Stretch Impacts	Stretch Impacts
3	3	3.25
3.5	3	3.25
4	3.5	3.5
4.5	3.5	3.5
5	3	3.5

As a recap, the worst case approach analyzed a model which had a depth, restricted to the depth of the utility cut and free to move on the plane located at the bottom of the cut. The load application of this model was via geostatic nodal forces applied to the back wall of the soil mass, surrounding the unsupported cut face. (See Figure 7.1 for the location of the back wall). The width of the model, from the face of the cut to the back wall, was determined from applying the Harris and O'Rourke 1983 inverse sine function shown in Table 4.7. In addition, the model was analyzed, assuming that the excavation was already completed.

In the case of the stress relief approach, a soil mass that would give a 4 feet depth of soil below the 5 feet deep utility cut was used. The width of the model was determined from the required width of cut for the 5 feet deep cut in Table 4.7 plus 6 inches. Gravity loading was applied to the model. The stress relief analysis was done on the model, using a load step approach, with a simulated excavation by predetermined layers removal, explained above.

Analytical time for the two approaches, using the now enhanced ANSYS 5.2 version with the power solver and power graphics may be similar. Analyses done earlier on the worst case model used versions 5.0 and 5.1 which were extremely slow and took several hours to complete an analysis. (Approximately 6 hours for the 5 feet deep utility cut). Using the stress relief approach with ANSYS version 5.2 solutions were obtained in 45 minutes for each analysis. It took approximately two hours after each analysis to process the information, extract results and outputs and modify the E-values for affected elements to conduct the next load step analysis.

However, the worst case approach will require greater input time as each of the respective models for the various depths have to be built, material properties and loads applied. On the other hand, for the stress relief approach the model of the soil mass (before excavation) is built, material properties and gravity loading applied. Successive excavation simulation was achieved by killing layer elements and impacted elements had their E-values modified for the next load step analysis. The stress relief models did not have to be rebuilt but to obtain previous information from earlier load steps would require conducting the analysis from the top. Hence, a backup file of the first analysis must be made by the analyst to ensure a capability to redo the step analyses.

CHAPTER IX

SUMMARY, CONCLUSION AND RECOMMENDATIONS

Summary

The first phase of the research analyzed twenty seven worst case models to determine the impacts of small utility cuts in urban street pavements. The worst case analysis assumed that the excavation was completed to the required depth and due to geostatic thrust and the spreading effects of the overburden pressure, the model was free to move towards the cut, along the horizontal plane, located at the bottom of the model (cut depth).

The second phase of the analysis pursued a stress relief approach. Eleven stress relief models were analyzed via a time step approach to simulate the excavation process in the field. A 9 feet deep half space of the pavement was used and the excavation process for a small utility cut of unsupported depths of up to 5 feet was allowed to take place. (OSHA Specifications indicated that unsupported excavations should not exceed a 5 feet depth). It was assumed in this analysis that some portion of the soil beneath the floor of the cut acted conjointly with the soil mass surrounding the utility cut, to provide some stability to the soil mass surrounding the utility cut. The stress relief models used a minimum soil mass of 4 feet below the floor of the utility cut during the analysis. The original half space of the pavement structure was modeled, gravity loading applied and by graduated excavation, load step analyses performed to determine the impacts of the utility cut excavation, on the surrounding pavement materials. See Figures 7.2 and 7.3.

The stress relief approach allowed for the utilization of the reduced average effective soil stresses, which resulted from the removal of the overburden pressure, during the excavation process. These impacted stresses were used to re-compile the E-values in the sub floor layers and the adjacent wall elements, prior to the next load step analysis.

The worst case model did not compensate for soil relaxation. It used the same E-values for all elements in the respective layers and no compensation was made in the wall elements to compensate for the absence of the excavated material.

The results of the 2 phase analyses, however, produced similar distress results, which can be observed by comparing Tables 8.1, 8.3 and 8.4. Indications are, that as excavation progressed to a depth of 5 feet, a stretching zone was created in the soil mass, varying between 3.25 feet to 3.5 feet from the face of the cut, for small utility cut depths in the range of 3 to 5 feet.

The stretching zones were indicated by positive strains in the results and the strain plots for the respective depths are shown in the Figure 8.5. Table 8.3 shows the computations from the outputs, which clarifies the extent of the positive strain and the reaches of the stretching zone in Figure 8.5 for depths 3 to 5 feet. Figure 8.6 also shows the extent of the stretching zone in the plots of the negative nodal displacements, for depths 3 feet through 5 feet.

The results further indicated, that at a distance approximating the extent of the distress zone, (determined from the strain and displacement results), the pavement assumed horizontal stress profiles, indicating stable conditions in the outer limits of the model, beyond the stretching zone. (See Figure 8.3) The figure showed the development of the decreasing stress patterns in the X-direction along the face of the cut, as the time

step analysis progressed and the confining stress released from the face of the cut. Figure 8.4 showed the vertical stress impacts in the soil mass adjacent to the cut and the impacts of the release of vertical pressure on the area under the floor of the cut, as the excavation progressed. The vertical stress variations, in the region of the face of the cut were less severe than the variations in the horizontal confining stresses, because of the influence of the overburden pressure.

The results showed the evidence of compression heaving below the floor of the cut in Figure 8.2. Figures 8.3 and 8.4 indicate the horizontal and vertical stress variations below the floor of the model as the overburden pressure was reduced during soil excavation. Note that the vertical stress patterns below the floor of the model show sharper variations than the horizontal stress patterns. Figure 8.5 shows the negative X-direction strain pattern from compression in the zone below the floor of the cut. Figure 8.6 shows the displacement pattern in the X-direction, below the floor of the cut.

The analysis assumed that few natural soils are perfectly cohesionless and approached the research with the assumption that the granular materials used in road construction possessed some intrinsic cohesion value. In the analysis of the worst case models, sensitivity analyses were performed for the determination of the minimum cohesion value, to enable measurement of the surrounding distresses to the pavement structure. The Phase 1 analysis determined the minimum cohesion values required to obtain stable solutions for excavations varying between 3 to 5 feet deep and Table 8.1 summarized the results of the depth specific analyses done on the 27 worst case models.

Conclusions

Based on the research assumptions, and results of the 2-phase analyses, the following can be determined:

- Under research conditions, when the utility cut is opened in the pavement, a stretching zone is created behind the unsupported face of the utility cut, extending for distances of up to 3.5 feet into the pavement structure. This was confirmed by both the Phase 1 (worst case) and the Phase 2 (stress relief) analyses.
- The magnitude of nodal displacements in the models appeared to be a function of the soil cohesion, angle of internal friction, density and cut depth.
- The load application also was found to impact the displacement values. The 27 worst case models used the horizontal nodal geostatic thrusts against the side of the model, and demonstrated greater displacements than the gravity loaded model used in the stress relief analysis. This was believed to be due in part to the freedom given to the worst case model, allowing it to slide on a plane located at the floor of the cut. (See Table 8.1 and Figure 8.6). The magnitude of the displacements did not impact the extent of the distress zone around the utility cut and was felt to be merely relative in nature.
- Table 8.1 shows that with the increase in ϕ angle and the development of a steeper failure plane, there is a requirement to increase the cohesion in the soil to maintain plastic equilibrium and prevent failure along the steeper failure plane.
- The asphalt surface seemed to provide restraining support to the model in its state of tension, and restricted the granular portion of the model from moving towards the cut.

A look at Figure 4.2 shows the failure plane for the active Rankine state. The soil to the left of that plane is likely to experience tension cracking in this state, and it appeared from the results of the analyses, that the asphaltic concrete may have acted as a stabilizer to the model, in restraining this tension distress in the granular material.

- The research showed that the worst distress impacts to a utility cut occurred in the fill material. The Researcher is of the opinion that the distresses to the fill material in a flexible pavement will be similarly experienced by a composite pavement, if subjected to a utility cut. The effects of these distresses are easily visible in flexible pavements, however, the bridging capability of the concrete base of composite pavements, prevents the reflection of the surrounding pavement distresses. Early utility cut distresses in composite pavement are revealed through patch failure.

Recommendations

This research effort pursued **A Mechanistic Approach To Determine the Impacts of Small Utility Cuts in Urban Street pavements.** It set out to examine the pavement structure and develop theoretical explanations for the surface distresses observed by others in the vicinity of street cuts, and the extent of these distress impacts. The Researcher pursued an hypothesis that predicted the existence of a localized stretching zone around the cut. Under research conditions, the actual profile of the displacement/distress envelope of the distress zone was determined, for cut depths ranging from 3 to 5 feet, the locus of which extended for distances of up to 3.5 feet from the face of the utility cut. It is anticipated that with this awareness of the distress patterns in the pavement structure, a more efficient restoration methodology could be pursued by city

agencies to mitigate pavement deterioration, and an appropriate fee structure developed to cover pavement damage and restoration costs.

Benefits to be derived from the results of this research effort will include; extended pavement life, reduced maintenance and life cycle costs, smoother streets in spite of utility cut patching and reduced consumer costs.

Based on:

1. The analyses and results of this research effort, and
2. Established theory of soil mechanics, which determine the incapability of a granular fill material, subjected to vertical stress, to displace itself sufficiently laterally, to recompact the distress zone around the utility cut,

the Researcher determined that under research conditions, the following actions may be pursued and studied, as an appropriate restoration methodology, to recover pavement integrity in the vicinity of utility cuts.

- Restore the utility cut according to the construction specifications for the pavement, up to top of base elevation. This restoration provides confining conditions for the soil surrounding the cut and prevent further inward movement of the surrounding soil, and inhibit any further extension of the stretching zone from creep strain.
- Remove the asphalt surface for a square area of sides (x' + 3' + x') or (2x' + 3') to obtain a cut-back surface area of $(2x' + 3')^2$, for x' equal the maximum distance of the displacement/distress envelope, in the fill material, from the face of the utility cut. (See Figure 9.1).
- Vibro compact or roll the cut-back area to develop initial compaction stresses in the depths of the pavement structure. "Sands can sometimes be densified with rollers for a

depth of 3 to 6 feet." (Lambe and Whitman 1969, 514). After achieving the desired field compaction values, which can be determined by field density tests, the area can then be resurfaced. (See Figure 9.1). This method, though costly, will ensure the full compaction of the utility cut, and the affected area of the pavement surrounding the cut. The results of the analyses in this research indicate that the cut-back surface area will vary between 9.5' x 9.5' and 10' x 10'. The text treats the issue of compaction in depth, as well as vibro-compaction and can be consulted for further study in pursuing a restoration approach. (Terzaghi and Peck 1967, and Capper and Cassie 1976).

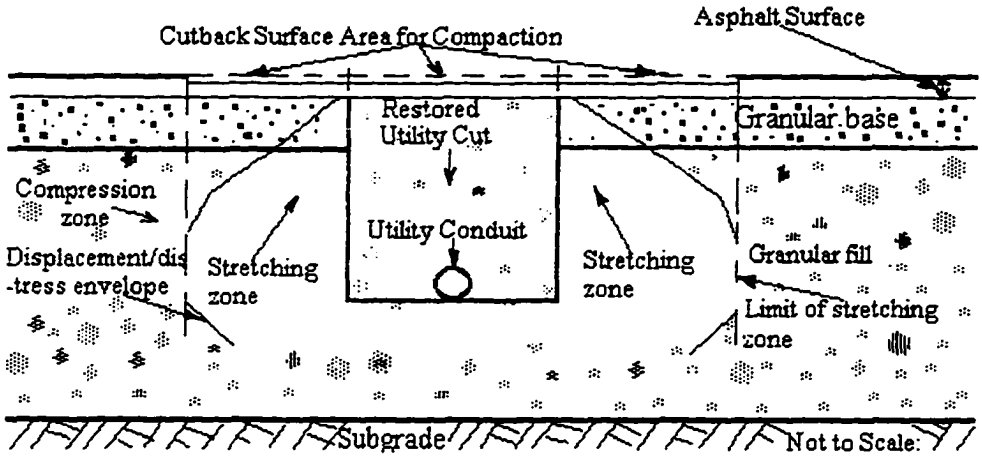

Figure 9.1
Section Through Utility Cut Showing the Recommended Extent of the Surface Cutback for Final Densification and Restoration of the Utility Cut.

Economics of the Cutback Approach to Utility Cut Restoration

A study in cutbacks and dynamic compaction, for the determination of an optimum economic solution, needs to be pursued as a follow-up to this research. Special attention will need to be paid to dynamic compaction methods in and around the vicinity of sensitive utility lines, when attempting to restore subfloor distresses.

The results from this research could be used to test various surface cutback scenarios with dynamic compaction, and the respective restoration scenarios monitored for a performance rating. Cost benefit analyses would determine the optimum cutback and dynamic compaction scenario for an empirical approach to city street restoration.

With the use of Figure 8.6 the analyst can design cutback intervals for testing a series of cuts, effect the restoration of the respective test sites, subject each site to the same load type and frequency of loading, monitor patch performance and determine the frequency of failure for each patch, (deflection of > 1/2 inch of the patch and/or the surrounding area within the limits of the compacted distress zone), required patch maintenance and related costs. These tests would determine whether a restoration with a maximum cut-back of 3.5 feet provides similar benefits as a restoration with a cut-back of lesser dimension and associated lower costs. A minimum asphaltic concrete cutback of 1 foot is recommended for the testing of these scenarios.

Other Recommended Restoration Approaches

Other recommended restoration approaches for further study may include:

1. Driving a square, steel sheet pile box of cut size into the pavement, along the proposed cut edges before excavation commences. This will rigidly confine the surrounding pavement structure, after which, excavation can commence. Restoration of the cut is achieved by controlled compaction of each lift of the restoration materials and using controlled withdrawal of the sheet pile box, as the lifts are completed in the cut. This can be a costly exercise, but may prevent the necessity for surface cutback and deep compaction. Harris and O'Rourke 1983, discussed the problem of soil strains even

with wall support, but the extent of the distress impacts may be minimized with the use of this contained excavation.

2. Freezing of the soil before excavation, to minimize soil stretching in sensitive areas, where such movements may be undesirable. This method is subject to its suitability for use in the proximity of the respective utilities.

BIBLIOGRAPHY

American Association of State Highway and Transportation Officials. AASHTO Guide for Design of Pavement Structures. Washington, D.C.: 1986.

_____. AASHTO Guide for Pavement Management Systems. 1990.

ANSYS - Engineering Analysis System, Revision 5.0A User's Manual, Vol. I Procedures, Vol. III Elements, Vol. IV Theory. 1991.

American Public Works Association Research Foundation. "Draft Utility Cut Opening and Restoration Procedures." A report prepared for discussion by the sponsors of the Recovering Costs of Pavement Cuts Research Project. August 1991.

_____. "Utility Cuts and Replacements." Street and Urban Road Maintenance, Project Number 111. (1963): 229-40.

Arizona Roads Newsletter Vol. 4 No. 4. "Non-shrink Backfill Saves Time, Money In Restoring Utility Cuts." October 1988.

Brewer, William E. "The End of the Backfill problem -Controlled Density Fill." Concrete Construction. October 1975. 448

Capper, P. Leonard., and W. Fisher Cassie. The Mechanics of Engineering Soils. New York: John Wiley & Sons, 1976.

Chang, Ching S. "Uncertainty Of One-Dimensional Consolidation Analyses." Journal of Geotechnical Engineering 111 (December 1985). 1411-24.

Chen, Wei-Fah., and D. J. Han. Plasticity for Structural Engineers. New York: Springer-Verlag, 1988.

Das, Braja M. "Principles of Soil Dynamics." Southern University at Carbondale. Boston, Massachusetts: PWS-Kent Publishing Company, 1993

Department of Water and Power, City of los Angeles. Slurry backfill Program, 1973.

Emery, John J., and Tom H Johnston. "Influence of Utility Cuts on Urban Pavement Performance." 1985.

_____. "SP 93-10 - Unshrinkable Fill for Utility Cut Restorations," 1986, 187-211.

Frederico, Antonio. "Pore Pressure Behavior of K_O-Consolidated Clays." Discussion from November, 1988 Vol. 114 by Paul W. Mayne and Harry E. Stewart (paper 22978). Journal of Geotechnical Engineering. (September 1990): 1436-41.

Grandlin, H. Jr., Fundamentals of the Finite Element Method. Prospect Heights, Illinois: Waveland Press, 1991.

Haas, Ralph, Ronald W. Hudson. Pavement Management Systems. New York: McGraw Hill, 1978.

Haas, Ralph, and Ronald W. Hudson and John Zaniewski. Modern Pavement Management. Malabar Florida: Krieger Publishing Company, 1994.

Harding, Bobby. "Crushing of Soil Particles." Journal of Geotechnical Engineering 111 (October 1985): 1177-92.

Harris, C. W., and T. D. O'Rourke. "Response of Jointed Cast Iron Pipeline to Parallel Trench Construction." Geotechnical Engineering Report 83-5. Ithaca, NY: Cornell University, March 1983.

Heine, Martha. "Pavement Opening Policy Protects City Streets." Roads and Bridges (April 1990): 36-39.

Huang, H. Yang. Pavement Analysis and Design. University of Kentucky. Englewood Cliffs, New Jersey: Prentice-Hall, 1993.

Infrastructure Institute of the University of Cincinnati. "Impacts of Utility Cuts on the Performance of City Street Pavements." 1991.

Johnson, Christine. "Pavement (Maintenance) Management Systems." American Public Works Association Research Foundation.

Kingston, William L. "Soil Cement Slurry Backfill." Department of Water and Power. City Of Los Angeles: 1973.

Lambe, T. William., and Robert V. Whitman. Soil Mechanics. Massachusetts Institute of Technology. New York: John Wiley & Sons, 1969.

Logan, D. L. A First Course in the Finite Element Method. Boston: PWS Engineering, 1986.

Lubliner, Jacob. Plasticity Theory. University of California at Berkley. New York: Macmillan Publishing Company, 1990.

Mangolds, A., and J. Carapezza. "Assessment of Pavement Cutback requirements." Produced for Brooklyn Union Gas and Consolidated Edison Co. New York: Foster-Miller, January 1991.

Mayne, Paul W. "Dilatometer Testing On Highly Overconsolidated Soils." Discussion on May 1987, Vol. 113, No. 5 by Alireza Boghrat (Paper 21453). Journal of Geotechnical Engineering 114 (December 1988): 1462-65.

_____. "Determining OCR In Clays From Laboratory Strength." Journal of Geotechnical Engineering 114 (January 1988): 76-92.

Mayne, Paul W., and Harry E. Stewart. "Pore Pressure Behavior of K_O-Consolidated Clays." Journal of Geotechnical Engineering 114 (November 1988): 1340-46.

Metropolitan Toronto Roads and Traffic Department. "Utility Cut Restoration, Problems and a New Policy." Toronto: April 1985.

New York City Department of Transportation. "Permit Process and Requirements." New York: September 1989.

_____. "Capital Asset Inventory and Maintenance Schedules of New York City Streets and Highways." New York: 1990.

_____. "New York City Street Conditions and Information." Presentation to Borough Presidents. New York: 1991.

Ogelsby, Clarkson H., and R. Gary Hicks. Highway Engineering. New York: John Wiley & Sons, 1982.

Organization for Economic Co-operation and Development. "Pavement Management Systems." Road Transport Research. 1987.

O'Rourke, T. D., and Arvind S. Kumbhojkar. "Field Testing of Cast Iron Pipeline Response of Shallow Trench Construction." Geotechnical Engineering Report 84-3. Ithaca, New York: Cornell University, June 1984.

Prager, William., and Philip G. Hodge. Jr. Theory of Perfectly Plastic Solids. New York: Dover Publications, 1968.

Shahin, M. Y., and J. A.. Crovetti. "Effects of Utility Cut Patching on Pavement Performance and Rehabilitation Costs." Prepared for the Annual Meeting of the TRB, Washington, D.C., January, 1986: August 10, 1985.

Sully, J. P., R. G. Campenella, and P. K. Robertson. "Overconsolidation Ratio Of Clays From Penetration Pore Pressure." Journal of Geotechnical Engineering 114 (February, 1988): 209-16.

Terzaghi, Karl, and Ralph B. Peck. Soil Mechanics in Engineering Practice. 2d ed., New York: John Wiley & Sons, 1967.

Terzaghi, Karl. Theoretical Soil Mechanics. New York: John Wiley & Sons, 1943.

Transportation Research Record 1205. Pavement Maintenance. Washington, D.C.: Transportation Research Board. 1988

Yoder, E. J., M. W. Witczak. Principles of Pavement Design. New York: John Wiley & Sons, 1975.

Zaniewski, John P. "Pavement Management Systems Concepts and Applications." Tempe, Arizona: Arizona State University.